



Role of oxygen vacancy in metal oxides for photocatalytic CO₂ reduction

Wenbin Jiang^a, Hongyi Loh^a, Beverly Qian Ling Low^a, Houjuan Zhu^a, Jingxiang Low^c,
Jerry Zhi Xiong Heng^a, Karen Yuanting Tang^a, Zibiao Li^{a,b,*}, Xian Jun Loh^{a,**}, Enyi Ye^{a,b,*},
Yujie Xiong^{c,**}

^a Institute of Materials Research and Engineering, A*STAR (Agency for Science, Technology and Research), 138634, Singapore

^b Institute of Sustainability for Chemicals, Energy and Environment (ISCE2), A*STAR (Agency for Science, Technology and Research), 138634, Singapore

^c School of Chemistry and Materials Science, University of Science and Technology of China, Hefei, Anhui 230026, China

ARTICLE INFO

Keywords:

Oxygen vacancy
Photocatalytic CO₂ reduction
Light absorption
Charge separation
Surface reaction

ABSTRACT

Photocatalytic conversion of greenhouse gas CO₂ into valuable solar fuels represents a promising technology for addressing the global energy crisis and environmental issues simultaneously. In such a technology, the development of efficient photocatalysts is a central task for pushing forward the practical application of photocatalytic CO₂ reduction. Due to their low cost, high redox capability, and environmental friendliness, metal oxide-based photocatalysts have been extensively employed for CO₂ reduction. Moreover, oxygen vacancy engineering in metal oxides has gradually emerged as a versatile approach to enhancing their photocatalytic performance for CO₂ reduction. In this article, the state-of-the-art progress in oxygen vacancy engineering, including its synthesis, characterization, and recent advancement in photocatalytic CO₂ reduction, is reviewed. In particular, the roles of oxygen vacancy in promoting the three basic steps in photocatalytic CO₂ reduction, i.e., light absorption, charge separation, and surface CO₂ conversion, are discussed in detail. The current challenges and future opportunities of engineering oxygen vacancy in metal oxide-based photocatalysts for efficient CO₂ reduction are also addressed. This review aims to inspire more creative works on the rational design of oxygen vacancy that maximizes its function, hence accelerating the discovery of high-performance photocatalysts for CO₂ reduction.

1. Introduction

Since the industrial revolution, the extensive consumption of conventional fossil fuels, including coal, oil, and natural gas, has led to a sharp rise in the concentration of atmospheric carbon dioxide (CO₂) [1–3]. As a major greenhouse gas, CO₂ has brought about a series of environmental issues, including the familiar global warming and glacier melting [4–6]. It is estimated that when the concentration of atmospheric CO₂ exceeds 600 ppm, the sea level will increase by 0.4 m [7], posing a great threat to our ecosystem. To lessen the CO₂-induced global environmental issues, it has reached a consensus that the atmospheric CO₂ concentration should peak (net-zero global CO₂ emissions) by mid-century and decline in the second half of this century [8]. In this context, there is an urgent need to develop advanced CO₂ conversion technologies for a carbon-negative future society [9–14].

Since the pioneering work by Fujishima and Honda on solar-driven water splitting [15], the utilization of inexhaustible solar energy as the

energy input for CO₂ conversion (i.e., photocatalytic CO₂ reduction) has attracted massive interest [16–18]. Through semiconductor-based photocatalytic processes [19,20], CO₂ can be converted into valuable green solar fuels [21,22], including CO, CH₄, CH₃OH, and HCOOH. Therefore, it can be considered a strategy that “kills two birds with one stone”, simultaneously eliminating atmospheric CO₂ and producing sustainable fuels and chemicals. In a typical semiconductor-based photocatalytic CO₂ reduction process, there are three basic steps [23]: i) harvesting of solar energy by the semiconductor photocatalyst to produce photogenerated charge carriers, ii) separation and transfer of the charge carriers, and iii) surface reactions between the charge carriers and substrate molecules (i.e., CO₂ and H₂O). Recently, a series of metal oxide semiconductors (e.g., TiO₂, ZnO, Cu₂O, BiVO₄, SrTiO₃) have been explored as the photocatalyst for CO₂ reduction owing to their low cost, high redox capability, environmental friendliness, and excellent chemical and thermal stability [24,25]. However, the performance of pure metal oxides is still far from satisfactory, mainly due to the limited light

* Corresponding authors at: Institute of Materials Research and Engineering, A*STAR (Agency for Science, Technology and Research), 138634, Singapore

** Corresponding authors.

E-mail addresses: lizb@imre.a-star.edu.sg (Z. Li), lohxj@imre.a-star.edu.sg (X.J. Loh), yeey@imre.a-star.edu.sg (E. Ye), yjxiong@ustc.edu.cn (Y. Xiong).

absorption, severe charge carrier recombination, and sluggish surface CO_2 conversion. To mitigate these challenges, many strategies, including morphology control, defect engineering, doping, and heterojunction construction, have been proposed to achieve efficient photocatalytic CO_2 reduction [26–28]. For instance, photosensitizers have been integrated into metal oxides to extend their light-absorption range, while metal co-catalysts are loaded onto their surface to facilitate charge carrier transfer/separation and surface CO_2 conversion.

Among the various strategies [29–32], oxygen vacancy (OV) engineering has been one of the most extensively studied topics [33–35]. OV, as a typical type of point defect [36–38], inevitably exists in metal oxide-based photocatalysts [39,40], especially when the size of the metal oxide is reduced to the nanoscale [41]. OV can significantly affect the optical and electronic properties of metal oxides [42] and thus their photocatalytic performance [43]. In earlier research, OV in the metal oxide matrix was considered detrimental to the photocatalytic process because it serves as a recombination center for charge carriers [44]. Nevertheless, with the rapid development of controllable synthesis and advanced characterization techniques for OV, it has been gradually recognized that OV can potentially influence all three basic steps of semiconductor-based photocatalytic CO_2 reduction. Furthermore, the in-depth understanding of the role of OV has provided plenty of opportunities for performance optimization by OV engineering. A typical case is the rational design of OV in the bulk and surface of metal oxide photocatalysts to achieve improved light absorption and accelerated charge carrier separation simultaneously.

In this review, we focus on clarifying the roles of OV in metal oxide-based photocatalytic CO_2 reduction and demonstrating methods to make rational use of OV for enhanced photocatalytic performance (Fig. 1). Firstly, we present the fundamental concept of metal oxide-based photocatalytic CO_2 reduction and the functions of OV. Subsequently, we discuss the approaches for controllable synthesis of OV in

metal oxides and the related characterization techniques. Furthermore, we summarize recent progress on OV engineering for enhanced photocatalytic CO_2 reduction, emphasizing the detailed roles of OV in promoting the three basic steps of semiconductor-based photocatalytic CO_2 reduction. Finally, an outlook of existing challenges and future opportunities is presented. As far as we know, this report is the first comprehensive review that clarifies the detailed roles of OV in metal oxide-based photocatalytic CO_2 reduction.

2. Fundamentals

In photocatalytic CO_2 reduction, catalytic activity and target product selectivity are two critical factors for performance evaluation. These two factors are both dependent on the three basic steps of semiconductor-based photocatalytic CO_2 reduction, light absorption, charge separation, and surface CO_2 conversion. In this sense, OV in metal oxides can significantly alter these basic steps, thus possessing immense influences on photocatalytic CO_2 reduction activity and selectivity.

2.1. Metal oxide-based photocatalytic CO_2 reduction

In a typical semiconductor-based photocatalytic CO_2 reduction process (Fig. 2a), the semiconductor photocatalyst is first excited by absorbing an incident photon with energy larger than its bandgap energy [45]. Along with photon absorption, electron hopping occurs from the valence band to the conduction band of the semiconductor, leaving a hole in the valence band. The photogenerated electrons and holes are then separated and transferred from the bulk to surface sites. During this process, most of the electrons and holes are consumed by recombination (step iv in Fig. 2a). Only a fraction of them can reach the catalyst surface sites and finally be consumed by surface reactions with substrate reactants (i.e., CO_2 , protons, and H_2O). H_2O is needed to consume photogenerated holes and provide protons for the continuous conversion of CO_2 . In addition, given that carbon has the highest valence state in CO_2 (+4), it can only accept electrons to be reduced into a variety of solar fuels, including CO (+2), HCOOH (0), CH_3OH (−2), and CH_4 (−4). In principle, the CO_2 reduction products can be controlled thermodynamically by the different redox potentials between CO_2 and the various reduction products (Table 1) [17,24]. However, complications arise when surface reaction kinetics is considered. For example, although the conversion of CO_2 to CH_4 is the most thermodynamically favorable, the dominant product will be CO when the electron supply is insufficient due to reaction kinetic limitations. In addition, if the produced CO can be stabilized on the surface sites of the photocatalyst, it can be further combined with protons provided by H_2O to produce hydrogenated products. It is worth noting that the protons can also directly accept electrons to generate hydrogen atoms, potentially contributing to H_2 evolution. As such, it remains a great challenge to efficiently utilize photogenerated electrons for highly selective CO_2 reduction.

In addition to selectivity, photocatalytic activity for CO_2 reduction should also be considered during photocatalyst design. To achieve efficient CO_2 reduction, the semiconductor photocatalyst should have both high reduction and oxidation capabilities. Specifically, electrons on the conduction band of the semiconductor should have more negative potential than the redox potential between CO_2 and the target reduction product; meanwhile, holes on the valence band should be oxidative enough to oxidize H_2O into O_2 . In this sense, conventional wide-bandgap metal oxides are considered one of the most promising choices because of their suitable energy band positions (Fig. 3) [46]. However, these metal oxide photocatalysts still suffer from poor CO_2 reduction activities due to the following limitations [47]. Firstly, these wide-bandgap metal oxides can only be excited by UV light (< 400 nm), which accounts for less than 5% of the solar spectrum [48]. Secondly, the charge carriers in these metal oxide photocatalysts experience severe recombination after photoexcitation. Lastly, there are limited active sites on the metal oxide surface for the adsorption and activation of CO_2 ,

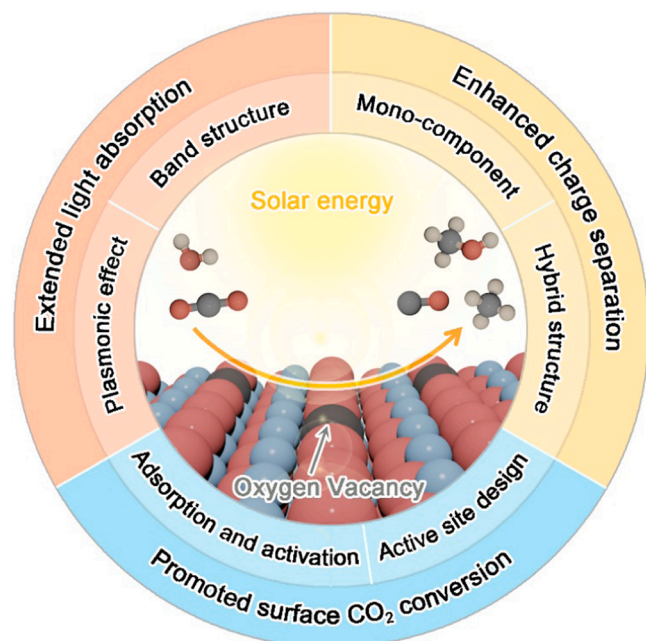


Fig. 1. Schematic illustration of the roles of OV in metal oxide-based photocatalytic CO_2 reduction. OV can extend the light absorption range of metal oxide photocatalysts by tuning their energy band structures (e.g., band positions and defect states) and inducing a plasmonic effect. The OV-induced defect state can trap photogenerated electrons, allowing enhanced charge separation in mono-component metal oxides and metal oxide-based hybrid nanostructures. Moreover, the role of OV in promoting the adsorption and activation of CO_2 provides abundant opportunities for rational active site design, benefiting the development of highly efficient photocatalysts.

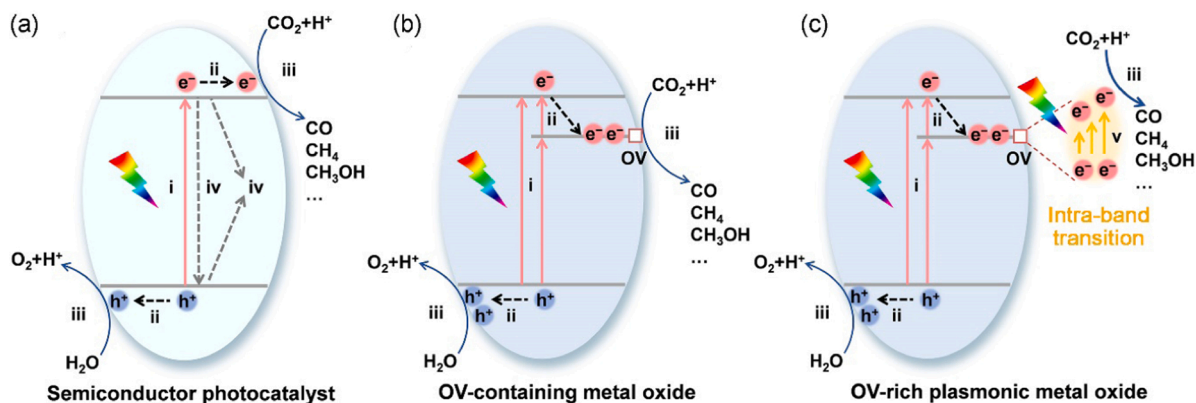


Fig. 2. Schematic illustration for (a) the overall photocatalytic process of CO₂ reduction with H₂O over a semiconductor photocatalyst and (b,c) the influences of OV on the process. The numbers i, ii, and iii represent the three basic steps in photocatalytic CO₂ reduction, i.e., light absorption, charge separation, and surface reaction. Following this, numbers iv and v represent the recombination of photogenerated electrons and holes and the intra-band transition of electrons in the OV-induced defect band, respectively. Step iv can occur either upon the generation of electrons and holes or during their migration from the bulk to surface sites. In addition, it should be predominant even in the presence of OV. However, to simplify the figure and thus facilitate reading, this step is not shown in Fig. 2b and c.

Table 1

Thermodynamic parameters for common CO₂ reduction reactions in photocatalysis.

Entry	Chemical equations	$^2 E_{\text{redox}}$ (V vs. NHE)		$^3 \Delta H^0$ (kJ mol ⁻¹)
		PH = 0	PH = 7	
1	$\text{CO}_2 + \text{e}^- \rightarrow \bullet\text{CO}_2^-$	-1.44	-1.85	/
3	$\text{CO}_2 + 2 \text{H}^+ + 2\text{e}^- \rightarrow \text{CO}_{(\text{g})} + \text{H}_2\text{O}_{(\text{l})}$	-0.11	-0.52	-41.2
2	$\text{CO}_2 + 2 \text{H}^+ + 2\text{e}^- \rightarrow \text{HCOOH}_{(\text{l})}$	-0.20	-0.61	-31.2
4	$\text{CO}_2 + 4 \text{H}^+ + 4\text{e}^- \rightarrow \text{HCHO}_{(\text{g})} + \text{H}_2\text{O}_{(\text{l})}$	0.07	-0.48	-121.0
5	$\text{CO}_2 + 6 \text{H}^+ + 6\text{e}^- \rightarrow \text{CH}_3\text{OH}_{(\text{l})} + \text{H}_2\text{O}_{(\text{l})}$	0.03	-0.38	-131.0
6	$\text{CO}_2 + 8 \text{H}^+ + 8\text{e}^- \rightarrow \text{CH}_4_{(\text{g})} + 2 \text{H}_2\text{O}_{(\text{l})}$	0.17	-0.24	-253.0
7	$2\text{CO}_2 + 8 \text{H}^+ + 8\text{e}^- \rightarrow \text{CH}_3\text{COOH}_{(\text{l})} + 2 \text{H}_2\text{O}_{(\text{l})}$	0.11	-0.30	122.1
8	$2\text{CO}_2 + 12 \text{H}^+ + 12\text{e}^- \rightarrow \text{C}_2\text{H}_5\text{OH}_{(\text{l})} + 3 \text{H}_2\text{O}_{(\text{l})}$	0.09	-0.32	216.1
9	$2\text{CO}_2 + 12 \text{H}^+ + 12\text{e}^- \rightarrow \text{C}_2\text{H}_4_{(\text{g})} + 4 \text{H}_2\text{O}_{(\text{l})}$	0.08	-0.33	127.8
10	$2\text{CO}_2 + 14 \text{H}^+ + 14\text{e}^- \rightarrow \text{C}_2\text{H}_6_{(\text{g})} + 4 \text{H}_2\text{O}_{(\text{l})}$	0.14	-0.27	264.3
11	$2 \text{H}^+ + 2\text{e}^- \rightarrow \text{H}_{2(\text{g})}$	0	-0.41	0
12	$\text{H}_2\text{O}_{(\text{l})} + 2 \text{h}^+ \rightarrow \bullet\text{OH}_{(\text{aq})} + 2 \text{H}^+$	2.73	2.32	71.0
13	$2 \text{H}_2\text{O}_{(\text{l})} + 4 \text{h}^+ \rightarrow \text{O}_{2(\text{g})} + 4 \text{H}^+$	1.23	0.82	572.0

¹ g: gas, l: liquid.

² E_{redox} : redox potential

³ ΔH^0 : reaction enthalpy.

resulting in sluggish CO₂ reduction kinetics.

2.2. OV in metal oxide photocatalysts

Fortunately, the introduction of OV into the metal oxide matrix has largely alleviated these limitations [41,43,49]. In metal oxides, OV assumes a local cave structure where an oxygen atom is removed from the oxide matrix [50]. The removal of the oxygen atom leaves two electrons at the vacancy site, and thus, the whole metal oxide system maintains a charge-neutral state ($\text{O}^{2-} \rightarrow \text{O}_{\text{atom}} + \text{OV} + 2 \text{e}^-$). The electrons accumulated at the OV sites can be transferred to adjacent metal atoms, forming positively charged OV sites and reduced metal centers. Bao and co-workers [51] studied the influence of hydrogen treatment on the evolution of OV and Ti³⁺ sites in the TiO₂ matrix. It was found that Ti³⁺ only appeared after the treatment temperature exceeded 450 °C, while OV already formed at a lower temperature. This result corroborated that the electrons in the OV were transferred out to form Ti³⁺ when sufficient energy was supplied by the hydrogen at higher temperatures. Additionally, positively charged OV sites are formed concomitant with the electron transfer and Ti³⁺ formation. The OV in a charge state of neutral, +1, or +2, can be respectively denoted as V_O^\times , $\text{V}_\text{O}^\bullet$, $\text{V}_\text{O}^{\bullet\bullet}$ according to the Kröger-Vink notation [50].

As an intrinsic point defect [42,52], OV commonly exists in metal oxides and can significantly alter their optical and electronic properties [53–57]. Moreover, considering that OV can be introduced in situ by light irradiation [58–60], it is expected to have a non-negligible influence on the photocatalytic process over metal oxide-based

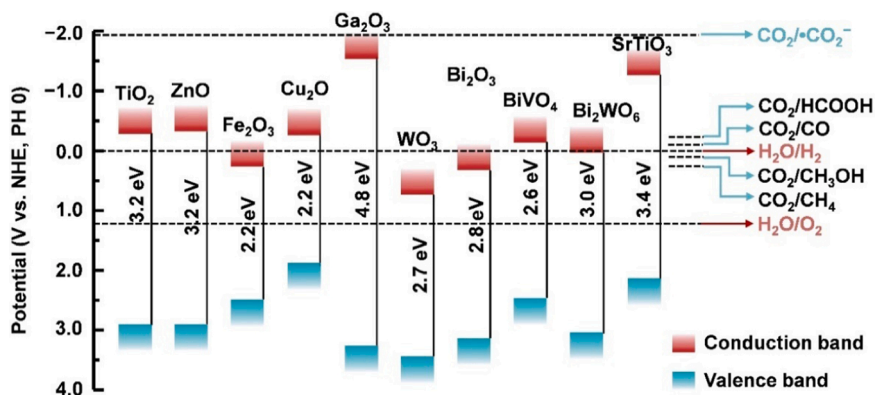


Fig. 3. Schematic illustration for energy band structures of common metal oxides. While some metal oxides (e.g., WO₃) do not have suitable conduction band positions to drive CO₂ reduction, they can form heterojunctions with other semiconductor materials and contribute to photocatalytic CO₂ conversion.

photocatalysts [37,61]. OV as an electron donor can induce a defect state (an inter-band state between conduction and valence bands) in semiconductor photocatalysts (Fig. 2b). Yim et al. used electron bombardment to vary the density of bridging OV in rutile $\text{TiO}_2(110)$ with in situ monitoring of the bandgap state (i.e., defect state) using ultraviolet photoemission spectroscopy [62]. It was revealed that the intensity of the photoemission peak was directly proportional to the OV density, confirming the dominant contribution of OV to the defect state. The OV-induced defect state allows metal oxide to be excited by absorbing photons with energy lower than its bandgap. In addition, Zhang et al. studied the influence of OV on energy band positions of metal oxide photocatalysts using OV-rich WO_3 as an example [63]. Theoretical calculations confirmed that the valence and conduction bands of WO_3 are mainly contributed by O 2p and W 5d orbitals, respectively. Accordingly, the electron transfer from OV to surrounding oxygen atoms through the coordination-unsaturated metal atoms will elevate the potential of the O 2p orbital. In other words, the OV-rich sample possesses a higher valence band maximum and thus narrower bandgap, resulting in promoted light absorption.

More interestingly, a unique electron excitation (i.e., light absorption) process has also been observed for some heavily OV-doped metal oxides (e.g., WO_3 , MoO_3 , and Bi_2O_3) [64–66]. In these metal oxides, the large number of electrons brought about by the heavily OV doping can absorb the incident light and experience intra-band transition in the OV-induced defect band (with a continuum of states available for ensemble electron excitation) (Fig. 2c) [67], analogous to the localized surface plasmon resonance (LSPR) excitation of free electrons in metal nanostructures (e.g., Au, Ag, and Cu) [68–70]. A key characteristic of LSPR excitation is that the optical extinction cross-section of the material will reach a maximum at certain frequencies owing to a collective excitation of electrons [68]. In other words, absorption peaks can be observed in the absorption spectra of the material, which can be monitored by UV–visible–near infrared (UV–vis–NIR) spectroscopy. Specifically, noble metal nanostructures with a high electron concentration (10^{22} – 10^{23} cm^{-3}) exhibit strong LSPR peaks in the visible light region. In contrast, heavily OV-doped metal oxides typically display LSPR peaks at 700–1250 nm due to the relatively low electron concentration (10^{21} – 10^{22} cm^{-3}) [71]. Nonetheless, rational regulation of electron concentration in these OV-containing plasmonic metal oxides presents a promising strategy for tuning their LSPR characteristics (e.g., intensity and peak position).

In short, OV can significantly extend the light absorption range of metal oxide photocatalysts by tuning their band structures (i.e., defect state and band positions) and inducing a plasmonic effect [72]. It is worth mentioning that the OV-induced defect state can further enhance the separation of photogenerated electrons and holes by serving as an electron-trapping state [73]. Therefore, more electrons and holes can be transferred to the surface sites of the photocatalyst, contributing to CO_2 reduction and H_2O oxidation, respectively [61]. Moreover, OV can also regulate the adsorption and activation behaviors of CO_2 on the surface of metal oxide photocatalysts. Rational active site design based on OV thus enables a delicate control of CO_2 reduction activity and target product selectivity. Therefore, the current studies on OV can be roughly divided into two parts: i) understanding the basics of OV including its preparation, structures and properties, and ii) rationally engineering OV for enhanced photocatalytic CO_2 reduction performance. The current progress of OV engineering in photocatalytic CO_2 reduction will be discussed in detail in Section 4, after a brief introduction of the synthesis and characterization techniques of OV in metal oxides.

3. Controllable synthesis and characterization of OV in metal oxides

3.1. Controllable synthesis of OV-containing metal oxides

The controllable synthesis of OV-containing metal oxides is the

prerequisite for their practical application. OV is introduced by removing an oxygen atom from the metal oxide, which can be regarded as a reduction process. Therefore, the formation of OV is determined by both the reductive environment conditions and the intrinsic reducibility of the metal oxide (i.e., OV formation energy). By extension, OV engineering in metal oxides can be approached from two aspects, the application of reductive synthesis/treatment environments and the regulation of the intrinsic OV formation energy.

3.1.1. Application of reductive environment

OV can be introduced into the metal oxide matrix during material synthesis [74]. In this case, reducing agents, such as glucose, alcohol, oxalic acid, ascorbic acid, and metallic metals, are commonly employed to provide a reductive synthesis environment for OV formation. For example, Kong et al. prepared OV-rich Bi_2WO_6 using a simple one-step ethylene glycol-assisted solvothermal method [75]. The redox reaction between ethylene glycol and Bi_2WO_6 resulted in the selective removal of oxygen atoms from the Bi_2WO_6 surface. In addition, the generated OVs can be refilled with oxygen atoms after calcinating the obtained sample in an air atmosphere at 400 °C for 4 h, as evidenced by the change in absorption in the visible light range (Fig. 4a). After material synthesis, OV can also be introduced by reduction treatment. Such OV is generally located on the surface of the material and can be accompanied by the appearance of surface disorder (amorphous layer) [76]. Huang and co-workers developed a disorder-engineered blue TiO_2 sample using lithium-containing ethylenediamine (Li-EDA) as a reducing agent [77]. The obtained sample featured a unique surface disorder layer that contains numerous OVs and doped hydrogen atoms. Moreover, the thickness of the disordered layer can be controlled by simply tuning the Li dosage.

High-temperature treatment is also an effective method to create OV in metal oxides. In a high-temperature environment, the oxygen atom removal efficiency from metal oxide depends on the oxygen partial pressure. In this regard, reducing agents, such as H_2 , NH_3 , NaBH_4 , Mg, and Al, are commonly employed to consume oxygen and thus assist the oxygen atom removal from the metal oxide matrix. Liu et al. recently reported the synthesis of OV-rich MoO_{2-x} nanobelts by thermal treatment of MoO_3 nanobelts at 550 °C under a 10% H_2/Ar mixture [78]. The OV-poor MnO_2 sample can be obtained by treating the OV-rich MoO_{2-x} at 200 °C in air. Similarly, Zhang and co-workers developed a universal NH_3 -assisted reduction strategy to introduce OV into transition metal oxides (WO_3 , MnO_2 , Nb_2O_5 , and MoO_3) [79]. Mechanism studies suggested that H and N atoms from NH_3 were able to extract oxygen atoms in transition metal oxides to form H_2O , N_2 , N_2O , and NO (Fig. 4b). In addition, Gao et al. reported the synthesis of black TiO_2 arrays using Al as the reductant [80]. Al can assist in capturing the oxygen released by metal oxides during high-temperature treatment, thus facilitating the lowering of oxygen partial pressure and formation of Ti^{3+} ions and OVs on the sample surface (Fig. 4c). The combination of solid (e.g., Mg) and gaseous (e.g., H_2) reductants can be an even more powerful technique for lowering oxygen partial pressure and introducing OV into metal oxides [81]. However, excessive OVs in the catalyst may not be beneficial for its application in photocatalytic CO_2 reduction.

Despite the strong reducing capability, these externally added agents may also introduce impurities such as interstitial H and N dopants into the metal oxide matrix [82–84]. To overcome this, inert conditions (e.g., Ar and vacuum) can be used to control the oxygen partial pressure in the environment and thus effectively create OV without impurity introduction. It is worth noting that this type of treatment is generally applied to metal oxides with relatively soft metal–oxygen bonds, such as BiVO_4 , WO_3 , ZnO , SnO_2 , ZnO , and CuO . High temperatures are still needed due to the weak reduction capability of the inert gases. However, too high annealing temperatures will potentially affect the morphology and phase of some metal oxides (e.g., CuO and Fe_2O_3). On this note, Zhang and co-workers recently proposed a vacuum-assisted self-photoetching approach to synthesize OV-rich orthorhombic cobalt carbonate

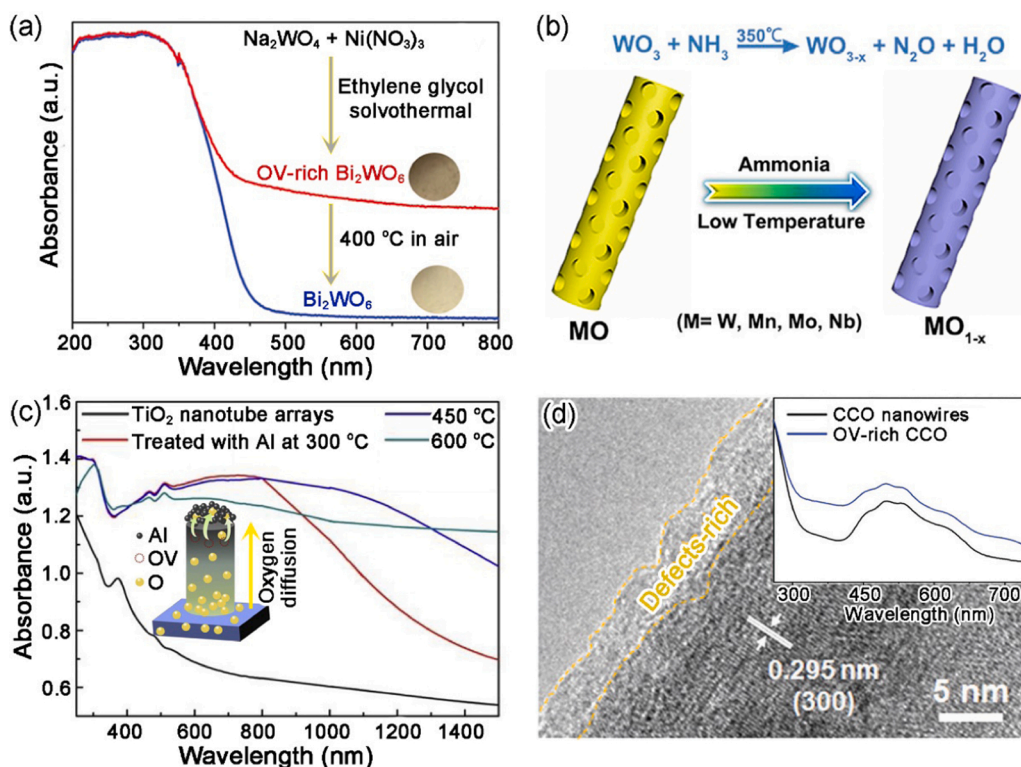


Fig. 4. (a) UV-vis diffuse reflectance spectroscopy (DRS) spectra of OV-rich Bi_2WO_6 obtained from one-step ethylene glycol-assisted solvothermal process. The inset shows the color of the samples. Reproduced with permission from Ref. [75]. Copyright 2016, The Royal Society of Chemistry. (b) Schematic illustration for the low-temperature ammonia-assisted synthetic process of OV-enriched transition metal oxides. Reproduced with permission from Ref. [79]. Copyright 2018, Elsevier B.V. (c) UV-vis DRS spectra of pristine TiO_2 nanotube arrays and the TiO_2 nanotube arrays treated with Al at 300, 450, and 600 °C. The inset shows the Al-assisted oxygen atom removal process in TiO_2 . Reproduced with permission from Ref. [80]. Copyright 2019, Elsevier B.V. (d) High-resolution TEM image of OV-rich cobalt carbonate hydroxide nanowires (CCO, $\text{Co}(\text{CO}_3)_{0.5-0.11} \text{H}_2\text{O}$) obtained from a vacuum-assisted self-photoetching approach. The inset shows UV-vis DRS spectra of pristine CCO nanowires and the OV-rich CCO nanowires. Reproduced with permission from Ref. [59]. Copyright 2021, Elsevier B.V.

hydroxide nanowires ($\text{Co}(\text{CO}_3)_{0.5-0.11} \text{H}_2\text{O}$) at ambient temperature [59]. The authors demonstrated that the crack of carbonate species on the nanowire surface under light irradiation resulted in the formation of an OV-rich surface layer (i.e., coordination-unsaturated Co sites) (Fig. 4d).

In principle, many other methods that can provide sufficient energy and a reductive environment have the potential to create OV in metal oxides. For instance, plasma treatment has recently attracted exceptional attention due to its ability to create OV under mild conditions [85]. The plasma-assisted OV creation can be controlled by plasma compositions (e.g., H_2 , Ar, and air), power, and treatment duration. Moreover, this plasma treatment can be carried out in a fast and highly efficient way without compromising its bulk morphology. Despite its potential, the application of this technique in photocatalytic CO_2 reduction is still scarce due to the low stability of the introduced OV sites. Zhu et al. reported that a hole scavenger (triethanolamine, TEOA) was needed for CO_2 reduction over an OV-rich In_2O_3 photocatalyst synthesized by NH_3 plasma [86]. In another work, Chen et al. reported that continuous Ar plasma treatment is needed to maintain the OV on the NiO/TiO_2 catalyst surface in order to achieve stable CO_2 reduction [87]. Therefore, the development of novel strategies to extend the application of this time- and energy-saving technique in photocatalytic CO_2 reduction is highly desired.

3.1.2. Regulation of OV formation energy

The ease of introducing OV in a material can be described by the OV formation energy, where a lower OV formation energy means easier OV introduction and vice versa. Therefore, the regulation of OV formation energy is another effective strategy for controllable OV introduction. Shi and co-workers developed a facile Ti-OH bond-breaking approach to create OV in titania. Compared to Ti-O bonds, the energy required for the dissociation of Ti-OH bonds is much lower. Therefore, OV was efficiently introduced into titania by simply calcining $\text{TiO}_x(\text{OH})_y$ precursor in N_2 [88]. A similar method was adopted to synthesize OV-containing NiO from $\beta\text{-Ni}(\text{OH})_2$ precursor [89]. In addition, Di et al. reported a strain-assisted synthesis of OV in $\text{Bi}_{12}\text{O}_{17}\text{Br}_2$ nanotubes [90].

The stretched local structure on the curved nanotube surface weakens the Bi-O bonding, and as a result, possesses a lower OV formation energy and higher OV concentration, compared to the nanoplate structure (Fig. 5a). Following this line of thought, a high-pressure torsion process is commonly applied to simultaneously introduce lattice strain and OVs in metal oxide materials [91,92]. Moreover, Huang and co-workers reported the OV formation in WO_3 film that was assisted by lattice strain arising from the thermal expansion during the photothermal reaction. The lattice strain and OV formation can collectively affect the electronic structure of the photocatalyst, resulting in enhanced performance toward photocatalytic CO_2 reduction [93].

In addition, size control of metal oxides provides the opportunity for OV engineering because OV formation is easier on the surface compared to bulk [94]. Theoretical calculations on MgO and CeO_2 suggest that surface oxides possess lower OV formation energy [95,96]. A smaller size means a higher surface area and thus a higher possibility for OV formation. Based on this, Guo et al. synthesized ultra-small $\text{Bi}_2\text{Sn}_2\text{O}_7$ nanoparticles (~4 nm) with high surface area [97]. Resultingly, a large number of OVs was created in the ultra-small $\text{Bi}_2\text{Sn}_2\text{O}_7$, allowing the sample to exhibit increased light absorption in the visible light range compared to bulk $\text{Bi}_2\text{Sn}_2\text{O}_7$ (Fig. 5b). In addition, the same research group reported the synthesis of Bi_2MoO_6 ultrathin nanosheets (with a thickness of 1–2 nm) using layered BiOBr nanosheets as the template [98]. The results suggested the existence of abundant OVs on the material surface in the form of Bi-O vacancy pairs. Moreover, the OV confined in the ultrathin nanosheets led to a new donor level near the conduction band minimum and a higher DOS at the valence band maximum, which extended the light absorption and accelerated the charge carrier separation [99].

Recently, engineering the local structure of OV has been gradually recognized as an effective pathway for promoting OV formation. The concept of “asymmetric oxygen vacancy site” is introduced to describe an OV site with asymmetric coordination of cations ($\text{M}_1\text{-OV-M}_2$). Under such a condition, OV sites are more easily refilled and regenerated (i.e., lower OV formation energy of the metal oxide matrix) [100]. In this regard, doping is commonly used to introduce asymmetry and thus

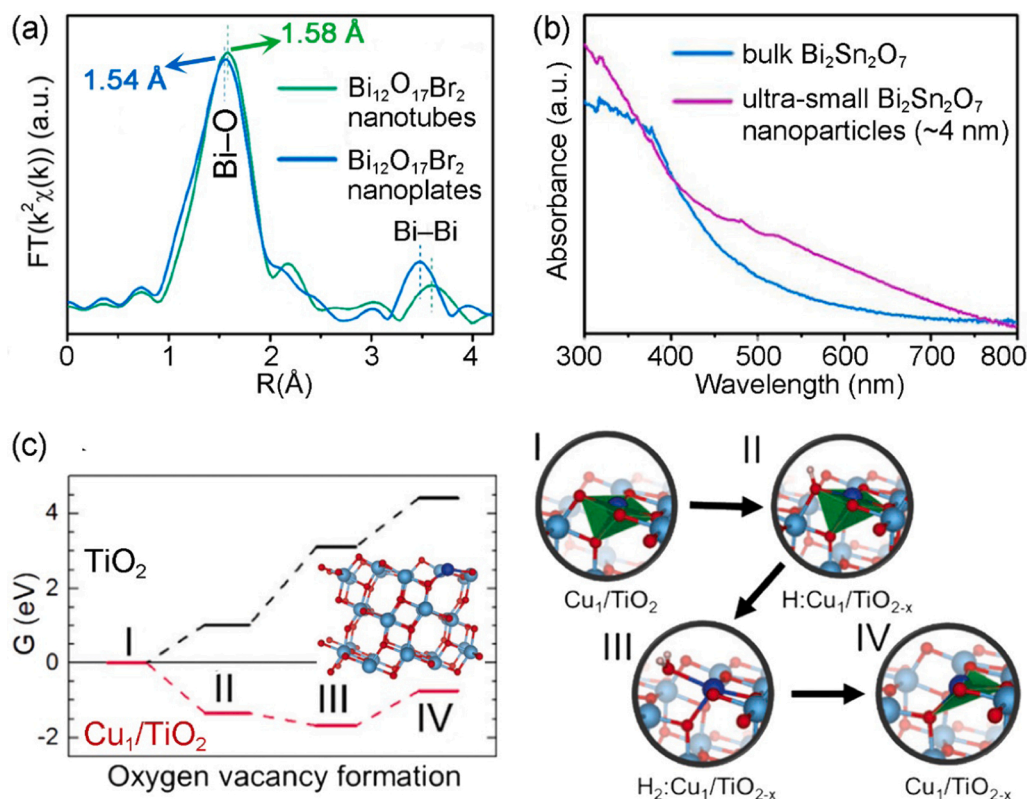


Fig. 5. (a) Fourier-transform Bi L₁-edge EXAFS spectra of $\text{Bi}_{12}\text{O}_{17}\text{Br}_2$ nanotubes and nanoplates, highlighting the elongated Bi–O bonds on a curved surface (i.e., with lattice strain). Reproduced with permission from Ref. [90]. Copyright 2020, American Chemical Society. (b) UV–vis DRS spectra of ultra-small $\text{Bi}_2\text{Sn}_2\text{O}_7$ nanoparticles, in comparison to bulk $\text{Bi}_2\text{Sn}_2\text{O}_7$. Reproduced with permission from Ref. [97]. Copyright 2021, Elsevier B.V. (c) Simulated energy changes of OV formation on TiO_2 and Cu-doped TiO_2 (Cu_1/TiO_2). In the Cu–O₄ structure model (green), Cu, O, and Ti atoms are in blue, red, and cyan colors, respectively. Reproduced with permission from Ref. [104]. Copyright 2022, Elsevier B.V.

promote OV formation [101]. For instance, Brant et al. observed a neutral Cu^{2+} –OV complex in Cu-doped rutile TiO_2 crystalline. Experimental evidence shows that the substitution of Ti^{4+} by Cu^{2+} led to the formation of OV adjacent to the Cu^{2+} site due to charge compensation [102]. First-principle results also confirmed the formation of charge-compensating OVs at sites adjacent to the metal dopant [103]. With this in mind, Lee et al. successfully prepared an OV-rich TiO_2 photocatalyst for efficient CO_2 reduction through a facile Cu-doping strategy [104]. Theoretical calculations confirmed that the electronic interaction between Cu and TiO_2 could lower the energy for OV formation in TiO_2 (Fig. 5c), leading to spontaneous OV formation near the Cu dopant. Moreover, the Cu dopant and the introduced OV sites can jointly stabilize CO_2 reduction intermediates on the TiO_2 surface, resulting in substantially enhanced performance compared to pristine TiO_2 .

Due to the charge-compensating characteristic, doping-induced OVs typically possess much higher stability than those on pristine metal oxides. Bo et al. reported that the OV in Fe-doped TiO_2 was maintained after calcination at 800 °C in air, which can hardly be expected for undoped TiO_2 [105]. Similarly, Wang and co-workers also observed metal doping-facilitated OV formation in atomic Ni-loaded TiO_2 catalysts during an oxidative molten salt treatment process [106]. The high stability of OV makes these metal oxides potential photocatalysts for highly efficiently photocatalytic CO_2 reduction. It is also worth mentioning that non-metal doping (e.g., C and N) can likewise induce the charge-compensating effect and thus the formation and stabilization of OV on the metal oxide surface [107–109]. In addition to doping, the formation of a metal/oxide interface is another effective pathway to regulate the reducibility of metal oxides [110]. The metal/oxide interface can be formed either by loading small metal nanoparticles onto the surface of metal oxide substrates [111–113] or by coating metal oxide nanoparticles/films onto metal substrates [114]. However, this method is currently mainly used to obtain metal oxide photocatalysts for CO_2 reduction with H_2 [115,116]. The use of H_2O as the reactant may not be able to regenerate OV at the metal/oxide interface during CO_2

conversion. Nonetheless, the integration of metal/oxide interfaces with other modification methods (e.g., doping) may serve as a promising pathway for efficient OV formation and CO_2 reduction.

3.2. Characterization of OV in metal oxides

3.2.1. Electron paramagnetic resonance and X-ray absorption spectroscopy

Identifying the state of OV in metal oxides is essential for its controllable synthesis and subsequent application [117–119]. In addition to the optical characterization method (i.e., UV–vis DRS), many methods have been proposed for OV characterization (Fig. 6) [120]. Among these methods, transmission electron microscope (TEM),

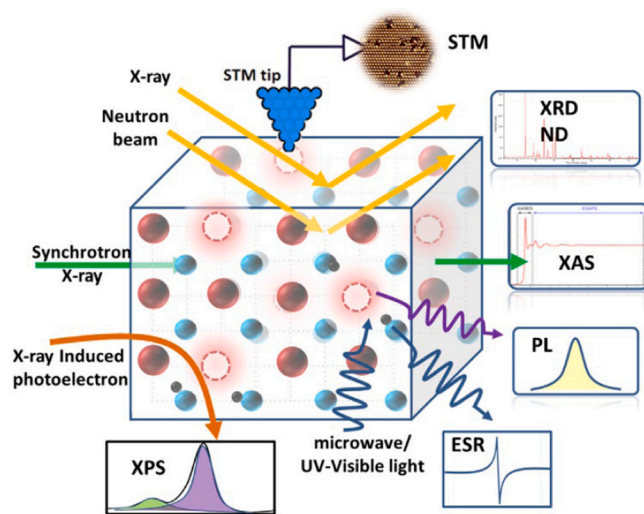


Fig. 6. Schematic illustration for the methods used to characterize OV (dashed circles) in metal oxides. Reproduced with permission from Ref. [120]. Copyright 2021, John Wiley & Sons, Inc.

electron paramagnetic resonance (EPR), X-ray absorption spectroscopy (XAS), X-ray photoemission spectroscopy (XPS), photoluminescence (PL), and positron annihilation spectrometry (PAS) are most often used. With the assistance of these characterization tools, Zhang et al. systematically investigated the OV characteristics within WO_3 nanoplates [63]. In the atomic resolution high-angle annual dark-field scanning transmission electron microscopy (HAADF-STEM) image, lattice disorder and dislocation were observed in the defect-rich WO_3 nanosheets (R-WO_3), indicating the formation of a defective surface (Fig. 7a). The defect types were further confirmed by EPR and W L_3 -edge extended X-ray absorption fine structure (EXAFS) spectra. The symmetrical EPR signal at $g = 2.002$ was assigned to single electron-trapped OVs on R-WO_3 (Fig. 7b). Furthermore, based on the fitting results of the W L_3 -edge EXAFS spectra, the R-WO_3 displayed reduced total W–O coordination numbers compared to commercial WO_3 and defect-free WO_3 (D-WO_3) (Fig. 7c).

Moreover, the development of advanced in situ characterization techniques (e.g., EPR and in situ XAS) to monitor the dynamic changes of OV under light irradiation and/or during interactions with adsorbed molecules is highly desirable for understanding the role of OV [121]. For example, Xiong and co-workers employed in situ EPR to investigate the

changes of OV under light irradiation and in different atmospheres (i.e., He and N_2) [105]. The reduced EPR signal intensity suggested a decrease in the amount of single-electron trapped OV site under light irradiation in N_2 (Fig. 7d). Similarly, Tang and co-workers successfully used in situ EPR to identify the role of OV as the trapping site for photogenerated electrons over Pd atoms-doped defective In_2O_3 [122]. In situ XAS is also a useful tool to trace the structure evolution of metal oxides during the catalytic reaction [123,124]. Paulus and co-workers studied the electrochemical oxidation behaviors of $\text{SrCoO}_{2.5}$ with in situ Co K-edge XAFS spectroscopy [125]. Surprisingly, an intermediate phase ($\text{SrCoO}_{2.82} \pm 0.07$) with oxygen ordering appeared at room temperature during the oxidation process of $\text{SrCoO}_{2.5}$ to SrCoO_3 . In another report, Park et al. [126] utilized Ce L_3 -edge EXAFS spectra to unravel the photo-induced reduction of Ce^{4+} to Ce^{3+} on the CeO_2 surface (Fig. 7e). The Fourier-transformed EXAFS spectra demonstrated that the CeO_2 reduction is accompanied by an elongation of the Ce–O bond from 2.36 to 2.42 Å due to larger ionic radius of Ce^{3+} (1.14 Å) than Ce^{4+} (1.00 Å).

3.2.2. Positron annihilation spectroscopy

To reliably interpret the characteristics of OV in metal oxides, the quantitative study of OV (e.g., content, types, sizes, and configuration) is

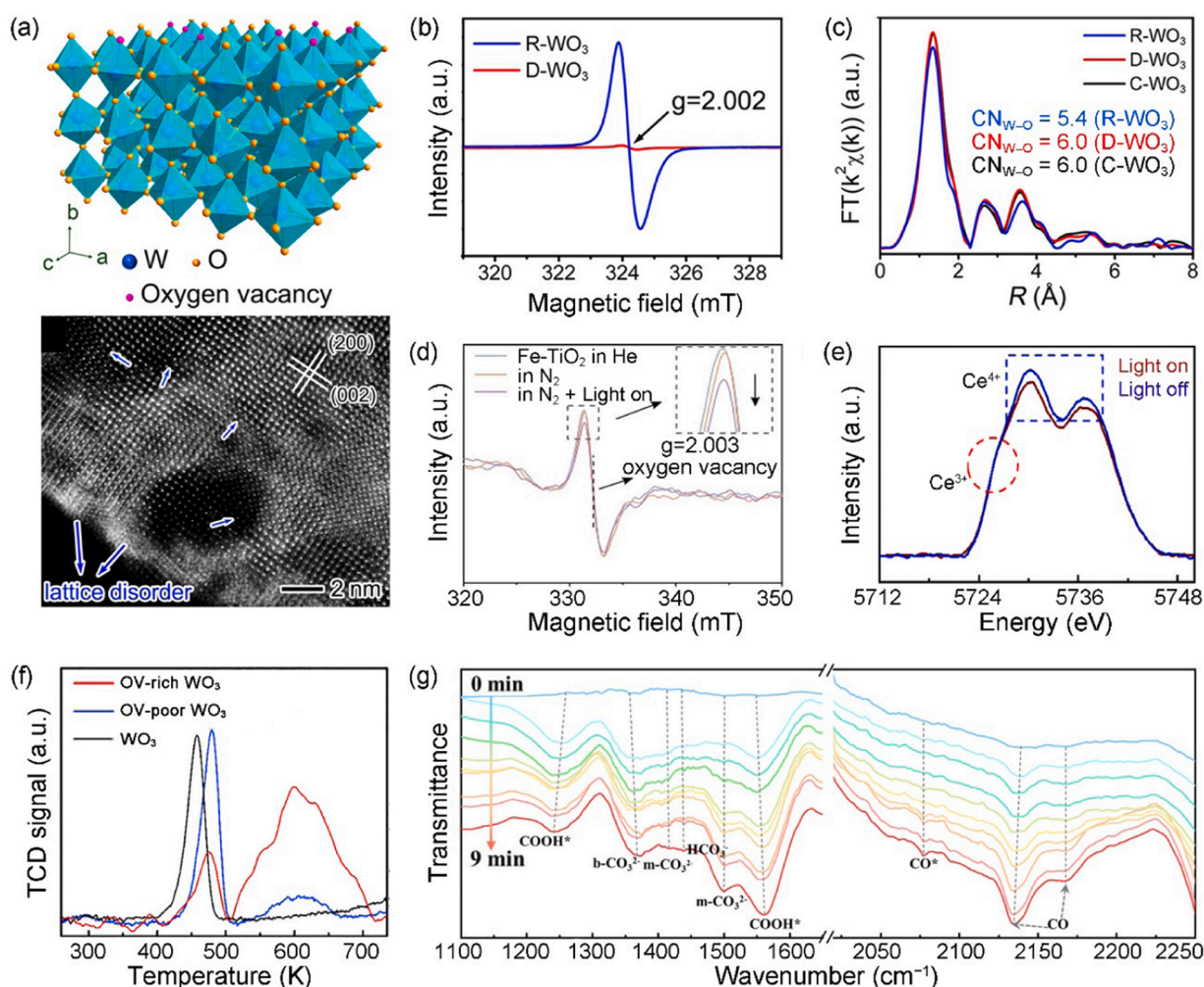


Fig. 7. (a) Schematic illustration of the location of OV in the WO_3 lattice and the corresponding aberration-corrected HAADF-STEM image of defect-rich WO_3 (R-WO_3). (b) Room temperature EPR spectra of R-WO_3 and defect-deficient WO_3 (D-WO_3). (c) Fourier-transform W L_3 -edge EXAFS spectra of R-WO_3 , D-WO_3 , and commercial WO_3 (C-WO_3). Reproduced with permission from Ref. [63]. Copyright 2016, American Chemical Society. (d) In situ EPR spectra of Fe-doped TiO_2 (Fe-TiO_2) before and after light irradiation in the N_2 atmosphere. Reproduced with permission from Ref. [105]. Copyright 2021, John Wiley & Sons, Inc. (e) In situ Ce L_3 -edge EXAFS spectra of $\text{NiO/CeO}_2/\text{rGO}$ before and after light irradiation. Reproduced with permission from Ref. [126]. Copyright 2020, Elsevier B.V. (f) CO_2 TPD spectra of WO_3 , OV-poor WO_3 , and OV-rich WO_3 . Reproduced with permission from Ref. [137]. Copyright 2018, Elsevier B.V. (g) In situ FTIR spectra of photo-catalytic CO_2 conversion over oxygen-defective $\text{Bi}_2\text{O}_2\text{CO}_3$ nanosheets. Reproduced with permission from Ref. [138]. Copyright 2020, John Wiley & Sons, Inc.

essential [127]. PAS is a highly sensitive technique to quantitatively characterize OV-related defects in metal oxides [128]. The lifetime of positrons can shed light on the size, type, and relative concentration of various defects at even the ppm level. Li and co-workers successfully identified two types of OVs in nanosized ceria [129], small neutral Ce^{3+} -OV complex and large-size clusters of vacancy defects. Based on this insight, the authors were able to establish the relationship between the concentration of defect clusters and the reducibility and reactivity of the nanosized ceria. Furthermore, similar defect types (i.e., small neutral Ti^{3+} -OV associates, large-size vacancy clusters, and a few voids of vacancy associates) were also observed in hydrogenation-modified TiO_2 using PAS [130]. In addition to the defect types and sizes, Zhang et al. [131] recently developed time-resolved optical spectroscopy to “visualize” OV configuration in metal oxides (e.g., WO_3 , $\text{WO}_{2.9}$, and $\text{WO}_{2.72}$). Due to the ultrafast characteristic (femtosecond scale) of this technique, it can accurately reflect the information of the excited states, energy bands, and electron transition routes, thus enabling the fingerprint identification of specific OV configurations in metal oxides.

3.2.3. Atomic-scale electron microscopy and scanning tunneling microscopy

In addition to adopting spectroscopic techniques, OV on some model metal oxides (atomic level flatness and clean surface) can be directly imaged by electron microscopy. Through direct atomic-scale TEM observations and density functional theory calculations, Wang and co-workers demonstrated the proton-dissolution-promoted formation, migration, and clustering of cation and anion vacancies during a water-vapor-enhanced NiCr alloy oxidation process [132]. Scanning tunneling microscopy (STM) is also commonly used to study OV and its interaction with adsorbed molecules (e.g., H_2O , O_2 , and CO_2) [133,134]. It has been successfully employed to image the OV on single crystalline TiO_2 under ultra-high vacuum conditions. Schaub et al. observed the oxygen-mediated OV diffusion on the $\text{TiO}_2(110)$ surface using STM [135]. It was reported that the adsorbed O_2 molecules could donate an oxygen atom to OV and then capture an oxygen atom from a neighboring bridging oxygen row, resulting in the observed OV diffusion. The adsorption process of O_2 was further studied by a subsequent work using anatase $\text{TiO}_2(101)$ as a model surface [136]. It was revealed that the O_2 adsorbed initially on the fivefold-coordinated Ti sites could react with OV to form an $(\text{O}_2)_\text{O}$ interstitial at the OV site.

3.2.4. CO_2 temperature-programmed desorption and infrared spectroscopy

The highly reactive characteristic of OV makes it an excellent active site to interact with CO_2 (i.e., CO_2 adsorption and activation). The adsorption of CO_2 can be quantitatively studied by CO_2 adsorption isotherms and temperature-programmed desorption (TPD). Notably, CO_2 TPD can shed light on the adsorption strength of CO_2 (i.e., physical adsorption, weak chemical adsorption, and strong chemical adsorption). Liang et al. recently employed CO_2 TPD to study the adsorption behaviors of CO_2 on WO_3 , OV-poor WO_3 , and OV-rich WO_3 [137]. Two peaks at around 460 K and 600 K were observed in TPD spectra and the peak intensity at 600 K was remarkably enhanced with the introduction of OV, confirming the OV-enabled stronger CO_2 adsorption (Fig. 7f). After adsorption, the subsequent activation and conversion of CO_2 can produce abundant surface carbon-containing intermediates (e.g., carboxyl group, carbonate, bicarbonate, and CO), which can be monitored by Fourier-transform infrared (FTIR) spectroscopy. For instance, Zu et al. recently applied in situ FTIR to gain insight into the photocatalytic CO_2 reduction process over oxygen-defective $\text{Bi}_2\text{O}_2\text{CO}_3$ nanosheets [138]. Upon light irradiation, two new peaks at 1565 and 1230 cm^{-1} , which can be ascribed to the vibrations of $^*\text{COOH}$ groups, appeared in the FTIR spectra (Fig. 7g). Moreover, the signal attributed to adsorbed CO gradually intensified with prolonged irradiation time. These results collectively suggest a $^*\text{COOH}$ -mediated CO_2 -to-CO conversion pathway on the OV-containing catalyst surface.

Despite the excellent methods described above, there are still some discrepancies to be noted in OV characterization. For example, in the

EPR spectra, the signal at $g = 2.002$ is ascribed to single electron-trapped OV sites. Resultingly, the intensity of this signal would be determined by both the concentration and electronic structure of OV. As such, more attention should be taken when analyzing the changes in the signal intensity under light irradiation or during in situ reactions. In the case of XPS, the peak at $\sim 531.0\text{ eV}$ in the O 1s XPS spectra is often ascribed to OV. However, this peak can also be ascribed to surface-adsorbed oxygen species (e.g., O_2^- and hydroxyl groups). To address this, PL may be an ideal alternative to O 1s XPS for distinguishing and quantifying the OV-induced defect state in some cases (e.g., ZnO-based materials) [139–141]. Despite these shortcomings, it has been well recognized that the EPR and XPS are highly sensitive to the metal valence states, which can indirectly shed some light on the state of OV in metal oxides. Finally, it is highly recommended to combine multiple characterization tools to gain a comprehensive insight into the structure and role of OV.

4. Recent progress of OV engineering in metal oxides for photocatalytic CO_2 reduction

The rapid development of controlled synthesis and advanced characterization techniques for OV-containing metal oxides has laid a foundation for their application in photocatalytic CO_2 reduction. The introduction of OV in metal oxide-based photocatalysts can potentially influence all three basic steps of photocatalytic CO_2 reduction: light absorption, charge separation, and surface CO_2 conversion reaction [142]. The role of OV can differ according to its specific state (e.g., concentration, location, and metal oxide components). For example, a high OV concentration mainly contributes to enhanced light absorption, while a moderate amount of OV on the photocatalyst surface can facilitate charge carrier separation and surface CO_2 conversion. A comprehensive understanding of the role of OV in photocatalytic CO_2 reduction is thus the premise for the rational design of high-performance metal oxide-based photocatalysts.

4.1. Oxygen vacancy-extended light absorption

To meet the thermodynamic requirements for photocatalytic CO_2 reduction with H_2O , the commonly used metal oxide photocatalysts typically have a wide bandgap ($> 3.0\text{ eV}$). As a result, these metal oxides can only be excited by UV light, significantly limiting their photocatalytic activity toward CO_2 reduction. With the introduction of OV, this limitation can be largely alleviated by extending the light response of metal oxide to the visible light range.

4.1.1. OV-modified band structure

OV can extend the light-absorption range of metal oxide photocatalysts by modifying their band structures (e.g., band positions and defect states) [143]. A typical case is TiO_2 , where the addition of OV in commercial white TiO_2 endows it with a variety of colors [77,144], including black, gray, green, blue, and red. The appearance of these colors indicates extended light absorption of metal oxide photocatalysts and is generally accompanied by their enhanced performance toward visible-light-driven CO_2 reduction [145–147]. Gao et al. prepared a black titania nanotube array (B- TiO_2) by aluminothermic reduction of anodized TiO_2 nanotube arrays [80]. Ascribing to the significantly extended light absorption range, the optimized B- TiO_2 catalyst demonstrated an excellent CO_2 -to-CO conversion yield of $185.4\text{ }\mu\text{mol g}^{-1}\text{ h}^{-1}$ under visible light irradiation. In addition, an enhanced CH_4 production rate of $16.2\text{ }\mu\text{mol g}^{-1}\text{ h}^{-1}$ was observed on hydrogenated blue titania (H-TiO_{2-x}) under full solar irradiation. The H- TiO_{2-x} prepared by Li-EDA reduction possessed a crystalline core-amorphous shell structure (TiO_2 @ TiO_{2-x}) with abundant OVs, thus exhibiting a significantly enhanced light absorption capability [77]. Due to this enhanced light absorption, these OV-containing metal oxides can also be employed to construct hybrid nanostructures for achieving better photocatalytic CO_2

reduction performance [148,149].

Rationally tuning the OV concentration in metal oxides can enable NIR and even IR light-driven CO_2 reduction reactions. In principle, the bandgap of the photocatalyst should be larger than 1.35 eV to fulfill the CO_2 -to- CO reduction (-0.12 V vs. NHE) and H_2O oxidation to O_2 ($+1.23$ V vs. NHE). Therefore, IR light with wavelengths larger than 920 nm should be incapable of initiating these two reactions simultaneously. To tackle this, Xie and co-workers [137] recently proposed an intermediate band engineering strategy by introducing OV into ultrathin WO_3 atomic layers (Fig. 8a). Theoretical calculations and experimental observations confirmed the formation of an intermediate band in the bandgap of WO_3 when the OV concentration reached a critical value, which endows the sample with light responses extending from visible to IR light (up to 10,000 nm) (Fig. 8b). As a result, the OV-rich WO_3 atomic layers showed obvious quantum efficiencies even up to 1064 nm (Fig. 8c). Following this line of thought, Jiang et al. developed a Z-scheme heterojunction by perovskite CsPbBr_3 and oxygen-deficient WO_3 for NIR light-driven CO_2 reduction [150]. Under NIR light (780–2500 nm) irradiation, electrons stored in the OV state of WO_3 could be excited to the conduction band of WO_3 and then transferred to the CsPbBr_3 site for CO_2 reduction, achieving CO and CH_4 production rates of $69 \mu\text{mol g}^{-1} \text{h}^{-1}$ and $8 \mu\text{mol g}^{-1} \text{h}^{-1}$, respectively.

Concomitant with the extended light absorption, OV as a donor-like defect state can drive up the Fermi level of metal oxide photocatalysts [151], thus potentially modifying their energy band positions for efficient CO_2 reduction. Zhu et al. explored the influence of OV on the photocatalytic CO_2 reduction performance of In_2O_3 catalysts [86]. It was revealed that the introduction of OV could optimize the conduction band position of In_2O_3 , allowing photogenerated electrons to be more energetic to participate in CO_2 -to- CO conversion. A similar phenomenon was observed in a Cu^+ -doped $\text{W}_{18}\text{O}_{49}$ catalyst [152], which exhibited ~ 4 times enhancement in photocatalytic CO_2 reduction performance for CH_4 production. It was reported that the Cu^+ doping could introduce OV and thus change the conduction band edge of $\text{W}_{18}\text{O}_{49}$ to a more negative position.

4.1.2. OV-induced plasmonic effect

In addition to modifying the energy band structure, OV can also extend the light absorption of metal oxides by inducing a unique plasmonic effect. In some heavily OV-doped metal oxides, the large number of electrons accumulated in the OV-induced defect band can absorb incident light and experience intra-band excitation. Interestingly, such an excitation can generate highly energetic “hot” electrons as well as a significant photothermal effect [66], both of which will contribute to the photocatalytic CO_2 reduction process. For example, Zhang and co-workers studied the performance of OV-enriched blue WO_{3-x} porous nanorods for photothermal CO_2 conversion [79]. It turns out that the OV enrichment allowed the sample to exhibit enhanced light absorption in the UV–vis–NIR range due to the LSPR effect. As a result, the OV-enriched sample achieved a remarkably enhanced CH_4 production rate of $\sim 45.7 \mu\text{mol g}^{-1} \text{h}^{-1}$ under solar light irradiation in the absence of any noble-metal co-catalysts or sacrificial agents.

Recently, Li and co-workers [153] developed an oxygen-deficient $\text{Bi}_2\text{O}_{3-x}$ catalyst, which exhibited LSPR absorption in the wavelength range of 600–1400 nm (Fig. 8d,e). Due to the enhanced light absorption, the catalyst displayed an apparent quantum yield of 0.113% for CO production at 940 nm (in the presence of H_2 reductant), which was 4-times higher than that observed at 450 nm. Moreover, the catalytic activity was well maintained across three cyclic tests, with each cycle lasting for 8 h, demonstrating the excellent stability of the plasmonic $\text{Bi}_2\text{O}_{3-x}$ catalyst (Fig. 8f). In another report, Lou and co-workers systematically studied the influence of OV location in Bi_2WO_6 (i.e., W–OV–W and Bi–OV–Bi sites) in inducing the LSPR effect for photocatalytic CO_2 reduction [154]. It was demonstrated that the W–OV–W site could induce an energy state close to the conduction band of Bi_2WO_6 , facilitating photoelectron accumulation for a long lifetime. Therefore, a strong LSPR absorption in the 500–1400 nm region was observed for Bi_2WO_6 with W–OV–W sites, which is absent for Bi_2WO_6 with Bi–OV–Bi sites. Benefiting from the LSPR-induced high-energy hot electrons, the Bi_2WO_6 with W–OV–W sites exhibited a CH_4 production rate of $9.95 \mu\text{mol g}^{-1} \text{h}^{-1}$, which is 26-fold higher than that of Bi_2WO_6 .

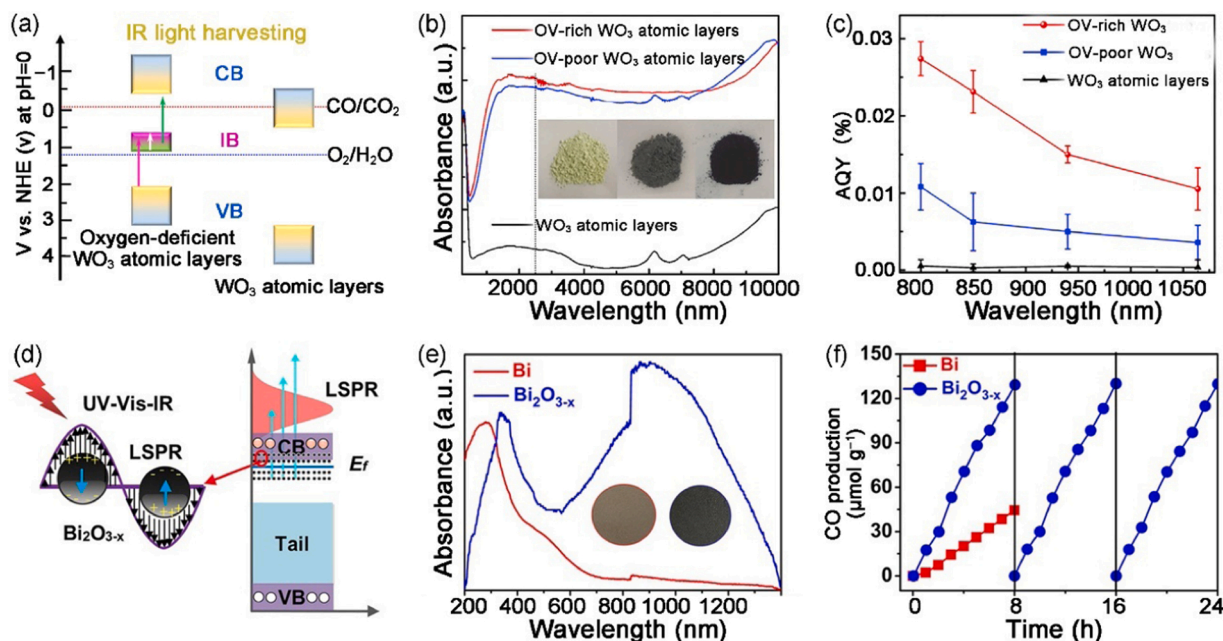


Fig. 8. (a) Schematic illustration for the electronic band structures of WO_3 and oxygen-deficient WO_3 (V_O -rich WO_3) atomic layers. VB, CB, and IB represent the valence band, conduction band, and intermediate band, respectively. (b) Optical absorption spectra of V_O -rich and V_O -poor WO_3 atomic layers. (c) Apparent quantum efficiency measurements for photocatalytic CO_2 reduction over WO_3 , V_O -rich, and V_O -poor WO_3 atomic layers. Reproduced with permission from Ref. [137]. Copyright 2018, Elsevier B.V. (d) Schematic illustration for the LSPR excitation process on $\text{Bi}_2\text{O}_{3-x}$. (e) UV-vis-IR absorption spectra of Bi and $\text{Bi}_2\text{O}_{3-x}$. The inset shows the photos of Bi (left) and $\text{Bi}_2\text{O}_{3-x}$ (right). (f) Photocatalytic CO_2 -to- CO conversion performance test for Bi and $\text{Bi}_2\text{O}_{3-x}$ samples. Reproduced with permission from Ref. [153]. Copyright 2020, John Wiley & Sons, Inc.

with Bi–OV–Bi sites ($0.37 \mu\text{mol g}^{-1} \text{h}^{-1}$).

The construction of heterojunction is effective in stabilizing the LSPR excitation of metal oxides by maintaining a high free-electron density under light irradiation [155,156], thereby facilitating the LSPR-mediated CO_2 reduction [157]. Li and co-workers constructed a heterostructure between TiO_2 mesocrystals and plasmonic WO_{3-x} nanowires for co-catalyst-free photocatalytic CO_2 reduction [158]. The $\text{TiO}_2/\text{WO}_{3-x}$ hybrid achieved a much higher CH_4 production rate ($16.3 \mu\text{mol g}^{-1} \text{h}^{-1}$) than TiO_2 ($3.5 \mu\text{mol g}^{-1} \text{h}^{-1}$) and WO_{3-x} ($8.0 \mu\text{mol g}^{-1} \text{h}^{-1}$) under UV–vis light irradiation. Mechanism studies suggested that the continuous photoelectron injection from TiO_2 to WO_{3-x} increased the free carrier density of WO_{3-x} , resulting in more stable LSPR absorption and hot electron generation. Similarly, a heterojunction by WO_{3-x} and MoO_{3-x} with abundant OVs was prepared, which displayed significantly enhanced hot electron generation and thus CO_2 -to- CO conversion performance under UV–vis–NIR light irradiation [159]. In another recent report, Lou and co-workers further demonstrated the plasmonic thermal effect-enhanced CO_2 reduction by coupling plasmonic WO_{3-x} with pyroelectric black phosphorous (BP) [160]. Under visible and NIR light irradiation, the local high temperature brought about by the plasmonic thermal effect of WO_{3-x} triggered the pyroelectric effect of BP, inducing the continuous electron injection from pyroelectric BP to WO_{3-x} . As a result, the plasmonic BP/ WO_{3-x} hybrid exhibited a CO production rate of $26.1 \mu\text{mol g}^{-1} \text{h}^{-1}$, 7- and 17-fold higher than those of WO_{3-x} and BP, respectively.

In short, the introduction of OV can significantly extend the light absorption range of metal oxides by tuning their band structures (i.e., band positions and defect states) and inducing a plasmonic effect. It is worth mentioning that the extended light absorption range does not necessarily lead to enhanced photocatalytic activity. Taking black and gray TiO_2 as an example, black TiO_2 has a broader light absorption range than gray TiO_2 ; however, the latter generally features higher intrinsic photocatalytic activity (in the absence of co-catalysts). In fact, the mismatch between the performance and light absorption capability of the photocatalyst is within expectations because light absorption is only one of the three basic steps (i.e., light absorption, charge carrier separation, and surface reaction) that determine photocatalytic performance. In addition, in OV-containing plasmonic metal oxides, the LSPR absorption is due to the intra-band excitation of electrons in the OV-induced defect band. Therefore, both OV-induced inter-band and intra-band excitations exist in plasmonic metal oxides (e.g., WO_{3-x}) and will potentially affect the catalytic reaction. However, a high electron concentration in the OV-induced defect band is required for maintaining a strong intra-band excitation [154]. To this end, the photocatalytic system should have i) sufficient energy input (e.g., UV light) for electron generation and ii) an efficient charge transfer channel for electron accumulation in the OV-induced defect band. Only after fulfilling these criteria, the OV-induced plasmonic effect can contribute to catalysis by providing highly energetic electrons (hot electron effect) and/or local high temperatures (i.e., photothermal effect).

4.2. Oxygen vacancy-enhanced charge separation

As a donor-like defect, OV can introduce a defect band near the conduction band of metal oxide photocatalysts. The defect band brought about by OV can serve as a trapping site for photogenerated electrons in the conduction band, thereby alleviating the unfavorable recombination of photogenerated charge carriers and facilitating their separation. Taking this into account, numerous researchers have successfully employed OV to maneuver the charge transfer behaviors in pristine metal oxide and metal oxide-based hybrid nanostructures for efficient CO_2 reduction.

4.2.1. OV in mono-component metal oxides

The role of OV in promoting charge carrier separation has been well-studied by previous works. Wheeler et al. systematically studied the role

of OV in introducing a mid-bandgap state in hydrogen-treated TiO_2 (H: TiO_2) using ultrafast transient adsorption [161]. Under UV light excitation, the charge carrier relaxation in H: TiO_2 was slower than untreated TiO_2 , indicating the prolonged charge carrier lifetime. In another work, Zhang et al. used EPR to study the light excitation behaviors of OV-rich nanoporous TiO_{2-x} that contains small anatase nanoparticles with high surface area [162]. It was observed that the TiO_{2-x} nanoparticles displayed shallow charge traps associated with Ti/O-vacancies, which remained separated and stable for several minutes after light exposure. The long-lived charge separation state allowed TiO_{2-x} to exhibit a favorable CH_4 production rate of $26.12 \mu\text{mol g}^{-1} \text{h}^{-1}$.

Over time, it has been realized that the function of OV in influencing charge carrier behaviors is largely determined by its locations [163]. A typical case is for bulk and surface OVs, where the latter generally has higher stability [95]. Kong et al. reported a markedly improved separation efficiency of photogenerated electrons and holes with the decreasing relative concentration of bulk OV to surface OV in TiO_2 nanocrystalline [163]. Furthermore (Fig. 9a), Yang and co-workers [164] studied the role of bulk and surface OVs in photocatalytic CO_2 reduction and observed an enhanced photocatalytic performance with an increase in the ratio of surface OV (SO) to bulk OV (i.e., single-electron-trapped oxygen vacancy, SETOV). It was revealed that the OV in the surface disorder layer (i.e., surface OV) could promote charge carrier separation, while bulk OV served as recombination centers for photogenerated electrons and holes. However, both bulk and surface OVs can contribute to enhanced visible light absorption of TiO_2 . Therefore, the TiO_2 sample with the co-existence of surface and bulk OV (TiO_2 -SBO) achieved the highest photocatalytic CO_2 reduction performance for CH_4 production under both UV and visible light irradiation (Fig. 9b). It is worth noting that the enhanced light absorption and the inhibited charge carrier separation caused by bulk OV will jointly determine whether there is a final positive or negative effect on the photocatalytic CO_2 reduction performance, especially when under UV light irradiation.

The synergy of OV with other surface sites (e.g., hydroxyl groups and metal vacancies) can further promote charge carrier separation and enhance photocatalytic performance [165]. Xiao et al. successfully modified OV and surface hydroxyl groups onto the TiO_2 surface ($\text{TiO}_{2-x} \cdot 2x\text{OH}$), where the OV and the hydroxyl groups with high electron density were able to trap electrons and holes, respectively [166]. The $\text{TiO}_{2-x} \cdot 2x\text{OH}$ sample was synthesized by high-temperature calcination of TiO_2 in the presence of ionic liquid, where the breaking of the Ti–O–Ti bond during high-temperature treatment leads to the formation of OV and surface hydroxyl groups on nearby Ti atoms ($\text{TiO}_2 + x \text{H}_2\text{O} \rightarrow \text{TiO}_{2-x} \cdot 2x\text{OH}$). Through femtosecond transient absorption measurements, Ozin and co-workers also observed a longer excited-state lifetime in the In_2O_3 catalyst co-modified with OV and hydroxyl groups ($\text{In}_2\text{O}_{3-x}(\text{OH})_y$) [167]. This observation was a result of improved charge separation due to the defect states induced by OV (shallow donor state, electron trapping) and hydroxyl groups (shallow acceptor state, hole trapping) in the bandgap of $\text{In}_2\text{O}_{3-x}(\text{OH})_y$. As a result, the $\text{In}_2\text{O}_{3-x}(\text{OH})_y$ with OV and hydroxyl groups on its surface functioned as an effective gas–solid-phase photocatalyst for CO_2 -to- CO reduction in the presence of H_2 .

In addition to serving as an electron trapping site, OV can also indirectly contribute to the charge carrier separation process by assisting in the formation/stabilization of the electric field within the metal oxide photocatalyst. Recently, Ma and co-workers [168] reported the synergy of OV and ferroelectric polarization in accelerating charge carrier separation and promoting CO_2 photoreduction on oxygen-deficient polarized $\text{Bi}_3\text{NbTiO}_9$ nanosheets (BNT-OVP) (Fig. 9c). Interestingly, the authors observed a pinning effect of OV on the ferroelectric domains of BNT-OVP. In other words, the strong electric field induced by the superb ferroelectric polarization could be well maintained by OV to facilitate the charge carrier separation within the BNT-OVP nanosheets. Compared to OV-deficient polarized $\text{Bi}_3\text{NbTiO}_9$ nanosheets (BNT-P), the

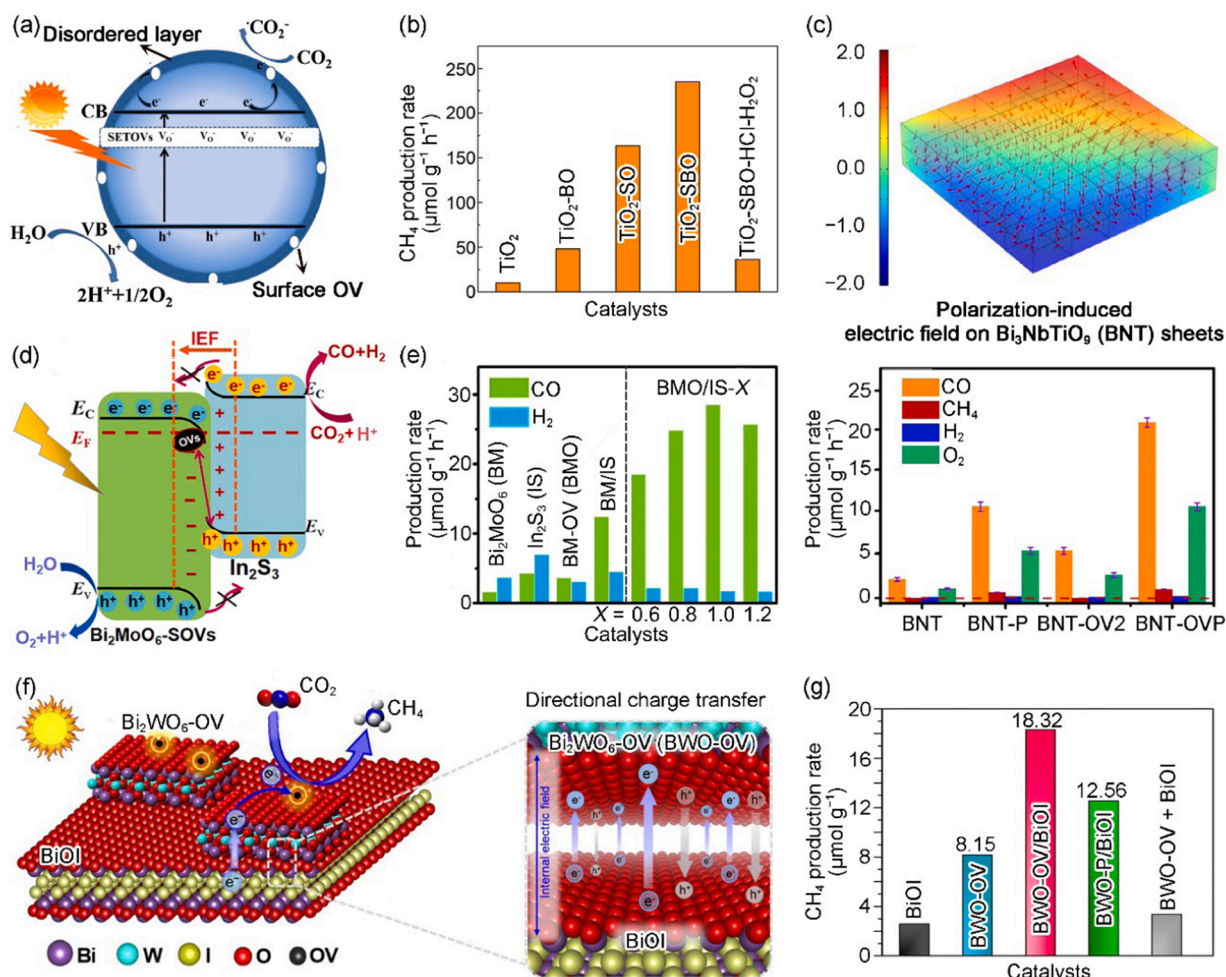


Fig. 9. (a) Schematic illustration for the photocatalytic CO₂ reduction process over the TiO₂ sample (TiO₂-SBO) containing both surface and bulk OVs. (b) Photocatalytic CH₄ production rates over different TiO₂ samples under UV light irradiation. Reproduced with permission from Ref. [164]. Copyright 2017, Elsevier B.V. (c) COMSOL simulation of polarization-induced electric field on polarized Bi₃NbTiO₉ (BNT-P) nanosheets. And the photocatalytic production rates of CO, CH₄, and H₂ over BNT, BNT-P, oxygen-deficient Bi₃NbTiO₉ (BNT-OV), and polarized BNT-OV (BNT-OVP). Reproduced with permission from Ref. [168]. Copyright 2021, Springer Nature. (d) Schematic illustration for the charge transfer mechanism over the Z-scheme oxygen-deficient Bi₂MoO₆/In₂S₃ heterojunctions. IEF: internal electric field. (e) Photocatalytic CO and H₂ production rates over different samples. Reproduced with permission from Ref. [180]. Copyright 2021, Elsevier B.V. (f) Schematic illustration for the OV-directed charge transfer from BiOI to OV-rich Bi₂WO₆ (BWO-OV). (g) Photocatalytic CH₄ production rate over BiOI, BWO-OV, BWO-OV/BiOI heterojunction, OV-deficient heterojunction (BWO-P/BiOI), and physical mixture of BWO-OV and BiOI. Reproduced with permission from Ref. [183]. Copyright 2021, Elsevier B.V.

BNT-OVP demonstrated nearly a 2-fold enhancement in CO (20.9 μmol g⁻¹ h⁻¹) and CH₄ (~10.0 μmol g⁻¹ h⁻¹) production under AM 1.5 G light irradiation.

4.2.2. OV in metal oxide-based hybrid nanostructures

The introduction of OV brings about more complex but fascinating influences on the charge transfer/separation behaviors in metal oxide-based hybrid nanostructures. Theoretically, an increase in the density of electron donor-like defect states (e.g., OV) can lead to a decrease in the work function of metal oxides [151]. With this in mind, Zheng et al. [169] successfully utilized OV to tune the energy match level between TiO₂ and polyoxometallate (POM), achieving multi-electron transfer from the OV-rich TiO₂ to POM (H₃PW₁₂O₄₀, HPW). With this supplement of electrons, the 5 wt% HPW-modified defective TiO₂ exhibited the highest selectivity (still < 4%) for CH₄ production. Furthermore, Chong et al. introduced a MgAl layered double oxide (MgAl-LDO) into the interlayer between Pt nanoparticles and TiO₂ substrate to mediate electron transfer within the hybrid [170]. The OV arising from MgAl-LDO deposition could suppress the recombination of photo-generated charge carriers, enabling multi-electron transfer from TiO₂ to

Pt sites. As a result, the MgAl-LDO introduction enhanced the CO and CH₄ yield by 2 and 11 times, respectively, with a greatly enhanced selectivity toward CH₄ production.

The role of OV in mediating the electron transfer pathway has also been observed in OV-containing Z-scheme heterojunctions [171,172]. Z-scheme heterojunction can facilitate the separation of photogenerated electrons and holes while retaining their high redox capabilities [173–175]. Therefore, the introduction of OV to assist or induce Z-scheme charge transfer is highly promising for constructing high-performance photocatalysts for CO₂ reduction [176–179]. Yu et al. recently developed a hierarchical Bi₂MoO₆/In₂S₃ heterostructure with abundant OVs for efficient CO₂ photoreduction [180]. Theoretical calculations and in situ XPS observations confirmed a Z-scheme electron transfer pathway (Fig. 9d), where energetic electrons and holes could remain in the conduction band of In₂S₃ and valence band of Bi₂MoO₆, respectively, to participate in photocatalytic CO₂ reduction with H₂O. Based on experimental results, the authors further proposed that the OV on Bi₂MoO₆ can accelerate the Z-scheme electron transfer from Bi₂MoO₆ to In₂S₃. As such, the optimized nanohybrid demonstrated a much higher yield of CO (28.5 μmol g⁻¹ h⁻¹) than that of defect-free

$\text{Bi}_2\text{MoO}_6/\text{In}_2\text{S}_3$ heterojunction ($\sim 12.0 \mu\text{mol g}^{-1} \text{h}^{-1}$) (Fig. 9e). In another study of H_2O oxidation using the Z-scheme heterojunction composed of BiOI and OV-enriched CeO_2 , Sultana et al. demonstrated that the OV could mediate the Z-scheme electron transfer from the conduction band of CeO_2 to the valence band of BiOI [181].

In addition to mediating electron transfer within the hybrid nanostructures, OV can also direct the electron transfer pathway for promoted charge separation [182–185]. Using Na-EDA as a selective reductant, Hwang et al. developed a heterophase junction between disordered anatase and ordered rutile (A_d/R_o) TiO_2 [186]. The OV in the disordered anatase not only extends the light absorption range of the hybrid but also serves as an electron trapping site to drive the electron transfer from R_o to A_d . As a result, the A_d/R_o TiO_2 displayed the highest CH_4 production rates of $3.983 \mu\text{mol g}^{-1} \text{h}^{-1}$ under visible light irradiation, which was even better than that of metal co-catalyst loaded commercial P25. Kong et al. developed a 2D/2D heterojunction between BiOI and OV-rich Bi_2WO_6 , in which the abundant OVs in Bi_2WO_6 induced a directional electron transfer from BiOI to Bi_2WO_6 (Fig. 9f) [183]. As a result, the OV-rich heterojunction exhibited an enhanced CH_4 production rate ($18.32 \mu\text{mol g}^{-1}$) compared to the OV-deficient $\text{Bi}_2\text{WO}_6/\text{BiOI}$ heterojunction ($12.56 \mu\text{mol g}^{-1}$) (Fig. 9g). Similarly [187,188], Miao et al. developed a co-catalyst BiO_{2-x} coupled g- C_3N_4 photocatalyst [189], which showed a CO production rate ($42.29 \mu\text{mol g}_{\text{cat}}^{-1}$) 3.8 times that of pure g- C_3N_4 . Sun et al. also developed a highly efficient photocatalyst consisting of reduced graphene oxide (rGO) and BiO quantum dots (QDs) [190]. The apparent quantum efficiency of rGO-BiO QDs reached 4.2% at 300 nm, which was ~ 15 times that of rGO- TiO_2 QDs (0.28%) under the same conditions. Mechanism studies suggested the role of OV in inducing a unique circular electron transfer pathway, i.e., from the conduction band of BiO to rGO and then to being trapped by the OV site on BiO. In other words, electrons were stored in rGO before participating in photocatalytic CO_2 reduction at the OV site.

In short, the electron-trapping effect of OV makes it a useful tool for regulating charge separation behaviors in metal oxide-based photocatalysts (Fig. 10). Tremendous efforts have been devoted to understanding the influence of the state of OV (e.g., locations) on the charge separation process. Despite the deeper understanding obtained, there are still some areas of contention that need to be clarified in future works. For example, in the OV-containing heterojunctions, it is commonly believed that OV at the interface can mediate the electron transfer between the two components. However, the interfacial OV can also be intuitively regarded as the bulk OV, which is supposed to be unfavorable for the charge separation process. For example, Zhang et al. reported that the OV at the interface between TiO_2 and perovskite can slow down charge transfer and significantly accelerate charge recombination at the interface [191]. A rational photocatalyst design with controllable ratios of interface OV to surface OV is hence necessary to

unravel the role of OV in metal oxide-based heterojunction photocatalysts.

4.3. OV-promoted surface CO_2 conversion reaction

The introduction of OV via the removal of oxygen atoms from the metal oxide matrix is generally accompanied by the formation of coordinatively unsaturated metal centers (M_{CUS}). In principle, these M_{CUS} -OV pairs can serve as ideal sites for molecular (e.g., CO_2) chemisorption. Furthermore, the ability of the neutral M_{CUS} -OV pair to accumulate electrons under light irradiation allows them to be an efficient channel for electron transfer between the metal oxide and adsorbed CO_2 molecules. In addition, the OV can potentially modify the electronic structure of other active sites on the metal oxide surface, thus indirectly contributing to the surface CO_2 conversion process. Hence, promoted surface CO_2 conversion reaction is commonly observed on OV-containing metal oxide photocatalysts.

4.3.1. OV as the active site for CO_2 adsorption and activation

The adsorption of CO_2 on the catalyst surface is indispensable for its activation and conversion. Generally, CO_2 can be adsorbed with a configuration of carbon coordination, oxygen coordination, or mixed coordination (i.e., using both carbon and oxygen atoms) [6]. The presence of OV on metal oxide-based photocatalysts has significant influences on the adsorption behaviors of CO_2 [58,192,193]. Sorescu et al. employed dispersion-corrected density functional theory to study the adsorption of CO_2 on the anatase $\text{TiO}_2(101)$ surface with bridging OVs [194]. It was reported that the most stable configuration of CO_2 adsorption was a bent CO_2 structure bound to two surface Ti atoms adjacent to the bridging OV. Moreover, subsurface OVs were found to further enhance the binding of CO_2 molecules to the surface. The OV-enhanced CO_2 adsorption not only accelerates the photocatalytic reaction [97,195,196] but also allows the reaction to be carried out at low CO_2 concentrations. Chen et al. recently employed OV-rich NiO nanoplatelets (r-NiO) to reduce diluted CO_2 (10 vol%) under visible light irradiation ($>400 \text{ nm}$) [89]. The r-NiO nanoplatelets were synthesized by calcination under Ar and then integrated with a Ru-based photosensitizer, enabling visible-light-driven CO_2 reduction (in the presence of TEOA as a hole sacrificial agent). Benefiting from the strong adsorption of CO_2 on OV sites, the r-NiO exhibited nearly a 2-fold enhancement in the production rate ($6.28 \text{ mmol g}^{-1} \text{h}^{-1}$) of CO from diluted CO_2 reduction compared to that of normal NiO ($3.94 \text{ mmol g}^{-1} \text{h}^{-1}$). The role of OV in promoting diluted CO_2 reduction is vital for its practical application.

When CO_2 is adsorbed at the OV site, it can accept electrons from adjacent metal atoms [197] and undergo activation and dissociation for its subsequent transformation [198–200]. Lee et al. [201] employed

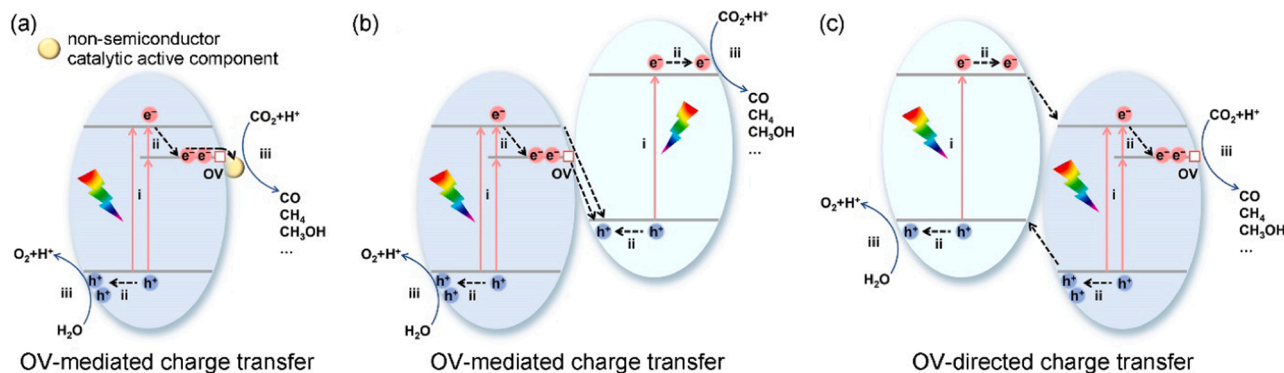


Fig. 10. Schematic illustration for OV-mediated charge transfer (a) between metal oxides and non-semiconductor catalytic active components (e.g., metal nanoparticles) and (b) within semiconductor heterojunction. (c) Schematic illustration of OV-directed charge transfer. The energy band bending at the contact interface and the recombination process of photogenerated electrons and holes are not shown in the figure.

STM to investigate the dissociation of CO_2 adsorbed at the OV site on the $\text{TiO}_2(110)$ surface at the single-molecular level (Fig. 11a,b). It was demonstrated that the electron injection from the STM tip into the adsorbed CO_2 induced the dissociation of CO_2 , which was accompanied by the healing of the OV site. The intermediate negative ion ($\bullet\text{CO}_2^-$) was considered to be essential for CO_2 activation and dissociation. In a subsequent theoretical study [202], Chu et al. reported the formation of intermediate $\bullet\text{CO}_2^-$ at the OV site on rutile $\text{TiO}_2(110)$ by single electron transfer from the conduction band of TiO_2 to the adsorbed CO_2 molecule. It was shown that if the intermediate $\bullet\text{CO}_2^-$ possessed a lifetime longer than 12 fs, it can excite the bending and asymmetric stretching vibrations with the assistance of OV (Fig. 11c). During this process, the CO_2 LUMO could be sufficiently stabilized below the conduction band minimum of TiO_2 , allowing it to trap photoexcited electrons and dissociate.

The activation and dissociation processes of CO_2 on OV have also been experimentally evidenced in recent reports [203,204]. Wang et al. reported the dissociation of CO_2 into carbon and oxygen over an OV-rich amorphous zinc germanate ($\alpha\text{-Zn-Ge-O}$) photocatalyst under xenon lamp irradiation [205]. EPR and isotope labeling studies confirmed the role of OV and photogenerated electrons in promoting CO_2 dissociation; meanwhile, photogenerated holes can reoxidize surface oxygen atoms

into O_2 to regenerate OV on the photocatalyst surface. Similarly, Liu et al. carried out photocatalytic CO_2 reduction studies on three TiO_2 nanocrystal polymorphs (anatase, rutile, and brookite) that were engineered with defect-free and OV-rich surfaces [206]. The helium treatment of the TiO_2 nanocrystals at moderate temperatures created OV and Ti^{3+} on anatase and brookite but not on rutile. In situ diffuse-reflectance infrared Fourier transform spectroscopy (DRIFTS) analyses showed that the $\bullet\text{CO}_2^-$ intermediate could only be observed on OV-containing samples (i.e., anatase and brookite TiO_2), in agreement with the OV-associated single-electron transfer process. Following this line of thought, Xie and co-workers successfully achieved the photofixation of CO_2 with methanol to long-chain chemicals (i.e., dimethyl carbonate, DMC) on OV-rich Bi_2O_3 nanosheets (Fig. 11d) [207]. Both in situ DRIFTS and XPS revealed that the OV could provide abundant localized electrons for the enhanced generation of $\bullet\text{CO}_2^-$, which was considered the rate-determining step for CO_2 photofixation. As a result, the CO_2 conversion over OV-rich Bi_2O_3 reached $\sim 18\%$, 9 times higher than that of OV-poor Bi_2O_3 (Fig. 11e).

In addition to the promoted CO_2 adsorption and activation, OV can also alter the CO_2 conversion pathway. Liu et al. investigated the CO_2 reduction pathway on defective anatase $\text{TiO}_2(101)$ surface with density functional theory calculation [208]. It was reported that the OV not only

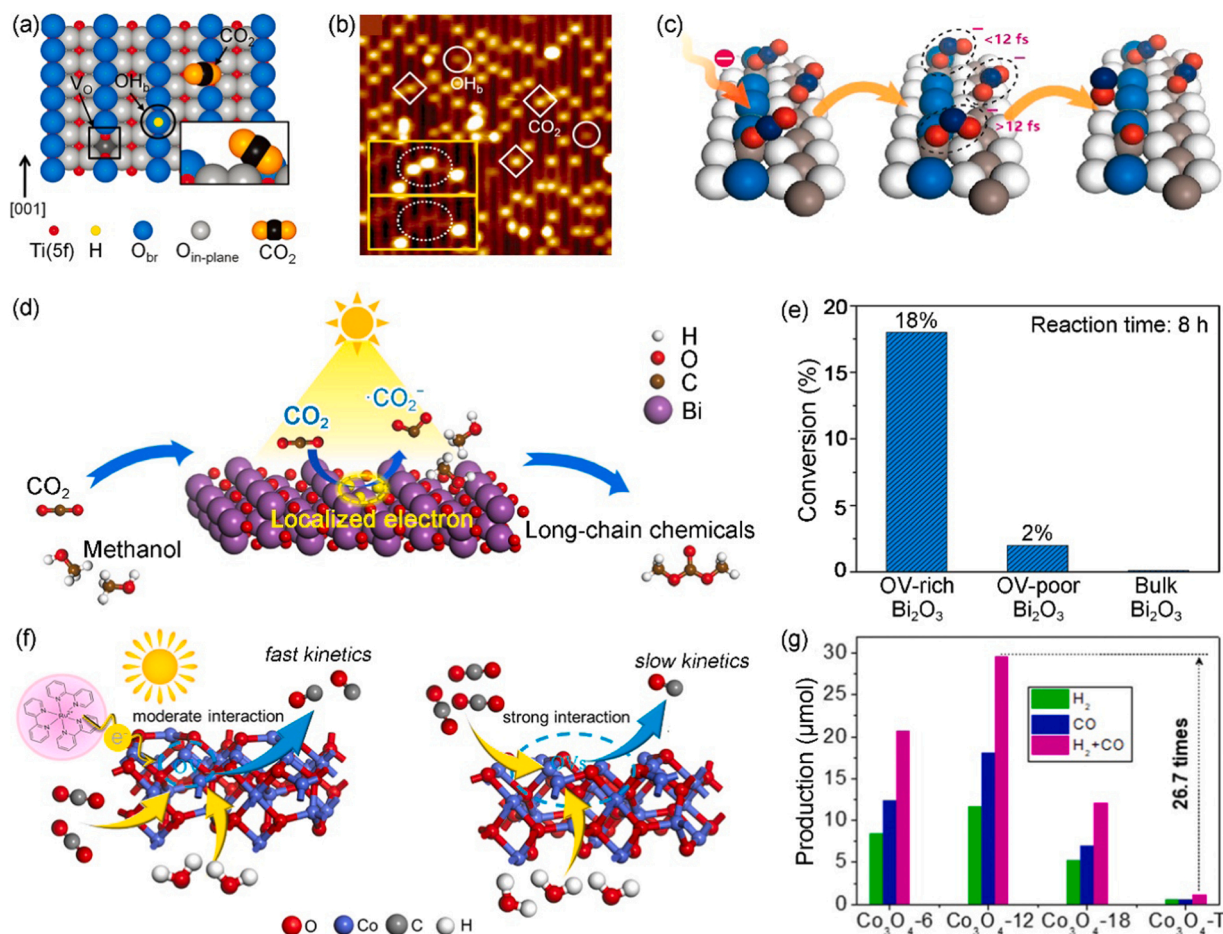


Fig. 11. (a) Schematic illustration of the oxygen vacancy defect (OV) and the adsorbed bridging hydroxyl (OH_b) and CO_2 molecule on the reduced $\text{TiO}_2(110)$ surface. (b) STM image of the $\text{TiO}_2(110)$ surface after adsorption of CO_2 at 55 K, showing the occupation of all the OV sites by CO_2 . CO_2 and OH_b features are highlighted with diamonds and circles, respectively. The insets show the OV site with and without adsorbed CO_2 . Reproduced with permission from Ref. [201]. Copyright 2011, American Chemical Society. (c) Schematic illustration for the photoexcited electrons-driven CO_2 activation process on the OV site of rutile $\text{TiO}_2(110)$ surface. Reproduced with permission from Ref. [202]. Copyright 2020, American Chemical Society. (d) Schematic illustration for the photocatalytic reduction of CO_2 to long-chain chemicals over Bi_2O_3 nanosheets with rich oxygen vacancies (OV-rich Bi_2O_3). (e) Photocatalytic CO_2 reduction performance of OV-rich Bi_2O_3 , OV-poor Bi_2O_3 , and bulk Bi_2O_3 at 373 K under xenon lamp irradiation. Reproduced with permission from Ref. [207]. Copyright 2019, Springer Nature. (f) Schematic illustration for photocatalytic CO_2 reduction process over OV-containing Co_3O_4 . (g) Photocatalytic CO_2 reduction performance of various samples under visible light irradiation ($\lambda \geq 420$ nm). Reproduced with permission from Ref. [211]. Copyright 2021, Elsevier B.V.

promoted CO_2 adsorption and activation but also stabilized CO and other intermediates for the subsequent hydrogenation and production of CH_4 . Furthermore, Ji et al. demonstrated that the hydrogenation of surface intermediates could occur at both the surface Ti and the OV sites, while deoxygenation processes largely take place at the OV site [209]. During the reduction of CO_2 over defective anatase $\text{TiO}_2(101)$, the CO_2 first occupied the OV site to undergo deoxygenation and generate CO. It subsequently experiences fast hydrogenation to hydrocarbon products. Following this work, the authors further studied the role of H_2O in the photocatalytic CO_2 reduction reaction over the defective anatase $\text{TiO}_2(101)$ [210]. Interestingly, it was found that H_2O directly donated protons to CO_2 and other reaction intermediates adsorbed at the OV site while the remaining OH^- recombined with a surface-adsorbed proton to generate a new H_2O molecule. This pathway is distinctly different from the traditional understanding that H_2O first experiences photooxidation to produce protons, which then participate in CO_2 hydrogenation and reduction. However, the possibility of H_2O participating in CO_2 reduction by combining a proton to form a hydrated proton (e.g., H_3O^+) should also be duly considered.

Despite the significance of OV in promoting CO_2 adsorption, activation, and conversion, rationally tuning the amount of OV is still essential. Zhang et al. [211] reported that the Co_3O_4 catalyst decorated with moderate OV amounts exhibited the highest performance for CO production in the presence of TEOA as a sacrificial agent (Fig. 11f,g). It was reported that excessive or insufficient OVs on the Co_3O_4 surface would lead to sluggish surface reaction kinetics. Excessive amounts of OVs lead to overly strong interactions between catalysts and substrate molecules, thus blocking the catalytic cycle. On the other hand, the

substrate CO_2 cannot be efficiently activated if the interactions are too weak (i.e., when there are insufficient OVs). In addition to CO_2 adsorption, an excessive amount of OVs can also impede the activation process of CO_2 adsorbed at the OV site. Zhao et al. reported that large amounts of OVs on the anatase TiO_2 nanorod surface led to severe charge carrier recombination, significantly limiting the single-electron transfer associated CO_2 activation process [212]. It was also demonstrated that atomic layer deposition (ALD) could be employed as an effective tool to passivate the excessive surface OV states.

4.3.2. OV-based active site design

During photocatalytic CO_2 reduction, the coordinatively unsaturated metal centers near OV also contribute to the stabilization of CO_2 reduction intermediates, constituting the $\text{M}_{\text{CUS}}\text{-OV}$ pair sites. Yan and co-workers reported the Nb-OV pair site-assisted CO_2 conversion on mesoporous black $\text{Nb}_2\text{O}_{5-x}$ catalyst [213]. It was shown that the Nb-OV pair site not only assisted the adsorption and dissociation of CO_2 but also facilitated the stabilization of $^*\text{CO}$ intermediates and their transformation into $^*\text{CHO}$ (Fig. 12a). Therefore, as compared to defect-free white Nb_2O_5 (0%), the black $\text{Nb}_2\text{O}_{5-x}$ photocatalyst achieved a higher CH_4 selectivity (64.8%) from CO_2 reduction (Fig. 12b).

Metal modification can also efficiently influence the photocatalytic CO_2 reduction process by modifying the $\text{M}_{\text{CUS}}\text{-OV}$ pair site [65,214]. The introduced metal centers can stabilize the adjacent OV sites [215–217] and, together with the OV, promote CO_2 adsorption and activation [218–220]. For instance, Chen et al. reported the enhanced CO_2 to CH_4 conversion over OV-rich Zn-doped ultrathin CoO layer [221]. The Zn-OV pair site promoted the formation of $^*\text{CO}$

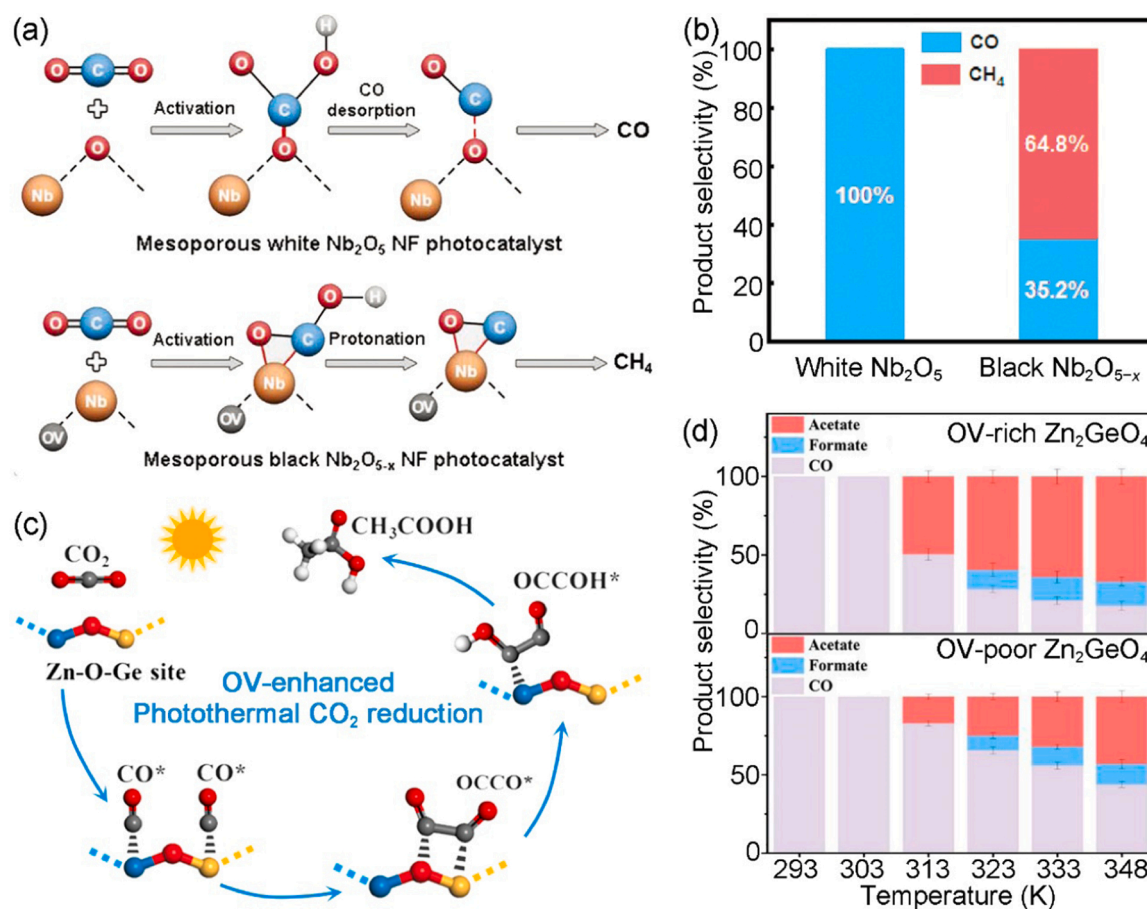


Fig. 12. (a) Schematic illustration for the photocatalytic CO_2 reduction routes over white and black Nb_2O_5 . Reproduced with permission from Ref. [213]. Copyright 2022, John Wiley & Sons, Inc. (c) Schematic illustration for the OV-enhanced photocatalytic CO_2 reduction to acetic acid process over Zn_2GeO_4 . (d) Product selectivities for photocatalytic CO_2 reduction over OV-rich and OV-poor Zn_2GeO_4 nanobelts in simulated air at different temperatures. Reproduced with permission from Ref. [239]. Copyright 2021, American Chemical Society.

intermediates while the π -back-bonding between Zn dopant and $^*\text{CO}$ stimulated the CH_4 evolution. As a result, the OV-rich Zn-CoO layer exhibited enhanced CO_2 reduction efficiency ($26.8 \mu\text{mol g}^{-1} \text{h}^{-1}$) and CH_4 selectivity (63.8%) compared to $7.2 \mu\text{mol g}^{-1} \text{h}^{-1}$ and 24.6% for the undoped OV-CoO layer. However, the photocatalyst efficiencies for OV-rich Zn-CoO and undoped OV-CoO reduced to 83.4% and 52.8% during the second catalytic cycle, respectively. This suggests that the OV on the catalyst surface was consumed during the photocatalytic reaction.

The role of metal dopants in stabilizing CO_2 reduction intermediates has also been observed in Cu^+ -modified TiO_2 [222–224]. Liu et al. reported that the Cu^+ dopant could assist in the destabilization and dissociation of the $^*\text{CO}_2^-$ intermediate formed at the adjacent Ti^{3+} -OV site due to the strong interaction between Cu^+ and $^*\text{CO}$ intermediates [225]. Furthermore, an over 30 times increase in CH_4 production rate ($8.68 \mu\text{mol g}^{-1} \text{h}^{-1}$) was observed over Cu_2O cluster-loaded TiO_2 nanosheets compared to the parent TiO_2 [226]. Extending from this, Wang et al. recently developed an $\text{Au}/\text{TiO}_{2-x}$ hybrid, where the slightly positively-charged Au formed under plasmonic excitation can stabilize the in situ generated $^*\text{CO}$ from the OV site [227]. Notably, it was demonstrated that the $^*\text{CO}$ stabilization allowed for efficient C–C coupling over the $\text{Au}/\text{TiO}_{2-x}$ hybrid, achieving a 20% selectivity toward C_2H_6 production ($0.66 \mu\text{mol g}^{-1} \text{h}^{-1}$) from photocatalytic CO_2 reduction.

Introducing additional active sites for enhanced H_2O activation and proton production is another promising pathway for promoting photocatalytic CO_2 reduction [228–231]. In this regard, Pt has commonly been considered the ideal choice for H_2O activation [232–234]. Yu and co-workers developed a Pt nanoparticles-loaded OV-rich Ga_2O_3 for enhanced photocatalytic CO_2 -to- CO conversion [235]. It was reported that the hydrogen atoms formed from H_2O reduction at the Pt site could be transferred to the adsorbed CO_2 molecules at the OV site on Ga_2O_3 . As a result, the OV-rich Pt/ Ga_2O_3 exhibited a substantially enhanced CO production rate ($21.0 \mu\text{mol h}^{-1}$) compared to that of OV-poor Pt/ Ga_2O_3 ($3.9 \mu\text{mol h}^{-1}$) under xenon lamp irradiation. In addition, it was recently demonstrated that thermal coupling could facilitate the electron transfer from OV to Pt sites, leading to promoted H_2O activation and hydrogen-assisted CO_2 reduction. During the thermally coupled photocatalytic CO_2 reduction, an enhanced hydrogen splitting was observed over Pt/ TiO_{2-x} with smaller Pt nanoparticles (2.33 nm vs. 4.06 nm), which is beneficial for the subsequent CO_2 activation by hydrogenation [236]. Unsurprisingly, a 43-fold increase in CO_2 conversion rates was observed when the system temperature was increased from 298 to 393 K. With that in mind, Cai et al. recently developed an OV-rich Au/TiO_2 photocatalyst, where the plasmonic effect of Au can locally provide high temperatures to induce the thermally coupled CO_2 reduction over the OV site [237]. The synergistic effect between OV and other active sites on the photocatalyst can potentially lead to higher performance for CO_2 reduction. However, the rational integration of the multiple active sites to maximize their synergistic effect remains challenging.

4.3.3. OV-assisted active site design

Apart from acting directly as the active site for CO_2 reduction, OV can also indirectly contribute to CO_2 reduction by affecting the electronic structures of actual catalytic active sites [238]. Recently, Xie and co-workers reported the OV-enhanced photothermal CO_2 reduction for acetate production over OV-rich Zn_2GeO_4 nanobelts [239]. DFT calculations demonstrated that the asymmetric Zn–O–Ge site endowed the two neighboring $^*\text{CO}$ molecules with different charge densities, which was beneficial for their coupling and hence the production of $^*\text{OCCO}$ intermediates (Fig. 12c). Moreover, the OV in the material further enhanced the asymmetry of the Zn–O–Ge site, thus leading to improved production of $^*\text{OCCO}$ and its hydrogenation to $^*\text{OCCOH}$ intermediates. The OV-rich Zn_2GeO_4 nanobelts displayed an acetate production yield of $12.7 \mu\text{mol g}^{-1} \text{h}^{-1}$ with a selectivity of 66.9% in a simulated air

atmosphere at 348 K, significantly outperforming that of OV-poor Zn_2GeO_4 (production yield: $1.4 \mu\text{mol g}^{-1} \text{h}^{-1}$, selectivity: 43.1%) (Fig. 12d).

Beyond that, the unique geometry and electronic structures of OV enable it to be an excellent site for the deposition of catalytically active components [240,241]. For instance, the redox reaction between the electrons trapped at the OV sites and the metal salt precursors can result in the deposition of metal nanoparticles on the defective metal oxide support [242]. Following the OV-assisted deposition, the intimate contact between OV-containing metal oxide and the deposited catalytic active components allows the formation of a high-quality interface. Therefore, a high charge transfer efficiency and synergistic effect between the two components can be expected [243], resulting in an augmented photocatalytic CO_2 reduction performance. In this regard, Cai et al. successfully employed OV to anchor single atomic Pt sites on the defective TiO_2 surface, where the synergy of OV and the anchored Pt contributed to enhanced CO_2 reduction performance [244]. Experimental and theoretical studies suggested that the strong electronic interaction between TiO_2 and the OV-anchored Pt atoms can impede the aggregation of Pt. At the same time, Pt modification favored the generation of more surface and subsurface OVs in the TiO_2 substrate.

In addition to metal deposition, Li et al. recently developed an OV-assisted strategy to construct FeOOH/CdS heterostructure as an efficient photocatalyst for CO_2 reduction [245]. It was found that the CdS nanocrystals with a size of ~ 9.3 nm were preferentially deposited at the OV sites on FeOOH nanospindles, forming a hierarchical type-II heterostructure. Due to the synergistic effect of the excellent interfacial charge transfer and the OV-assisted surface reaction, the optimized OV-rich FeOOH/CdS hybrid demonstrated a remarkable CO production rate of $12.55 \mu\text{mol g}^{-1} \text{h}^{-1}$ under visible light irradiation, about 5.0 times higher than that of OV-rich FeOOH ($2.52 \mu\text{mol g}^{-1} \text{h}^{-1}$). This work highlighted the pivotal role of the OV-assisted synthetic strategy in the formation of high-quality interfaces within the metal oxide-based hybrid nanostructure. However, this OV-assisted synthesis strategy is largely applied to supported metal catalysts. Extending this strategy to the synthesis of more types of metal oxide-based hybrid nanocatalysts will be promising for the discovery of high-performance photocatalysts.

5. Conclusions and future perspectives

OV represents a versatile tool for improving the performance of metal oxide-based photocatalysts for CO_2 reduction. In this review, we have summarized the role of OV in metal oxide-based photocatalytic CO_2 reduction (Table 2), together with its controllable synthesis and advanced characterization. Generally, the controllable OV synthesis can be approached from two perspectives, applying a reductive environmental condition and tuning the reducibility of the metal oxide (i.e., OV formation energy). The introduced OV can significantly affect the photocatalytic CO_2 reduction performance of metal oxides by extending the light-absorption range, enhancing the separation of photogenerated charge carriers, and promoting the surface CO_2 conversion reaction. Moreover, the detailed working mechanism of OV in affecting these steps is highly dependent on its states, such as concentration, location, and the component of substrate metal oxides. Based on this understanding, one can rationally design OV to achieve specific functions for metal oxide-based photocatalysts. Particularly, the three basic steps in photocatalytic CO_2 reduction can be simultaneously optimized by OV engineering, with the aim of obtaining high-performance metal oxide-based photocatalysts for CO_2 reduction.

Although remarkable progress has been made in utilizing OV-containing metal oxide photocatalysts for CO_2 reduction, there are still many considerable challenges that have yet to be addressed. Firstly, the performance of the current OV-containing metal oxide photocatalysts is far from satisfactory for its practical application. Under ambient conditions (room temperature and 1 atm pressure), the current CO_2 conversion is commonly at the $\mu\text{mol g}^{-1}$ level, which should at least be

Table 2Summary of the roles of OV in promoting metal oxide-based photocatalytic CO₂ reduction.

^a Role of OV			Catalyst	Product yields ($\mu\text{mol g}^{-1} \text{h}^{-1}$)	^e Performance enhancement	Reaction conditions	Ref.
Light absorption ^b (B, P)	Charge separation ^c (M, H)	Surface reaction ^d (A, D)					
B	–	–	WO ₃ layer	CO, 2.8	CO, 1.8 ×	H ₂ O vapor, 40 W IR lamp (> 800 nm)	[137]
B	–	–	Bi ₂ WO ₆	CH ₄ , 4.3	CH ₄ , 3.0 ×	H ₂ O vapor, 300 W Xe lamp (> 400 nm)	[75]
P	–	–	WO _{3-x}	CH ₄ , 45.7	CH ₄ , 45.7 ×	H ₂ O vapor, 300 W Xe lamp (AM 1.5 G filter)	[79]
P	–	–	Bi ₂ WO ₆	CH ₄ , 9.95	CH ₄ , 26.9 ×	H ₂ O vapor, 300 W Xe lamp	[154]
P	–	–	MoS ₂	CO, 32.4	CO, 12.9 ×	H ₂ O vapor, 300 W Xe lamp	[157]
			/MoO _{3-x}	CH ₄ , 2.0			
P	–	–	WO ₃ /black phosphorus	CO, 26.1	CO, 17.0 ×	H ₂ O vapor, ^g 86 °C, Xe lamp (> 400 nm)	[160]
B	M	–	TiO ₂	CH ₄ , 235.24 ppm g ⁻¹ h ⁻¹	CH ₄ , 22.8 ×	0.1 M KHCO ₃ , 250 W Hg lamp	[164]
–	M	–	Bi ₃ NbTiO ₉ nanosheets	CO, 20.9	CO, 2.0 ×	NaHCO ₃ , 4 M H ₂ SO ₄ , Xe lamp (AM 1.5 G)	[168]
B	M	A	Sr ₂ Bi ₂ Nb ₂ TiO ₁₂ sheets	CO, 17.11	CO, 5.5 ×	NaHCO ₃ , 4 M H ₂ SO ₄ , 20 °C, Xe lamp	[142]
	H	–	Bi ₂ Mo ₂ O _{6-x} /In ₂ S ₃	CO, 28.54	CO, 2.5 ×	H ₂ O, 300 W Xe lamp (> 420 nm)	[180]
–	H	–	Bi ₂ WO _{6-x} /BiOI	CH ₄ , 2.3	CH ₄ , 1.5 ×	H ₂ O, 500 W Xe lamp (> 400 nm)	[183]
–	H	–	rGO/BiO	CO, 4.5	–	H ₂ O, 4 °C, 300 W Xe lamp	[190]
				CH ₄ , 21.75			
–	–	A	Co ₃ O ₄	CO, 18.0 $\mu\text{mol h}^{-1}$	CO, 29.5 ×	[Ru(bpy) ₃]Cl ₂ , H ₂ O, CH ₃ CN, ^h TEOA, Xe lamp (≥ 420 nm)	[211]
–	–	A	r-NiO	CO, 3.14 $\mu\text{mol h}^{-1}$	CO, 1.6 ×	[Ru(bpy) ₃]Cl ₂ , H ₂ O, 10% CO ₂ , CH ₃ CN, TEOA, 5 W LED (400–1000 nm)	[89]
–	–	A	Bi ₂ O ₃ nanosheet	^f DMC, 18% conversion	9.0 ×	CH ₃ OH, 100 °C, 0.2 Mpa, 300 W Xe lamp	[207]
–	–	D	Black Nb ₂ O ₅	CO, 10.6 CH ₄ , 19.5	SCH ₄ , 0–64.8%	H ₂ O, 300 W Xe lamp (> 420 nm)	[213]
–	–	D	Zn-doped CoO	CO, 9.7 CH ₄ , 17.1	CO, 1.8 × CH ₄ , 10 ×	H ₂ O, 80 Pa CO ₂ , Xe lamp (AM 1.5 G filter)	[221]
–	–	D	Cu-doped CeO _{2-x}	CO, 1.65	CO, 26.0 ×	H ₂ O vapor, 300 W Xe lamp	[215]
–	–	D	Au/TiO _{2-x}	CH ₄ , 2.66 C ₂ H ₆ , 0.66	–	H ₂ O vapor, 50 W LED (530 nm)	[227]
–	H	D	Pt/Ga ₂ O _{3-x}	CO, 105.0 CH ₄ , 4.8	CO, 5.4 ×	H ₂ O, 300 W Xe lamp	[235]
–	–	D	Au/TiO _{2-x}	CO, 3.4 CH ₄ , 5.0	CO, 2.7 × CH ₄ , 1.5 ×	H ₂ O, ^g 181 °C, 300 W Xe lamp	[237]
–	–	D	Zn ₂ GeO ₄ nanobelt	Acetate, 12.7 CO, 13.5 HCOOH, 11.7	Acetate, 9.1 ×	H ₂ O, 0.03% CO ₂ in Ar, 75 °C, 300 W Xe lamp (AM 1.5 G filter)	[239]

^a OV can influence all three basic steps in photocatalytic CO₂ reduction. Herein, only the most significant influences are listed for a better comparison.^b B: band structure, P: plasmonic effect.^c M: mono-component metal oxide, H: hybrid nanostructure.^d A: CO₂ adsorption and activation, D: OV-based active site design.^e Performance enhancement brought about by OV.^f DMC: dimethyl carbonate.^g The high reaction temperature is attributed to the photothermal effect of the catalyst.^h TEOA: triethanolamine.

improved by 3 orders of magnitude to fit the continuous process in industrial manufacturing. The limited catalytic activities also reduce the possibility of carrying out the photocatalytic CO₂ reduction in low concentrations of CO₂ (i.e., atmospheric air). Moreover, the current products from photocatalytic CO₂ reduction are mainly C₁ compounds (i.e., CO, CH₄, CH₃OH), which are less valuable than multi-carbon compounds (C₂₊, e.g., C₂H₆, C₂H₄, C₂H₅OH, CH₃CHO, and CH₃COOH). Therefore, rational active site design on OV-containing metal oxides for enhanced CO₂ adsorption and efficient C–C coupling is highly demanded. In addition, coupling photocatalytic CO₂ reduction with thermal and/or electric can be a potential choice for further performance optimization.

Secondly, the true performance of the photocatalyst needs to be carefully evaluated. During photocatalytic CO₂ reduction, any carbon-containing compounds (e.g., organic solvent, organic residue on the catalyst surface, sacrificial agent, and carbon-based catalyst) in the reaction system have the possibility to be decomposed into small

fragments (e.g., CO, CH₄, and C₂H₄), and contribute to false-positive results. Therefore, systematic experiments should be carried out to identify the carbon source of the detected products, including i) control experiments in N₂ or Ar, ii) dark experiments at a similar temperature to photo-reaction, and iii) isotope experiments using ¹³CO₂ as the precursor. In addition, when pure water is employed as the reductant, oxidation products (i.e., O₂ and H₂O₂) should be examined to judge if the CO₂ conversion is realized by a catalytic reaction or a surface chemical reaction (i.e., OV is consumed and cannot be regenerated during the reaction). In detail, product balance should be reached for CO₂ reduction and H₂O oxidation (e.g., CO₂ + H₂O → CO + 1/2 O₂ + H₂O). Only with all the above experiments being carefully implemented, it can be safe to conclude that the detected products are indeed from the photocatalytic reduction of CO₂.

Thirdly, the development of advanced CO₂ reduction systems to make efficient utilization of both photogenerated electrons and holes is pressing for achieving high overall solar-to-fuel conversion efficiency.

Specifically, the holes-related oxidative half-reaction should be well engineered given the slow kinetics of water oxidation. Currently, sacrificial agents (e.g., triethanolamine, methanol, and isopropanol) are commonly employed to accelerate the extraction of holes. However, this will lead to high capital costs and thus limit the practical application of photocatalytic CO₂ reduction. As a promising alternative, the combination of CO₂ reduction with selective organic oxidation can give rise to CO₂ reduction products and value-added chemicals simultaneously, achieving the double-win of catalytic performance and economic efficiency. In addition, the coupling of photocatalytic CO₂ reduction with plastic oxidation (i.e., reduction of the CO₂ obtained from plastic oxidation) has recently emerged as a feasible pathway for plastic upcycling. The knowledge obtained in these systems will also in turn contribute to the advancement of photocatalytic CO₂ reduction with H₂O.

Fourthly, the current methods for OV engineering are mainly focused on tuning the concentration and location (e.g., surface and bulk) of OV in mono-component metal oxide photocatalysts. The controllable formation of OV in more complicated systems (e.g., metal oxide-based hybrid nanostructures) remains a challenge, resulting in substantially limited mechanistic understanding and photocatalytic performance for CO₂ reduction. In such a system, OV can be located at the material surface, bulk, and interface. Moreover, additional active sites can exist in the system to work together with OV for CO₂ adsorption, activation, and conversion. In this context, developing controllable synthetic methods to maximize the synergistic effect between various OVs in the material and the additional active sites on the material surface is promising for obtaining high-performance photocatalysts. The precise integration of OV is also essential for obtaining more profound insights into the structure-performance relationship of photocatalytic CO₂ reduction over OV-containing metal oxide-based hybrid nanocatalysts.

Fifthly, advanced characterization techniques for studying the dynamic changes of OV during photocatalytic CO₂ reduction are still inadequate. For the typical in situ characterization techniques (e.g., EPR, XPS, STM, DRIFTS) in photocatalytic CO₂ reduction, there is a huge disparity between the characterization and the real reaction conditions. For instance, the current in situ EPR characterization is mainly carried out in the gas-solid phase to investigate the influence of light irradiation on the electronic structure of OV. Likewise, in situ XPS can only be carried out at near-ambient pressure (typically <0.5 mbar). In addition, the water content during in situ DRIFTS measurements needs to be well controlled since IR light is highly sensitive to water. These limitations significantly interfere with our understanding of the actual role of OV in photocatalytic reactions. Thus, the development of novel reaction systems that mimic the current in situ characterization conditions is highly desired. The combination of multiple characterization techniques is also recommended for gaining a comprehensive understanding of the role of OV in photocatalytic CO₂ reduction.

Nonetheless, these challenges provide plenty of opportunities for future work in this blooming research field. At the current pace of development and rise in the understanding of the role of OV, it is anticipated that the rational design and controllable synthesis of OV-containing metal oxide will contribute to the next generation of photocatalysts for efficient CO₂ reduction. Meanwhile, it is believed that more latent functions of OV will start to emerge with continuous exploration. We hope this review can inspire more creative work in the field of OV engineering for efficient photocatalytic CO₂ reduction.

Declaration of Competing Interest

The authors declare that they have no known competing financial interests or personal relationships that could have appeared to influence the work reported in this paper.

Data availability

Data will be made available on request.

Acknowledgments

This work was financially supported in part by the Science and Engineering Research Council (SERC) Central Research Fund (Use-Inspired Basic Research) of the Agency for Science, Technology and Research (A*STAR), Singapore, and Natural Science Foundation of China (21725102, 91961106).

References

- [1] J. Ran, M. Jaroniec, S.Z. Qiao, Cocatalysts in semiconductor-based photocatalytic CO₂ reduction: Achievements, challenges, and opportunities, *Adv. Mater.* 30 (2018), <https://doi.org/10.1002/adma.201704649>.
- [2] T. Kong, Y. Jiang, Y. Xiong, Photocatalytic CO₂ conversion: What can we learn from conventional CO_x hydrogenation? *Chem. Soc. Rev.* 49 (2020) 6579–6591, <https://doi.org/10.1039/c9cs00920e>.
- [3] M. Cai, Z. Wu, Z. Li, L. Wang, W. Sun, A.A. Tountas, C. Li, S. Wang, K. Feng, A.-B. Xu, S. Tang, A. Tavasoli, M. Peng, W. Liu, A.S. Helmy, L. He, G.A. Ozin, X. Zhang, Greenhouse-inspired supra-photothermal CO₂ catalysis, *Nat. Energy* 6 (2021) 807–814, <https://doi.org/10.1038/s41560-021-00867-w>.
- [4] J. Low, J. Ma, J. Wan, W. Jiang, Y. Xiong, Identification and design of active sites on photocatalysts for the direct artificial carbon cycle, *Acc. Mater. Res.* 3 (2021) 331–342, <https://doi.org/10.1021/accountsmr.1c00222>.
- [5] Y. Jiang, R. Long, Y. Xiong, Regulating C-C coupling in thermocatalytic and electrocatalytic CO_x conversion based on surface science, *Chem. Sci.* 10 (2019) 7310–7326, <https://doi.org/10.1039/c9sc02014d>.
- [6] J. Fu, K. Jiang, X. Qiu, J. Yu, M. Liu, Product selectivity of photocatalytic CO₂ reduction reactions, *Mater. Today* 32 (2020) 222–243, <https://doi.org/10.1016/j.mattod.2019.06.009>.
- [7] Y. Zhang, B. Xia, J. Ran, K. Davey, S.Z. Qiao, Atomic-level reactive sites for semiconductor-based photocatalytic CO₂ reduction, *Adv. Energy Mater.* 10 (2020) 1903879, <https://doi.org/10.1002/aenm.201903879>.
- [8] S. Cheng, Z. Sun, K.H. Lim, T.Z.H. Gani, T. Zhang, Y. Wang, H. Yin, K. Liu, H. Guo, T. Du, L. Liu, G.K. Li, Z. Yin, S. Kawi, Emerging strategies for CO₂ photoreduction to CH₄: From experimental to data-driven design, *Adv. Energy Mater.* (2022) 2200389, <https://doi.org/10.1002/aenm.202200389>.
- [9] J.Y.Y. Loh, N.P. Kherani, G.A. Ozin, Persistent CO₂ photocatalysis for solar fuels in the dark, *Nat. Sustain* 4 (2021) 466–473, <https://doi.org/10.1038/s41893-021-00681-y>.
- [10] A. Wagner, C.D. Sahm, E. Reisner, Towards molecular understanding of local chemical environment effects in electro- and photocatalytic CO₂ reduction, *Nat. Catal.* 3 (2020) 775–786, <https://doi.org/10.1038/s41929-020-00512-x>.
- [11] C. Gao, Y. Xiong, Solar-driven artificial carbon cycle, *Chin. J. Chem.* 40 (2021) 153–159, <https://doi.org/10.1002/cjoc.202100549>.
- [12] T. Rasheed, S. Shafi, M.T. Anwar, K. Rizwan, T. Ahmad, M. Bilal, Revisiting photo and electro-catalytic modalities for sustainable conversion of CO₂, *Appl. Catal. A Gen.* 623 (2021), 118248, <https://doi.org/10.1016/j.apcata.2021.118248>.
- [13] D. Xi, J. Li, J. Low, K. Mao, R. Long, J. Li, Z. Dai, T. Shao, Y. Zhong, Y. Li, Z. Li, X. J. Loh, L. Song, E. Ye, Y. Xiong, Limiting the uncoordinated N species in M-N_x single-atom catalysts toward electrocatalytic CO₂ reduction in broad voltage range, *Adv. Mater.* 33 (2021), e2104090, <https://doi.org/10.1002/adma.202104090>.
- [14] Y. Jiang, X. Wang, D. Duan, C. He, J. Ma, W. Zhang, H. Liu, R. Long, Z. Li, T. Kong, X.J. Loh, L. Song, E. Ye, Y. Xiong, Structural reconstruction of Cu₂O superparticles toward electrocatalytic CO₂ reduction with high C₂₊ products selectivity, *Adv. Sci.* 9 (2022), e2105292, <https://doi.org/10.1002/advs.202105292>.
- [15] A. Fujishima, K. Honda, Electrochemical photolysis of water at a semiconductor electrode, *Nature* 238 (1972) 37–38, <https://doi.org/10.1038/238037a0>.
- [16] J. Low, R. Long, Y. Xiong, Solar-driven conversion of greenhouse gases toward closing the artificial carbon-cycle loop, *Chem. Catal.* 2 (2022) 226–228, <https://doi.org/10.1016/j.cheecat.2022.01.008>.
- [17] J. Albero, Y. Peng, H. Garcia, Photocatalytic CO₂ reduction to C₂₊ products, *ACS Catal.* 10 (2020) 5734–5749, <https://doi.org/10.1021/acscatal.0c00478>.
- [18] J. Wang, Y. Shi, Y. Wang, Z. Li, Rational design of metal halide perovskite nanocrystals for photocatalytic CO₂ reduction: Recent advances, challenges, and prospects, *ACS Energy Lett.* 7 (2022) 2043–2059, <https://doi.org/10.1021/acsenenergylett.2c00752>.
- [19] M.R. Hoffmann, S.T. Martin, W.Y. Choi, D.W. Bahnemann, Environmental applications of semiconductor photocatalysis, *Chem. Rev.* 95 (1995) 69–96, <https://doi.org/10.1021/cr00033a004>.
- [20] A.A. Ismail, D.W. Bahnemann, Photochemical splitting of water for hydrogen production by photocatalysis: A review, *Sol. Energy Mater. Sol. Cells* 128 (2014) 85–101, <https://doi.org/10.1016/j.solmat.2014.04.037>.
- [21] S. Navarro-Jaén, M. Virginie, J. Bonin, M. Robert, R. Wojcieszak, A.Y. Khodakov, Highlights and challenges in the selective reduction of carbon dioxide to methanol, *Nat. Rev. Chem.* 5 (2021) 564–579, <https://doi.org/10.1038/s41570-021-00289-y>.

- [22] J. Jiang, D. Duan, J. Ma, Y. Jiang, R. Long, C. Gao, Y. Xiong, Van der Waals heterostructures by single cobalt sites-anchored graphene and g-C₃N₄ nanosheets for photocatalytic syngas production with tunable CO/H₂ ratio, *Appl. Catal. B Environ.* 295 (2021), 120261, <https://doi.org/10.1016/j.apcatb.2021.120261>.
- [23] Y. Bo, C. Gao, Y. Xiong, Recent advances in engineering active sites for photocatalytic CO₂ reduction, *Nanoscale* 12 (2020) 12196–12209, <https://doi.org/10.1039/d0nr02596h>.
- [24] S.N. Habisreutinger, L. Schmidt-Mende, J.K. Stolarczyk, Photocatalytic reduction of CO₂ on TiO₂ and other semiconductors, *Angew. Chem. Int. Ed.* 52 (2013) 7372–7408, <https://doi.org/10.1002/anie.201207199>.
- [25] A. Sinhamahapatra, J.P. Jeon, J. Kang, B. Han, J.S. Yu, Oxygen-deficient zirconia (ZrO_{2-x}): A new material for solar light absorption, *Sci. Rep.* 6 (2016) 27218, <https://doi.org/10.1038/srep27218>.
- [26] H. Huang, H. Song, J. Kou, C. Lu, J. Ye, Atomic-level insights into surface engineering of semiconductors for photocatalytic CO₂ reduction, *J. Energy Chem.* 67 (2022) 309–341, <https://doi.org/10.1016/j.jechem.2021.10.015>.
- [27] N. Zhang, C. Gao, Y. Xiong, Defect engineering: A versatile tool for tuning the activation of key molecules in photocatalytic reactions, *J. Energy Chem.* 37 (2019) 43–57, <https://doi.org/10.1016/j.jechem.2018.09.010>.
- [28] Q. Liu, S. Wang, W. Mo, Y. Zheng, Y. Xu, G. Yang, S. Zhong, J. Ma, D. Liu, S. Bai, Emerging stacked photocatalyst design enables spatially separated Ni(OH)₂ redox cocatalysts for overall CO₂ reduction and H₂O oxidation, *Small* 18 (2022), e2104681, <https://doi.org/10.1002/sml.202104681>.
- [29] A.B. Djurišić, Y.H. Leung, A.M. Ching Ng, Strategies for improving the efficiency of semiconductor metal oxide photocatalysis, *Mater. Horiz.* 1 (2014) 400, <https://doi.org/10.1039/c4mh00031e>.
- [30] N. Shehzad, M. Tahir, K. Johari, T. Murugesan, M. Hussain, A critical review on TiO₂ based photocatalytic CO₂ reduction system: Strategies to improve efficiency, *J. CO₂ Util.* 26 (2018) 98–122, <https://doi.org/10.1016/j.jcou.2018.04.026>.
- [31] H. Xiong, Y. Dong, D. Liu, R. Long, T. Kong, Y. Xiong, Recent advances in porous materials for photocatalytic CO₂ Reduct., *J. Phys. Chem. Lett.* 13 (2022) 1272–1282, <https://doi.org/10.1021/acs.jpclett.1c03204>.
- [32] S. Akrami, Y. Murakami, M. Watanabe, T. Ishihara, M. Arita, M. Fuji, K. Edalati, Defective high-entropy oxide photocatalyst with high activity for CO₂ conversion, *Appl. Catal. B Environ.* 303 (2022), 120896, <https://doi.org/10.1016/j.apcatb.2021.120896>.
- [33] L. Hao, H. Huang, Y. Zhang, T. Ma, Oxygen vacant semiconductor photocatalysts, *Adv. Funct. Mater.* 31 (2021) 2100919, <https://doi.org/10.1002/adfm.202100919>.
- [34] X. Pan, M.Q. Yang, X. Fu, N. Zhang, Y.J. Xu, Defective TiO₂ with oxygen vacancies: synthesis, properties and photocatalytic applications, *Nanoscale* 5 (2013) 3601–3614, <https://doi.org/10.1039/c3nr00476g>.
- [35] P. Li, Z. Zhou, Q. Wang, M. Guo, S. Chen, J. Low, R. Long, W. Liu, P. Ding, Y. Wu, Y. Xiong, Visible-Light-Driven Nitrogen Fixation Catalyzed by Bi₂O₃/Br Nanostructures: Enhanced Performance by Oxygen Vacancies, *J. Am. Chem. Soc.* 142 (2020) 12430–12439, <https://doi.org/10.1021/jacs.0c05097>.
- [36] H.L. Tuller, S.R. Bishop, Point defects in oxides: Tailoring materials through defect engineering, *Annu. Rev. Mater. Res.* 41 (2011) 369–398, <https://doi.org/10.1146/annurev-matsci-062910-100442>.
- [37] H. Zhao, F. Pan, Y. Li, A review on the effects of TiO₂ surface point defects on CO₂ photoreduction with H₂O, *J. Mater.* 3 (2017) 17–32, <https://doi.org/10.1016/j.jmat.2016.12.001>.
- [38] S. Bai, N. Zhang, C. Gao, Y. Xiong, Defect engineering in photocatalytic materials, *Nano Energy* 53 (2018) 296–336, <https://doi.org/10.1016/j.nanoen.2018.08.058>.
- [39] G. Pacchioni, Oxygen vacancy: the invisible agent on oxide surfaces, *ChemPhysChem* 4 (2003) 1041–1047, <https://doi.org/10.1002/cphc.200300835>.
- [40] Y. Li, W. Zhang, J. Niu, Y. Chen, Mechanism of photogenerated reactive oxygen species and correlation with the antibacterial properties of engineered metal-oxide nanoparticles, *ACS Nano* 6 (2012) 5164–5173, <https://doi.org/10.1021/nn300934k>.
- [41] F. Gunkel, D.V. Christensen, Y.Z. Chen, N. Pryds, Oxygen vacancies: The (in) visible friend of oxide electronics, *Appl. Phys. Lett.* 116 (2020), 120505, <https://doi.org/10.1063/1.5143309>.
- [42] G. Zhuang, Y. Chen, Z. Zhuang, Y. Yu, J. Yu, Oxygen vacancies in metal oxides: Recent progress towards advanced catalyst design, *Sci. China Mater.* 63 (2020) 2089–2118, <https://doi.org/10.1007/s40843-020-1305-6>.
- [43] Y. Huang, Y. Yu, Y. Yu, B. Zhang, Oxygen vacancy engineering in photocatalysis, *Sol. RRL* 4 (2020) 2000037, <https://doi.org/10.1002/solr.202000037>.
- [44] R. Qian, H. Zong, J. Schneider, G. Zhou, T. Zhao, Y. Li, J. Yang, D.W. Bahnemann, J.H. Pan, Charge carrier trapping, recombination and transfer during TiO₂ photocatalysis: An overview, *Catal. Today* 335 (2019) 78–90, <https://doi.org/10.1016/j.cattod.2018.10.053>.
- [45] W. Tu, Y. Zhou, Z. Zou, Photocatalytic conversion of CO₂ into renewable hydrocarbon fuels: state-of-the-art accomplishment, challenges, and prospects, *Adv. Mater.* 26 (2014) 4607–4626, <https://doi.org/10.1002/adma.201400087>.
- [46] W. Jiang, J. Low, C. Qiu, R. Long, Y. Xiong, Photocatalytic methane conversion over metal oxides: Fundamentals, achievements, and challenges, *J. Univ. Sci. Technol. China* 50 (2020) 1361, <https://doi.org/10.3969/j.issn.0253-2778.2020.11.001>.
- [47] N.H. Khadry, A.S. Alayyar, L.M. Alsarhan, S. Alshihri, M. Mokhtar, Metal oxides as catalyst/supporter for CO₂ capture and conversion, review, *Catalysts* 12 (2022) 300, <https://doi.org/10.3390/catal12030300>.
- [48] X. Chen, L. Liu, F. Huang, Black titanium dioxide (TiO₂) nanomaterials, *Chem. Soc. Rev.* 44 (2015) 1861–1885, <https://doi.org/10.1039/c4cs00330f>.
- [49] G. Wang, Y. Yang, D. Han, Y. Li, Oxygen defective metal oxides for energy conversion and storage, *Nano Today* 13 (2017) 23–39, <https://doi.org/10.1016/j.nantod.2017.02.009>.
- [50] Z. Wang, R. Lin, Y. Huo, H. Li, L. Wang, Formation, detection, and function of oxygen vacancy in metal oxides for solar energy conversion, *Adv. Funct. Mater.* 32 (2021) 2109503, <https://doi.org/10.1002/adfm.202109503>.
- [51] H. Liu, H.T. Ma, X.Z. Li, W.Z. Li, M. Wu, X.H. Bao, The enhancement of TiO₂ photocatalytic activity by hydrogen thermal treatment, *Chemosphere* 50 (2003) 39–46, [https://doi.org/10.1016/s0045-6535\(02\)00486-1](https://doi.org/10.1016/s0045-6535(02)00486-1).
- [52] Y. Ding, I.S. Yang, Z. Li, X. Xia, W.I. Lee, S. Dai, D.W. Bahnemann, J.H. Pan, Nanoporous TiO₂ spheres with tailored textural properties: Controllable synthesis, formation mechanism, and photochemical applications, *Prog. Mater. Sci.* 109 (2020), 100620, <https://doi.org/10.1016/j.pmatsci.2019.100620>.
- [53] Z. Wang, X. Mao, P. Chen, M. Xiao, S.A. Monny, S. Wang, M. Konarova, A. Du, L. Wang, Understanding the roles of oxygen vacancies in hematite-based photoelectrochemical processes, *Angew. Chem. Int. Ed.* 58 (2019) 1030–1034, <https://doi.org/10.1002/anie.201810583>.
- [54] S. Yang, Y. Liu, Y. Hao, X. Yang, W.A. Goddard III, X.L. Zhang, B. Cao, Oxygen-vacancy abundant ultrathin Co₃O₄/graphene composites for high-rate supercapacitor electrodes, *Adv. Sci.* 5 (2018) 1700659, <https://doi.org/10.1002/advs.201700659>.
- [55] S. Selim, E. Pastor, M. Garcia-Tecedor, M.R. Morris, L. Francas, M. Sachs, B. Moss, S. Corby, C.A. Mesa, S. Gimenez, A. Kafizas, A.A. Bakulin, J.R. Durrant, Impact of oxygen vacancy occupancy on charge carrier dynamics in BiVO₄ photoanodes, *J. Am. Chem. Soc.* 141 (2019) 18791–18798, <https://doi.org/10.1021/jacs.9b09056>.
- [56] S. Sakthivel, M.V. Shankar, M. Palanichamy, B. Arabindoo, D.W. Bahnemann, V. Murugesan, Enhancement of photocatalytic activity by metal deposition: characterisation and photonic efficiency of Pt, Au and Pd deposited on TiO₂ catalyst, *Water Res.* 38 (2004) 3001–3008, <https://doi.org/10.1016/j.watres.2004.04.046>.
- [57] E. Ye, S.Y. Zhang, S.H. Lim, S. Liu, M.Y. Han, Morphological tuning, self-assembly and optical properties of indium oxide nanocrystals, *Phys. Chem. Chem. Phys.* 12 (2010) 11923–11929, <https://doi.org/10.1039/c0cp00138d>.
- [58] Y. Qi, L. Song, S. Ouyang, X. Liang, S. Ning, Q. Zhang, J. Ye, Photoinduced defect engineering: Enhanced photothermal catalytic performance of 2D black In₂O_{3-x} nanosheets with bifunctional oxygen vacancies, *Adv. Mater.* 32 (2020), e1903915, <https://doi.org/10.1002/adma.201903915>.
- [59] H. Liu, F. Zhang, H. Wang, J. Xue, Y. Guo, Q. Qian, G. Zhang, Oxygen vacancy engineered unsaturated coordination in cobalt carbonate hydroxide nanowires enables highly selective photocatalytic CO₂ reduction, *Energy Environ. Sci.* 14 (2021) 5339–5346, <https://doi.org/10.1039/d1ee01397a>.
- [60] W. Zhang, C. Fu, J. Low, D. Duan, J. Ma, W. Jiang, Y. Chen, H. Liu, Z. Qi, R. Long, Y. Yao, X. Li, H. Zhang, Z. Liu, J. Yang, Z. Zou, Y. Xiong, High-performance photocatalytic nonoxidative conversion of methane to ethane and hydrogen by heteroatoms-engineered TiO₂, *Nat. Commun.* 13 (2022) 2806, <https://doi.org/10.1038/s41467-022-30532-z>.
- [61] Z. Deng, J. Ji, M. Xing, J. Zhang, The role of oxygen defects in metal oxides for CO₂ reduction, *Nanoscale Adv.* 2 (2020) 4986–4995, <https://doi.org/10.1039/d0na00535e>.
- [62] C.M. Yim, C.L. Pang, G. Thornton, Oxygen vacancy origin of the surface band-gap state of TiO₂(110), *Phys. Rev. Lett.* 104 (2010), 036806, <https://doi.org/10.1103/PhysRevLett.104.036806>.
- [63] N. Zhang, X. Li, H. Ye, S. Chen, H. Ju, D. Liu, Y. Lin, W. Ye, C. Wang, Q. Xu, J. Zhu, L. Song, J. Jiang, Y. Xiong, Oxide defect engineering enables to couple solar energy into oxygen activation, *J. Am. Chem. Soc.* 138 (2016) 8928–8935, <https://doi.org/10.1021/jacs.6b04629>.
- [64] Z. Wang, C. Yang, T. Lin, H. Yin, P. Chen, D. Wan, F. Xu, F. Huang, J. Lin, X. Xie, M. Jiang, H-doped black titania with very high solar absorption and excellent photocatalysis enhanced by localized surface plasmon resonance, *Adv. Funct. Mater.* 23 (2013) 5444–5450, <https://doi.org/10.1002/adfm.201300486>.
- [65] N. Zhang, A. Jalil, D. Wu, S. Chen, Y. Liu, C. Gao, W. Ye, Z. Qi, H. Ju, C. Wang, X. Wu, L. Song, J. Zhu, Y. Xiong, Refining defect states in W₁₈O₄₉ by Mo doping: A strategy for tuning N₂ activation towards solar-driven nitrogen fixation, *J. Am. Chem. Soc.* 140 (2018) 9434–9443, <https://doi.org/10.1021/jacs.8b02076>.
- [66] M. Duan, C. Hu, H. Li, Y. Chen, R. Chen, W. Gong, Z. Lu, N. Zhang, R. Long, L. Song, Y. Xiong, Synergizing inter and intraband transitions in defective tungsten oxide for efficient photocatalytic alcohol dehydration to alkenes, *JACS Au* 2 (2022) 1160–1168, <https://doi.org/10.1021/jacsau.2c00146>.
- [67] A. Agrawal, S.H. Cho, O. Zandi, S. Ghosh, R.W. Johns, D.J. Milliron, Localized surface plasmon resonance in semiconductor nanocrystals, *Chem. Rev.* 118 (2018) 3121–3207, <https://doi.org/10.1021/acs.chemrev.7b00613>.
- [68] U. Aslam, V.G. Rao, S. Chavez, S. Linic, Catalytic conversion of solar to chemical energy on plasmonic metal nanostructures, *Nat. Catal.* 1 (2018) 656–665, <https://doi.org/10.1038/s41929-018-0138-x>.
- [69] E. Ye, M.D. Regulacio, S.Y. Zhang, X.J. Loh, M.Y. Han, Anisotropically branched metal nanostructures, *Chem. Soc. Rev.* 44 (2015) 6001–6017, <https://doi.org/10.1039/c5cs00213c>.
- [70] D. Liu, C. Xue, Plasmonic coupling architectures for enhanced photocatalysis, *Adv. Mater.* 33 (2021), e2005738, <https://doi.org/10.1002/adma.202005738>.
- [71] J. Li, Z. Lou, B. Li, Engineering plasmonic semiconductors for enhanced photocatalysis, *J. Mater. Chem. A* 9 (2021) 18818–18835, <https://doi.org/10.1039/d1ta04541e>.
- [72] V. Etacheri, C. Di Valentin, J. Schneider, D. Bahnemann, S.C. Pillai, Visible-light activation of TiO₂ photocatalysts: Advances in theory and experiments,

- J. Photochem. Photobiol. C. 25 (2015) 1–29, <https://doi.org/10.1016/j.jphotochemrev.2015.08.003>.
- [73] A. Naldoni, M. Altomare, G. Zoppellaro, N. Liu, S. Kment, R. Zboril, P. Schmuki, Photocatalysis with reduced TiO₂: From black TiO₂ to cocatalyst-free hydrogen production, *ACS Catal.* 9 (2019) 345–364, <https://doi.org/10.1021/acscatal.8b04068>.
- [74] Q.D. Truong, T.H. Le, J.-Y. Liu, C.-C. Chung, Y.-C. Ling, Synthesis of TiO₂ nanoparticles using novel titanium oxalate complex towards visible light-driven photocatalytic reduction of CO₂ to CH₃OH, *Appl. Catal. A Gen.* 437–438 (2012) 28–35, <https://doi.org/10.1016/j.apcata.2012.06.009>.
- [75] X.Y. Kong, Y.Y. Choo, S.P. Chai, A.K. Soh, A.R. Mohamed, Oxygen vacancy induced Bi₂WO₆ for the realization of photocatalytic CO₂ reduction over the full solar spectrum: from the UV to the NIR region, *Chem. Commun.* 52 (2016) 14242–14245, <https://doi.org/10.1039/c6cc07750a>.
- [76] K. Zhang, L. Wang, J.K. Kim, M. Ma, G. Veerappan, C.-L. Lee, H. K.-j. Kong, J. H. Lee, Park, An order/disorder/water junction system for highly efficient co-catalyst-free photocatalytic hydrogen generation, *Energy Environ. Sci.* 9 (2016) 499–503, <https://doi.org/10.1039/c5ee03100a>.
- [77] G. Yin, X. Huang, T. Chen, W. Zhao, Q. Bi, J. Xu, Y. Han, F. Huang, Hydrogenated blue titania for efficient solar to chemical conversions: Preparation, characterization, and reaction mechanism of CO₂ reduction, *ACS Catal.* 8 (2018) 1009–1017, <https://doi.org/10.1021/acscatal.7b03473>.
- [78] X. Liu, L. Yang, M. Huang, Q. Li, L. Zhao, Y. Sang, X. Zhang, Z. Zhao, H. Liu, W. Zhou, Oxygen vacancy-regulated metallic semiconductor MoO₂ nanobelt photoelectron and hot electron self-coupling for photocatalytic CO₂ reduction in pure water, *Appl. Catal. B Environ.* 319 (2022), 121887, <https://doi.org/10.1016/j.apcatb.2022.121887>.
- [79] D. Liu, C. Wang, Y. Yu, B.-H. Zhao, W. Wang, Y. Du, B. Zhang, Understanding the nature of ammonia treatment to synthesize oxygen vacancy-enriched transition metal oxides, *Chem* 5 (2019) 376–389, <https://doi.org/10.1016/j.chempr.2018.11.001>.
- [80] J. Gao, Q. Shen, R. Guan, J. Xue, X. Liu, H. Jia, Q. Li, Y. Wu, Oxygen vacancy self-doped black TiO₂ nanotube arrays by aluminothermic reduction for photocatalytic CO₂ reduction under visible light illumination, *J. CO₂ Util.* 35 (2020) 205–215, <https://doi.org/10.1016/j.jcou.2019.09.016>.
- [81] A. Sinhamahapatra, J.-P. Jeon, J.-S. Yu, A new approach to prepare highly active and stable black titania for visible light-assisted hydrogen production, *Energy Environ. Sci.* 8 (2015) 3539–3544, <https://doi.org/10.1039/c5ee02443a>.
- [82] X. Chen, L. Liu, P.Y. Yu, S.S. Mao, Increasing solar absorption for photocatalysis with black hydrogenated titanium dioxide nanocrystals, *Science* 331 (2011) 746–750, <https://doi.org/10.1126/science.1200448>.
- [83] J. Wang, D.N. Tafen, J.P. Lewis, Z. Hong, A. Manivannan, M. Zhi, M. Li, N. Wu, Origin of photocatalytic activity of nitrogen-doped TiO₂ nanobelts, *J. Am. Chem. Soc.* 131 (2009) 12290–12297, <https://doi.org/10.1021/ja903781h>.
- [84] T.W. Kim, Y. Ping, G.A. Galli, K.S. Choi, Simultaneous enhancements in photon absorption and charge transport of bismuth vanadate photoanodes for solar water splitting, *Nat. Commun.* 6 (2015) 8769, <https://doi.org/10.1038/ncomms9769>.
- [85] H. Liang, Z. Cao, C. Xia, F. Ming, W. Zhang, A.-H. Emwas, L. Cavallo, H. N. Alshareef, Tungsten blue oxide as a reusable electrocatalyst for acidic water oxidation by plasma-induced vacancy engineering, *CCS Chem.* 3 (2021) 1553–1561, <https://doi.org/10.31635/ccschem.020.202000325>.
- [86] X. Zhu, J. Yang, X. Zhu, J. Yuan, M. Zhou, X. She, Q. Yu, Y. Song, Y. She, Y. Hua, H. Li, H. Xu, Exploring deep effects of atomic vacancies on activating CO₂ photoreduction via rationally designing indium oxide photocatalysts, *Chem. Eng. J.* 422 (2021), 129888, <https://doi.org/10.1016/j.cej.2021.129888>.
- [87] G. Chen, V. Georgieva, T. Godfroid, R. Snyder, M.-P. Delplanck-Ogletree, Plasma assisted catalytic decomposition of CO₂, *Appl. Catal. B Environ.* 190 (2016) 115–124, <https://doi.org/10.1016/j.apcatb.2016.03.009>.
- [88] M. Shen, M. Wang, Q. Wang, J. Tian, L. Zhang, L. Wang, J. Shi, A Ti-OH bond breaking route for creating oxygen vacancy in titania towards efficient CO₂ photoreduction, *Chem. Eng. J.* 425 (2021), 131513, <https://doi.org/10.1016/j.cej.2021.131513>.
- [89] W. Chen, X. Liu, B. Han, S. Liang, H. Deng, Z. Lin, Boosted photoreduction of diluted CO₂ through oxygen vacancy engineering in NiO nanoplatelets, *Nano Res* 14 (2020) 730–737, <https://doi.org/10.1007/s12274-020-3105-1>.
- [90] J. Di, P. Song, C. Zhu, C. Chen, J. Xiong, M. Duan, R. Long, W. Zhou, M. Xu, L. Kang, B. Lin, D. Liu, S. Chen, C. Liu, H. Li, Y. Zhao, S. Li, Q. Yan, L. Song, Z. Liu, Strain-engineering of Bi₁₂O₁₇Br₂ nanotubes for boosting photocatalytic CO₂ reduction, *ACS Mater. Lett.* 2 (2020) 1025–1032, <https://doi.org/10.1021/acsmaterialslett.0c00306>.
- [91] S. Akrami, M. Watanabe, T.H. Ling, T. Ishihara, M. Arita, M. Fuji, K. Edalati, High-pressure TiO₂-II polymorph as an active photocatalyst for CO₂ to CO conversion, *Appl. Catal. B Environ.* 298 (2021), 120566, <https://doi.org/10.1016/j.apcatb.2021.120566>.
- [92] S. Akrami, Y. Murakami, M. Watanabe, T. Ishihara, M. Arita, Q. Guo, M. Fuji, K. Edalati, Enhanced CO₂ conversion on highly-strained and oxygen-deficient BiVO₄ photocatalyst, *Chem. Eng. J.* 442 (2022), 136209, <https://doi.org/10.1016/j.cej.2022.136209>.
- [93] Y. Xu, M. Liu, F. Tong, F. Ma, X. He, Z. Wang, P. Wang, Y. Liu, H. Cheng, Y. Dai, Z. Zheng, B. Huang, Strain-assisted in-situ formed oxygen defective WO₃ film for photothermal-synergistic reverse water gas shift reaction and single-particle study, *Chem. Eng. J.* 433 (2022), 134199, <https://doi.org/10.1016/j.cej.2021.134199>.
- [94] S. Sun, M. Watanabe, J. Wu, Q. An, T. Ishihara, Ultrathin WO₃·0.33H₂O nanotubes for CO₂ photoreduction to acetate with high selectivity, *J. Am. Chem. Soc.* 140 (2018) 6474–6482, <https://doi.org/10.1021/jacs.8b03316>.
- [95] E. Scorza, U. Birkenheuer, C. Pisani, The oxygen vacancy at the surface and in bulk MgO: An embedded-cluster study, *J. Chem. Phys.* 107 (1997) 9645–9658, <https://doi.org/10.1063/1.475260>.
- [96] M. Nolan, J. Fearon, G. Watson, Oxygen vacancy formation and migration in ceria, *Solid State Ion.* 177 (2006) 3069–3074, <https://doi.org/10.1016/j.ssi.2006.07.045>.
- [97] S. Guo, J. Di, C. Chen, C. Zhu, M. Duan, C. Lian, M. Ji, W. Zhou, M. Xu, P. Song, R. Long, X. Cao, K. Gu, J. Xia, H. Liu, Y. Zhao, L. Song, Y. Xiong, S. Li, Z. Liu, Oxygen vacancy mediated bismuth stannate ultra-small nanoparticle towards photocatalytic CO₂-to-CO conversion, *Appl. Catal. B Environ.* 276 (2020), 119156, <https://doi.org/10.1016/j.apcatb.2020.119156>.
- [98] J. Di, X. Zhao, C. Lian, M. Ji, J. Xia, J. Xiong, W. Zhou, X. Cao, Y. She, H. Liu, K. P. Loh, S.J. Pennycook, H. Li, Z. Liu, Atomically-thin Bi₂MoO₆ nanosheets with vacancy pairs for improved photocatalytic CO₂ reduction, *Nano Energy* 61 (2019) 54–59, <https://doi.org/10.1016/j.nanoen.2019.04.029>.
- [99] F. Lei, Y. Sun, K. Liu, S. Gao, L. Liang, B. Pan, Y. Xie, Oxygen vacancies confined in ultrathin indium oxide porous sheets for promoted visible-light water splitting, *J. Am. Chem. Soc.* 136 (2014) 6826–6829, <https://doi.org/10.1021/ja501866r>.
- [100] K. Yu, L.L. Lou, S. Liu, W. Zhou, Asymmetric oxygen vacancies: The intrinsic redox active sites in metal oxide catalysts, *Adv. Sci.* 7 (2020) 1901970, <https://doi.org/10.1002/advs.201901970>.
- [101] M. Wang, M. Shen, X. Jin, J. Tian, Y. Shao, L. Zhang, Y. Li, J. Shi, Exploring the enhancement effects of hetero-metal doping in CeO₂ on CO₂ photocatalytic reduction performance, *Chem. Eng. J.* 427 (2022), 130987, <https://doi.org/10.1016/j.cej.2021.130987>.
- [102] A.T. Brant, S. Yang, N.C. Giles, M.Z. Iqbal, A. Manivannan, L.E. Halliburton, Oxygen vacancies adjacent to Cu²⁺ ions in TiO₂ (rutile) crystals, *J. Appl. Phys.* 109 (2011), 073711, <https://doi.org/10.1063/1.3552910>.
- [103] V. Kumaravel, S. Rhatigan, S. Mathew, J. Bartlett, M. Nolan, S.J. Hinder, P. K. Sharma, A. Singh, J.A. Byrne, J. Harrison, S.C. Pillai, Indium-doped TiO₂ photocatalysts with high-temperature anatase stability, *J. Phys. Chem. C* 123 (2019) 21083–21096, <https://doi.org/10.1021/acs.jpcc.9b06811>.
- [104] B.-H. Lee, E. Gong, M. Kim, S. Park, H.R. Kim, J. Lee, E. Jung, C.W. Lee, J. Bok, Y. Jung, Y.S. Kim, K.-S. Lee, S.-P. Cho, J.-W. Jung, C.-H. Cho, S. Lebegue, K. T. Nam, H. Kim, S.-I. In, T. Hyeon, Electronic interaction between transition metal single-atoms and anatase TiO₂ boosts CO₂ photoreduction with H₂O, *Energy Environ. Sci.* 15 (2022) 601–609, <https://doi.org/10.1039/d1ee01574e>.
- [105] Y. Bo, H. Wang, Y. Lin, T. Yang, R. Ye, Y. Li, C. Hu, P. Du, Y. Hu, Z. Liu, R. Long, C. Gao, B. Ye, L. Song, X. Wu, Y. Xiong, Altering hydrogenation pathways in photocatalytic nitrogen fixation by tuning local electronic structure of oxygen vacancy with dopant, *Angew. Chem. Int. Ed.* 60 (2021) 16085–16092, <https://doi.org/10.1002/anie.202104001>.
- [106] M. Xiao, L. Zhang, B. Luo, M. Lyu, Z. Wang, H. Huang, S. Wang, A. Du, L. Wang, Molten-salt-mediated synthesis of an atomic nickel co-catalyst on TiO₂ for improved photocatalytic H₂, *Evol., Angew. Chem. Int. Ed.* 59 (2020) 7230–7234, <https://doi.org/10.1002/anie.202001148>.
- [107] B. Lei, W. Cui, P. Chen, L. Chen, J. Li, F. Dong, C-doping induced oxygen-vacancy in WO₃ nanosheets for CO₂ activation and photoreduction, *ACS Catal.* 12 (2022) 9670–9678, <https://doi.org/10.1021/acscatal.2c02390>.
- [108] Y. Huang, K. Li, J. Zhou, J. Guan, F. Zhu, K. Wang, M. Liu, W. Chen, N. Li, Nitrogen-stabilized oxygen vacancies in TiO₂ for site-selective loading of Pt and CoO_x cocatalysts toward enhanced photoreduction of CO₂ to CH₄, *Chem. Eng. J.* 439 (2022), 135744, <https://doi.org/10.1016/j.cej.2022.135744>.
- [109] M. Zheng, J. Yang, W. Fan, X. Zhao, Oxygen vacancy and nitrogen doping collaboratively boost performance and stability of TiO₂-supported Pd catalysts for CO₂ photoreduction: a DFT study, *Phys. Chem. Chem. Phys.* 23 (2021) 24801–24813, <https://doi.org/10.1039/d1cp03693a>.
- [110] A.R. Puigdollers, P. Schlexer, S. Tosoni, G. Pacchioni, Increasing oxide reducibility: The role of metal/oxide interfaces in the formation of oxygen vacancies, *ACS Catal.* 7 (2017) 6493–6513, <https://doi.org/10.1021/acscatal.7b01913>.
- [111] W. Jiang, J. Low, K. Mao, D. Duan, S. Chen, W. Liu, C.-W. Pao, J. Ma, S. Sang, C. Shu, X. Zhan, Z. Qi, H. Zhang, Z. Liu, X. Wu, R. Long, L. Song, Y. Xiong, Pd-modified ZnO-Au enabling alkoxy intermediates formation and dehydrogenation for photocatalytic conversion of methane to ethylene, *J. Am. Chem. Soc.* 143 (2021) 269–278, <https://doi.org/10.1021/jacs.0c10369>.
- [112] T.-D. Pham, B.-K. Lee, Novel capture and photocatalytic conversion of CO₂ into solar fuels by metals co-doped TiO₂ deposited on PU under visible light, *Appl. Catal. A Gen.* 529 (2017) 40–48, <https://doi.org/10.1016/j.apcata.2016.10.019>.
- [113] Z. Duan, X. Zhao, C. Wei, L. Chen, Ag-Bi/BiVO₄ chain-like hollow microstructures with enhanced photocatalytic activity for CO₂ conversion, *Appl. Catal. A Gen.* 594 (2020), 117459, <https://doi.org/10.1016/j.apcata.2020.117459>.
- [114] J. Zhao, Y. Li, Y. Zhu, Y. Wang, C. Wang, Enhanced CO₂ photoreduction activity of black TiO₂-coated Cu nanoparticles under visible light irradiation: Role of metallic Cu, *Appl. Catal. A Gen.* 510 (2016) 34–41, <https://doi.org/10.1016/j.apcata.2015.11.001>.
- [115] C. Shen, K. Sun, Z. Zhang, N. Rui, X. Jia, D. Mei, C.-j. Liu, Highly active Ir/In₂O₃ catalysts for selective hydrogenation of CO₂ to methanol: Experimental and theoretical studies, *ACS Catal.* 11 (2021) 4036–4046, <https://doi.org/10.1021/acscatal.0c05628>.
- [116] J. Jia, P.G. O'Brien, L. He, Q. Qiao, T. Fei, L.M. Reyes, T.E. Burrow, Y. Dong, K. Liao, M. Varela, S.J. Pennycook, M. Hmadeh, A.S. Helmy, N.P. Kherani, D. Perovic, G.A. Ozin, Visible and near-infrared photothermal catalyzed hydrogenation of gaseous CO₂ over nanostructured Pd/Nb₂O₅, *Adv. Sci.* 3 (2016) 1600189, <https://doi.org/10.1002/advs.201600189>.

- [117] L. Zhang, J. Ran, S.Z. Qiao, M. Jaroniec, Characterization of semiconductor photocatalysts, *Chem. Soc. Rev.* 48 (2019) 5184–5206, <https://doi.org/10.1039/c9cs00172g>.
- [118] K. Ye, K. Li, Y. Lu, Z. Guo, N. Ni, H. Liu, Y. Huang, H. Ji, P. Wang, An overview of advanced methods for the characterization of oxygen vacancies in materials, *TrAC, Trends Anal. Chem.* 116 (2019) 102–108, <https://doi.org/10.1016/j.trac.2019.05.002>.
- [119] O. Al-Madanat, B.N. Nunes, Y. AlSalka, A. Hakki, M. Curti, A.O.T. Patrocinio, D. W. Bahnemann, Application of EPR spectroscopy in TiO_2 and Nb_2O_5 photocatalysis, *Catalysts* 11 (2021) 1514, <https://doi.org/10.3390/catal1121514>.
- [120] Z. Wang, L. Wang, Role of oxygen vacancy in metal oxide based photoelectrochemical water splitting, *EcoMat* 3 (2021), <https://doi.org/10.1002/eom2.12075>.
- [121] T. Berger, M. Sterrer, O. Diwald, E. Knozinger, D. Panayotov, T.L. Thompson, J. T. Yates, Light-induced charge separation in anatase TiO_2 particles, *J. Phys. Chem. B* 109 (2005) 6061–6068, <https://doi.org/10.1021/jp0404293>.
- [122] L. Luo, L. Fu, H. Liu, Y. Xu, J. Xing, C.R. Chang, D.Y. Yang, J. Tang, Synergy of Pd atoms and oxygen vacancies on In_2O_3 for methane conversion under visible light, *Nat. Commun.* 13 (2022) 2930, <https://doi.org/10.1038/s41467-022-30434-0>.
- [123] L. Liu, C. Zhao, J.T. Miller, Y. Li, Mechanistic study of CO_2 photoreduction with H_2O on Cu/ TiO_2 nanocomposites by in situ X-ray absorption and infrared spectroscopies, *J. Phys. Chem. C* 121 (2016) 490–499, <https://doi.org/10.1021/acs.jpcc.6b10835>.
- [124] Z. Xiao, Y.C. Huang, C.L. Dong, C. Xie, Z. Liu, S. Du, W. Chen, D. Yan, L. Tao, Z. Shu, G. Zhang, H. Duan, Y. Wang, Y. Zou, R. Chen, S. Wang, Operando identification of the dynamic behavior of oxygen vacancy-rich Co_3O_4 for oxygen evolution reaction, *J. Am. Chem. Soc.* 142 (2020) 12087–12095, <https://doi.org/10.1021/jacs.0c00257>.
- [125] R. Le Toquin, W. Paulus, A. Cousson, C. Prestipino, C. Lamberti, Time-resolved in situ studies of oxygen intercalation into $\text{SrCoO}_{2.5}$, performed by neutron diffraction and X-ray absorption spectroscopy, *J. Am. Chem. Soc.* 128 (2006) 13161–13174, <https://doi.org/10.1021/ja063207m>.
- [126] H.R. Park, A.U. Pawar, U. Pal, T. Zhang, Y.S. Kang, Enhanced solar photoreduction of CO_2 to liquid fuel over rGO grafted NiO-CeO_2 heterostructure nanocomposite, *Nano Energy* 79 (2021), 105483, <https://doi.org/10.1016/j.nanoen.2020.105483>.
- [127] M. Karppinen, M. Matvejeff, K. Salomäki, H. Yamauchi, Oxygen content analysis of functional perovskite-derived cobalt oxides, *J. Mater. Chem* 12 (2002) 1761–1764, <https://doi.org/10.1039/b200770n>.
- [128] S. Gao, B. Gu, X. Jiao, Y. Sun, X. Zu, F. Yang, W. Zhu, C. Wang, Z. Feng, B. Ye, Y. Xie, Highly efficient and exceptionally durable CO_2 photoreduction to methanol over freestanding defective single-unit-cell bismuth vanadate layers, *J. Am. Chem. Soc.* 139 (2017) 3438–3445, <https://doi.org/10.1021/jacs.6b11263>.
- [129] X. Liu, K. Zhou, L. Wang, B. Wang, Y. Li, Oxygen vacancy clusters promoting reducibility and activity of ceria nanorods, *J. Am. Chem. Soc.* 131 (2009) 3140–3141, <https://doi.org/10.1021/ja808433d>.
- [130] X. Jiang, Y. Zhang, J. Jiang, Y. Rong, Y. Wang, Y. Wu, C. Pan, Characterization of oxygen vacancy associates within hydrogenated TiO_2 : A positron annihilation study, *J. Phys. Chem. C* 116 (2012) 22619–22624, <https://doi.org/10.1021/jp307573c>.
- [131] X. Zhang, F. Tang, M. Wang, W. Zhan, H. Hu, Y. Li, R.H. Friend, X. Song, Femtosecond visualization of oxygen vacancies in metal oxides, *Sci. Adv.* 6 (2020), <https://doi.org/10.1126/sciadv.aax9427>.
- [132] L. Luo, M. Su, P. Yan, L. Zou, D.K. Schreiber, D.R. Baer, Z. Zhu, G. Zhou, Y. Wang, S.M. Bruemmer, Z. Xu, C. Wang, Atomic origins of water-vapour-promoted alloy oxidation, *Nat. Mater.* 17 (2018) 514–518, <https://doi.org/10.1038/s41563-018-0078-5>.
- [133] D.A. Muller, N. Nakagawa, A. Ohtomo, J.L. Grazul, H.Y. Hwang, Atomic-scale imaging of nanoengineered oxygen vacancy profiles in SrTiO_3 , *Nature* 430 (2004) 657–661, <https://doi.org/10.1038/nature02756>.
- [134] D.P. Acharya, N. Camillone, P. Sutter, CO_2 adsorption, diffusion, and electron-induced chemistry on rutile $\text{TiO}_2(110)$: A low-temperature scanning tunneling microscopy study, *J. Phys. Chem. C* 115 (2011) 12095–12105, <https://doi.org/10.1021/jp202476v>.
- [135] R. Schaub, E. Wahlstrom, A. Ronnau, E. Laegsgaard, I. Stensgaard, F. Besenbacher, Oxygen-mediated diffusion of oxygen vacancies on the $\text{TiO}_2(110)$ surface, *Science* 299 (2003) 377–379, <https://doi.org/10.1126/science.1078962>.
- [136] M. Setvin, U. Aschauer, P. Scheiber, Y.-F. Li, W. Hou, M. Schmid, A. Selloni, U. Diebold, Reaction of O_2 with subsurface oxygen vacancies on TiO_2 anatase (101), *Science* 341 (2013) 988–991, <https://doi.org/10.1126/science.1239879>.
- [137] L. Liang, X. Li, Y. Sun, Y. Tan, X. Jiao, H. Ju, Z. Qi, J. Zhu, Y. Xie, Infrared light-driven CO_2 overall splitting at room temperature, *Joule* 2 (2018) 1004–1016, <https://doi.org/10.1016/j.joule.2018.02.019>.
- [138] X. Zu, Y. Zhao, X. Li, R. Chen, W. Shao, Z. Wang, J. Hu, J. Zhu, Y. Pan, Y. Sun, Y. Xie, Ultrafast and efficient visible-light-driven CO_2 reduction triggered by regenerative oxygen-vacancies in $\text{Bi}_2\text{O}_3\text{CO}_3$ nanosheets, *Angew. Chem. Int. Ed.* 60 (2021) 13840–13846, <https://doi.org/10.1002/anie.202101894>.
- [139] H.-B. Fan, S.-Y. Yang, P.-F. Zhang, H.-Y. Wei, X.-L. Liu, C.-M. Jiao, Q.-S. Zhu, Y.-H. Chen, Z.-G. Wang, Investigation of oxygen vacancy and interstitial oxygen defects in ZnO films by photoluminescence and X-ray photoelectron spectroscopy, *Chinese Phys. Lett.* 24 (2007) 2108–2111.
- [140] P. Klason, T. Moe Børseth, Q.X. Zhao, B.G. Svensson, A.Y. Kuznetsov, P. J. Bergman, M. Willander, Temperature dependence and decay times of zinc and oxygen vacancy related photoluminescence bands in zinc oxide, *Solid State Commun.* 145 (2008) 321–326, <https://doi.org/10.1016/j.ssc.2007.10.036>.
- [141] R. Gurwitz, R. Cohen, I. Shalish, Interaction of light with the ZnO surface: Photon induced oxygen “breathing,” oxygen vacancies, persistent photoconductivity, and persistent photovoltage, *J. Appl. Phys.* 115 (2014), 033701, <https://doi.org/10.1063/1.4861413>.
- [142] H. Yu, J. Li, Y. Zhang, S. Yang, K. Han, F. Dong, T. Ma, H. Huang, Three-in-one oxygen vacancies: Whole visible-spectrum absorption, efficient charge separation, and surface site activation for robust CO_2 photoreduction, *Angew. Chem. Int. Ed.* 58 (2019) 3880–3884, <https://doi.org/10.1002/anie.201813967>.
- [143] A. Naldoni, M. Allieta, S. Santangelo, M. Marelli, F. Fabbri, S. Cappelli, C. L. Bianchi, R. Psaro, V. Dal Santo, Effect of nature and location of defects on bandgap narrowing in black TiO_2 nanoparticles, *J. Am. Chem. Soc.* 134 (2012) 7600–7603, <https://doi.org/10.1021/ja3012676>.
- [144] Y. Yang, L.C. Yin, Y. Gong, P. Niu, J.Q. Wang, L. Gu, X. Chen, G. Liu, L. Wang, H. M. Cheng, An unusual strong visible-light absorption band in red anatase TiO_2 photocatalyst induced by atomic hydrogen-occupied oxygen vacancies, *Adv. Mater.* 30 (2018) 1704479, <https://doi.org/10.1002/adma.201704479>.
- [145] O. Ola, M.M. Maroto-Valer, Transition metal oxide based TiO_2 nanoparticles for visible light induced CO_2 photoreduction, *Appl. Catal. A Gen.* 502 (2015) 114–121, <https://doi.org/10.1016/j.apcata.2015.06.007>.
- [146] Z. Shen, Q. Xia, Y. Li, C. Yin, Z. Ge, X. Li, Y. Wang, Adsorption-enhanced nitrogen-doped mesoporous CeO_2 as an efficient visible-light-driven catalyst for CO_2 photoreduction, *J. CO₂ Util.* 39 (2020), 101176, <https://doi.org/10.1016/j.jcou.2020.101176>.
- [147] W. Zhang, J. Xue, Q. Shen, S. Jia, J. Gao, X. Liu, H. Jia, Black single-crystal TiO_2 nanosheet array films with oxygen vacancy on {001} facets for boosting photocatalytic CO_2 reduction, *J. Alloy. Compd.* 870 (2021), 159400, <https://doi.org/10.1016/j.jallcom.2021.159400>.
- [148] A. Ziarati, A. Badiei, R. Luque, M. Dadras, T. Burgi, Visible light CO_2 reduction to CH_4 using hierarchical yolk@shell $\text{TiO}_2\text{-xH}_2$ modified with plasmonic Au-Pd nanoparticles, *ACS Sustain. Chem. Eng.* 8 (2020) 3689–3696, <https://doi.org/10.1021/acssuschemeng.9b06751>.
- [149] J. Ye, J. Xu, D. Tian, X. Zhao, Q. Wang, J. Wang, Y. Li, C. Zhao, Z. Liu, Y. Fu, Efficient photocatalytic reduction of CO_2 by a rhenium-doped $\text{TiO}_2\text{-x}/\text{SnO}_2$ inverse opal S-scheme heterostructure assisted by the slow-phonon effect, *Sep. Purif. Technol.* 277 (2021), 119431, <https://doi.org/10.1016/j.seppur.2021.119431>.
- [150] X. Jiang, Y. Ding, S. Zheng, Y. Ye, Z. Li, L. Xu, J. Wang, Z. Li, X.J. Loh, E. Ye, L. Sun, In-situ generated CsPbBr_3 nanocrystals on O-Defective WO_3 for photocatalytic CO_2 reduction, *ChemSusChem* 15 (2022), e202102295, <https://doi.org/10.1002/cssc.202102295>.
- [151] M.T. Greiner, L. Chai, M.G. Helander, W.-M. Tang, Z.-H. Lu, Transition metal oxide work functions: The influence of cation oxidation state and oxygen vacancies, *Adv. Funct. Mater.* 22 (2012) 4557–4568, <https://doi.org/10.1002/adfm.201200615>.
- [152] M. Zhang, G. Cheng, Y. Wei, Z. Wen, R. Chen, J. Xiong, W. Li, C. Han, Z. Li, Cuprous ion (Cu^+) doping induced surface/interface engineering for enhancing the CO_2 photoreduction capability of $\text{W}_{18}\text{O}_{49}$ nanowires, *J. Colloid Interface Sci.* 572 (2020) 306–317, <https://doi.org/10.1016/j.jcis.2020.03.090>.
- [153] Y. Li, M. Wen, Y. Wang, G. Tian, C. Wang, J. Zhao, Plasmonic hot electrons from oxygen vacancies for infrared light-driven catalytic CO_2 reduction on $\text{Bi}_2\text{O}_3\text{-x}$, *Angew. Chem. Int. Ed.* 60 (2021) 910–916, <https://doi.org/10.1002/anie.202010156>.
- [154] C. Lu, X. Li, Q. Wu, J. Li, L. Wen, Y. Dai, B. Huang, B. Li, Z. Lou, Constructing surface plasmon resonance on Bi_2WO_6 to boost high-selective CO_2 reduction for methane, *ACS Nano* 15 (2021) 3529–3539, <https://doi.org/10.1021/acsnano.1c00452>.
- [155] Z. Lou, M. Zhu, X. Yang, Y. Zhang, M.-H. Whangbo, B. Li, B. Huang, Continual injection of photoinduced electrons stabilizing surface plasmon resonance of non-elemental-metal plasmonic photocatalyst $\text{CdS}/\text{WO}_{3-x}$ for efficient hydrogen generation, *Appl. Catal. B Environ.* 226 (2018) 10–15, <https://doi.org/10.1016/j.apcatb.2017.12.023>.
- [156] Z. Zhang, J. Huang, Y. Fang, M. Zhang, K. Liu, B. Dong, A nonmetal plasmonic Z-scheme photocatalyst with UV- to NIR-driven photocatalytic protons reduction, *Adv. Mater.* 29 (2017), <https://doi.org/10.1002/adma.201606688>.
- [157] J. Li, X. Xu, B. Huang, Z. Lou, B. Li, Light-induced in situ formation of a nonmetallic plasmonic $\text{MoS}_2/\text{MoO}_{3-x}$ heterostructure with efficient charge transfer for CO_2 reduction and SERS detection, *ACS Appl. Mater. Interfaces* 13 (2021) 10047–10053, <https://doi.org/10.1021/acsaami.0c21401>.
- [158] Z. Lou, P. Zhang, J. Li, X. Yang, B. Huang, B. Li, Plasmonic heterostructure $\text{TiO}_2\text{-x}/\text{WO}_{3-x}$ NWs with continuous photoelectron injection boosting hot electron for methane generation, *Adv. Funct. Mater.* 29 (2019) 1808696, <https://doi.org/10.1002/adfm.201808696>.
- [159] Y. Liu, X. Dong, Q. Yuan, J. Liang, Y. Zhou, X. Qu, B. Dong, In-situ synthesis of $\text{WO}_{3-x}/\text{MoO}_{3-x}$ heterojunction with abundant oxygen vacancies for efficient photocatalytic reduction of CO_2 , *Colloid Surf. A* 621 (2021), 126582, <https://doi.org/10.1016/j.colsurfa.2021.126582>.
- [160] C. Lu, X. Li, J. Li, L. Mao, M. Zhu, Q. Chen, L. Wen, B. Li, T. Guo, Z. Lou, Nonmetallic surface plasmon resonance coupling with pyroelectric effect for enhanced near-infrared-driven CO_2 reduction, *Chem. Eng. J.* 445 (2022), 136739, <https://doi.org/10.1016/j.cej.2022.136739>.
- [161] D.A. Wheeler, Y. Ling, R.J. Dillon, R.C. Fitzmorris, C.G. Dudzik, L. Zavodivker, T. Rajh, N.M. Dimitrijevic, G. Millhauser, C. Bardeen, Y. Li, J.Z. Zhang, Probing the nature of bandgap states in hydrogen-treated TiO_2 nanowires, *J. Phys. Chem. C* 117 (2013) 26821–26830, <https://doi.org/10.1021/jp409857j>.

- [162] T. Zhang, J. Low, J. Yu, A.M. Tyryshkin, E. Mikmekova, T. Asefa, A blinking mesoporous TiO_{2-x} composed of nanosized anatase with unusually long-lived trapped charge carriers, *Angew. Chem. Int. Ed.* 59 (2020) 15000–15007, <https://doi.org/10.1002/anie.202005143>.
- [163] M. Kong, Y. Li, X. Chen, T. Tian, P. Fang, F. Zheng, X. Zhao, Tuning the relative concentration ratio of bulk defects to surface defects in TiO_2 nanocrystals leads to high photocatalytic efficiency, *J. Am. Chem. Soc.* 133 (2011) 16414–16417, <https://doi.org/10.1021/ja207826q>.
- [164] J. Li, M. Zhang, Z. Guan, Q. Li, C. He, J. Yang, Synergistic effect of surface and bulk single-electron-trapped oxygen vacancy of TiO_2 in the photocatalytic reduction of CO_2 , *Appl. Catal. B Environ.* 206 (2017) 300–307, <https://doi.org/10.1016/j.apcatb.2017.01.025>.
- [165] J. Di, C. Chen, C. Zhu, R. Long, H. Chen, X. Cao, J. Xiong, Y. Weng, L. Song, S. Li, H. Li, Y. Xiong, Z. Liu, Surface local polarization induced by bismuth-oxygen vacancy pairs tuning non-covalent interaction for CO_2 photoreduction, *Adv. Energy Mater.* 11 (2021) 2102389, <https://doi.org/10.1002/aenm.202102389>.
- [166] S.-T. Xiao, S.-M. Wu, Y. Dong, J.-W. Liu, L.-Y. Wang, L. Wu, Y.-X. Zhang, G. Tian, C. Janiak, M. Shalom, Y.-T. Wang, Y.-Z. Li, R.-K. Jia, D.W. Bahnemann, X.-Y. Yang, Rich surface hydroxyl design for nanostructured TiO_2 and its hole-trapping effect, *Chem. Eng. J.* 400 (2020), 125909, <https://doi.org/10.1016/j.cej.2020.125909>.
- [167] L.B. Hoch, P. Szymanski, K.K. Ghuman, L. He, K. Liao, Q. Qiao, L.M. Reyes, Y. Zhu, M.A. El-Sayed, C.V. Singh, G.A. Ozin, Carrier dynamics and the role of surface defects: Designing a photocatalyst for gas-phase CO_2 reduction, *E8011-E8020, Proc. Natl. Acad. Sci. USA* 113 (2016), <https://doi.org/10.1073/pnas.1609374113>.
- [168] H. Yu, F. Chen, X. Li, H. Huang, Q. Zhang, S. Su, K. Wang, E. Mao, B. Mei, G. Mul, T. Ma, Y. Zhang, Synergy of ferroelectric polarization and oxygen vacancy to promote CO_2 photoreduction, *Nat. Commun.* 12 (2021) 4594, <https://doi.org/10.1038/s41467-021-24882-3>.
- [169] H. Zheng, C. Wang, X. Zhang, Y. Li, H. Ma, Y. Liu, Control over energy level match in Keggin polyoxometallate- TiO_2 microspheres for multielectron photocatalytic reactions, *Appl. Catal. B Environ.* 234 (2018) 79–89, <https://doi.org/10.1016/j.apcatb.2018.04.015>.
- [170] R. Chong, C. Su, Y. Du, Y. Fan, Z. Ling, Z. Chang, D. Li, Insights into the role of MgAl layered double oxides interlayer in Pt/ TiO_2 toward photocatalytic CO_2 reduction, *J. Catal.* 363 (2018) 92–101, <https://doi.org/10.1016/j.jcat.2018.04.020>.
- [171] S. Ali, J. Lee, H. Kim, Y. Hwang, A. Razzaq, J.-W. Jung, C.-H. Cho, S.-I. In, Sustained, photocatalytic CO_2 reduction to CH_4 in a continuous flow reactor by earth-abundant materials: Reduced titania- Cu_2O Z-scheme heterostructures, *Appl. Catal. B Environ.* 279 (2020), 119344, <https://doi.org/10.1016/j.apcatb.2020.119344>.
- [172] J. Liu, J. Wan, L. Liu, W. Yang, J. Low, X. Gao, F. Fu, Synergistic effect of oxygen defect and doping engineering on S-scheme $\text{O-ZnIn}_2\text{S}_4/\text{TiO}_{2-x}$ heterojunction for effective photocatalytic hydrogen production by water reduction coupled with oxidative dehydrogenation, *Chem. Eng. J.* 430 (2022), 133125, <https://doi.org/10.1016/j.cej.2021.133125>.
- [173] T. Wei, Y.-N. Zhu, X. An, L.-M. Liu, X. Cao, H. Liu, J. Qu, Defect modulation of Z-scheme $\text{TiO}_2/\text{Cu}_2\text{O}$ photocatalysts for durable water splitting, *ACS Catal.* 9 (2019) 8346–8354, <https://doi.org/10.1021/acscatal.9b01786>.
- [174] Y. Zhang, L. Shi, H. Yuan, X. Sun, X. Li, L. Duan, Q. Li, Z. Huang, X. Ban, D. Zhang, Construction of melamine foam-supported $\text{WO}_3/\text{CsPbBr}_3$ S-scheme heterojunction with rich oxygen vacancies for efficient and long-period CO_2 photoreduction in liquid-phase H_2O environment, *Chem. Eng. J.* 430 (2022), 132820, <https://doi.org/10.1016/j.cej.2021.132820>.
- [175] T.M. Suzuki, S. Yoshino, K. Sekizawa, Y. Yamaguchi, A. Kudo, T. Morikawa, Photocatalytic CO_2 reduction by a Z-scheme mechanism in an aqueous suspension of particulate $(\text{CuGa})_{0.3}\text{Zn}_{1.4}\text{S}_2$, BiVO_4 and a Co complex operating dual-functionally as an electron mediator and as a cocatalyst, *Appl. Catal. B Environ.* 316 (2022), 121600, <https://doi.org/10.1016/j.apcatb.2022.121600>.
- [176] K. Wang, L. Jiang, X. Wu, G. Zhang, Vacancy mediated Z-scheme charge transfer in a 2D/2D $\text{La}_2\text{Ti}_2\text{O}_7/\text{g-C}_3\text{N}_4$ nanojunction as a bifunctional photocatalyst for solar-to-energy conversion, *J. Mater. Chem. A* 8 (2020) 13241–13247, <https://doi.org/10.1039/d0ta01310b>.
- [177] A. Han, M. Li, S. Zhang, X. Zhu, J. Han, Q. Ge, H. Wang, Ti^{3+} defective $\text{SnS}_2/\text{TiO}_2$ heterojunction photocatalyst for visible-light driven reduction of CO_2 to CO with high selectivity, *Catalysts* 9 (2019) 927, <https://doi.org/10.3390/catal9110927>.
- [178] S. Huang, Y. Long, S. Ruan, Y.-J. Zeng, Enhanced photocatalytic CO_2 reduction in defect-engineered Z-scheme $\text{WO}_{3-x}/\text{g-C}_3\text{N}_4$ heterostructures, *ACS Omega* 4 (2019) 15593–15599, <https://doi.org/10.1021/acsomega.9b01969>.
- [179] X. Yue, L. Cheng, J. Fan, Q. Xiang, 2D/2D $\text{BiVO}_4/\text{CsPbBr}_3$ S-scheme heterojunction for photocatalytic CO_2 reduction: Insights into structure regulation and Fermi level modulation, *Appl. Catal. B Environ.* 304 (2022), 120979, <https://doi.org/10.1016/j.apcatb.2021.120979>.
- [180] B. Yu, Y. Wu, F. Meng, Q. Wang, X. Jia, M. Wasim Khan, C. Huang, S. Zhang, L. Yang, H. Wu, Formation of hierarchical $\text{Bi}_2\text{MoO}_6/\text{In}_2\text{S}_3$ S-scheme heterojunction with rich oxygen vacancies for boosting photocatalytic CO_2 reduction, *Chem. Eng. J.* 429 (2022), 132456, <https://doi.org/10.1016/j.cej.2021.132456>.
- [181] S. Sultana, S. Mansingh, K.M. Parida, Facile synthesis of CeO_2 nanosheets decorated upon BiOI microplate: A surface oxygen vacancy promoted Z-scheme-based 2D–2D nanocomposite photocatalyst with enhanced photocatalytic activity, *J. Phys. Chem. C* 122 (2017) 808–819, <https://doi.org/10.1021/acs.jpcc.7b08534>.
- [182] J. Xiong, M. Zhang, G. Cheng, Facile polyol-triggered anatase-rutile heterophase TiO_{2-x} nanoparticles for enhancing photocatalytic CO_2 reduction, *J. Colloid Interface Sci.* 579 (2020) 872–877, <https://doi.org/10.1016/j.jcis.2020.06.103>.
- [183] X.Y. Kong, W.Q. Lee, A.R. Mohamed, S.-P. Chai, Effective steering of charge flow through synergistic inducing oxygen vacancy defects and p-n heterojunctions in 2D/2D surface-engineered $\text{Bi}_2\text{WO}_6/\text{BiOI}$ cascade: Towards superior photocatalytic CO_2 reduction activity, *Chem. Eng. J.* 372 (2019) 1183–1193, <https://doi.org/10.1016/j.cej.2019.05.001>.
- [184] Y. Cao, Q. Li, C. Li, J. Li, J. Yang, Surface heterojunction between (001) and (101) facets of ultrafine anatase TiO_2 nanocrystals for highly efficient photoreduction CO_2 to CH_4 , *Appl. Catal. B Environ.* 198 (2016) 378–388, <https://doi.org/10.1016/j.apcatb.2016.05.071>.
- [185] D. Zhang, Y.J. Sun, X. Tian, X.T. Liu, X.J. Wang, J. Zhao, Y.P. Li, F.T. Li, Promoting photocatalytic CO_2 reduction to CH_4 via a combined strategy of defects and tunable hydroxyl radicals, *J. Colloid Interface Sci.* 606 (2022) 1477–1487, <https://doi.org/10.1016/j.jcis.2021.08.163>.
- [186] H.M. Hwang, S. Oh, J.H. Shim, Y.M. Kim, A. Kim, D. Kim, J. Kim, S. Bak, Y. Cho, V.Q. Bui, T.A. Le, H. Lee, Phase-selective disordered anatase/ordered rutile interface system for visible-light-driven, metal-free CO_2 reduction, *ACS Appl. Mater. Interfaces* 11 (2019) 35693–35701, <https://doi.org/10.1021/acsami.9b10837>.
- [187] M. Liang, Y. Borjigin, Y. Zhang, B. Liu, H. Liu, H. Guo, Controlled assemble of hollow heterostructured $\text{g-C}_3\text{N}_4/\text{CeO}_2$ with rich oxygen vacancies for enhanced photocatalytic CO_2 reduction, *Appl. Catal. B Environ.* 243 (2019) 566–575, <https://doi.org/10.1016/j.apcatb.2018.11.010>.
- [188] H. Shi, S. Long, S. Hu, J. Hou, W. Ni, C. Song, K. Li, G.G. Gurzadyan, X. Guo, Interfacial charge transfer in 0D/2D defect-rich heterostructures for efficient solar-driven CO_2 reduction, *Appl. Catal. B Environ.* 245 (2019) 760–769, <https://doi.org/10.1016/j.apcatb.2019.01.036>.
- [189] Y.-f. Miao, R.-t. Guo, J.-w. Gu, Y.-z. Liu, G.-l. Wu, C.-p. Duan, W.-g. Pan, Oxygen vacancy-rich BiO_{2-x} : Super-active co-catalyst on $\text{g-C}_3\text{N}_4$ for efficient visible-light photocatalytic CO_2 reduction, *J. CO₂ Util.* 44 (2021), 101377, <https://doi.org/10.1016/j.jcou.2020.101377>.
- [190] S. Sun, M. Watanabe, P. Wang, T. Ishihara, Synergistic enhancement of H_2 and CH_4 evolution by CO_2 photoreduction in water with reduced graphene oxide–bismuth monoxide quantum dot catalyst, *ACS Appl. Energy Mater.* 2 (2019) 2104–2112, <https://doi.org/10.1021/acsaem.8b02153>.
- [191] F. Zhang, W. Ma, H. Guo, Y. Zhao, X. Shan, K. Jin, H. Tian, Q. Zhao, D. Yu, X. Lu, G. Lu, S. Meng, Interfacial oxygen vacancies as a potential cause of hysteresis in perovskite solar cells, *Chem. Mater.* 28 (2016) 802–812, <https://doi.org/10.1021/acs.chemmater.5b04019>.
- [192] U. Tumuluri, J.D. Howe, W.P. Mounfield, M. Li, M. Chi, Z.D. Hood, K.S. Walton, D.S. Sholl, S. Dai, Z. Wu, Effect of surface structure of TiO_2 nanoparticles on CO_2 adsorption and SO_2 resistance, *ACS Sustain. Chem. Eng.* 5 (2017) 9295–9306, <https://doi.org/10.1021/acssuschemeng.7b02295>.
- [193] P. Li, S. Zhu, H. Hu, L. Guo, T. He, Influence of defects in porous ZnO nanoplates on CO_2 photoreduction, *Catal. Today* 335 (2019) 300–305, <https://doi.org/10.1016/j.cattod.2018.11.068>.
- [194] D.C. Soreescu, W.A. Al-Saidi, K.D. Jordan, CO_2 adsorption on $\text{TiO}_2(101)$ anatase: a dispersion-corrected density functional theory study, *J. Chem. Phys.* 135 (2011), 124701, <https://doi.org/10.1063/1.3638181>.
- [195] A. Ziarati, A. Badiei, R. Grillo, T. Burgi, 3D yolk@Shell $\text{TiO}_{2-x}/\text{LDH}$ architecture: Tailored structure for visible light CO_2 conversion, *ACS Appl. Mater. Interfaces* 11 (2019) 5903–5910, <https://doi.org/10.1021/acsaami.8b17232>.
- [196] X. She, X. Zhu, J. Yang, Y. Song, Y. She, D. Liu, J. Wu, Q. Yu, H. Li, Z. Liu, P. M. Ajayan, H. Xu, Grain-boundary surface terminations incorporating oxygen vacancies for selectively boosting CO_2 photoreduction activity, *Nano Energy* 84 (2021), 105869, <https://doi.org/10.1016/j.nanoen.2021.105869>.
- [197] M. Wang, M. Shen, X. Jin, J. Tian, Y. Zhou, Y. Shao, L. Zhang, Y. Li, J. Shi, Mild generation of surface oxygen vacancies on CeO_2 for improved CO_2 photoreduction activity, *Nanoscale* 12 (2020) 12374–12382, <https://doi.org/10.1039/d0nr00717j>.
- [198] R. Schaub, P. Thstrup, N. Lopez, E. Laegsgaard, I. Stensgaard, J.K. Nørskov, F. Besenbacher, Oxygen vacancies as active sites for water dissociation on rutile $\text{TiO}_2(110)$, *Phys. Rev. Lett.* 87 (2001), 266104, <https://doi.org/10.1103/PhysRevLett.87.266104>.
- [199] W. Pipornpong, R. Wanbayor, V. Ruangpornvisuti, Adsorption CO_2 on the perfect and oxygen vacancy defect surfaces of anatase TiO_2 and its photocatalytic mechanism of conversion to CO, *Appl. Surf. Sci.* 257 (2011) 10322–10328, <https://doi.org/10.1016/j.apsusc.2011.06.013>.
- [200] S. Rhatigan, M. Nolan, CO_2 and water activation on ceria nanocluster modified TiO_2 rutile (110), *J. Mater. Chem. A* 6 (2018) 9139–9152, <https://doi.org/10.1039/c8ta01270a>.
- [201] J. Lee, D.C. Soreescu, X. Deng, Electron-induced dissociation of CO_2 on $\text{TiO}_2(110)$, *J. Am. Chem. Soc.* 133 (2011) 10066–10069, <https://doi.org/10.1021/ja204077e>.
- [202] W. Chu, Q. Zheng, O.V. Prezhdo, J. Zhao, CO_2 photoreduction on metal oxide surface is driven by transient capture of hot electrons: Ab initio quantum dynamics simulation, *J. Am. Chem. Soc.* 142 (2020) 3214–3221, <https://doi.org/10.1021/jacs.9b13280>.
- [203] L. Wang, Y. Wang, Y. Cheng, Z. Liu, Q. Guo, M.N. Ha, Z. Zhao, Hydrogen-treated mesoporous WO_3 as a reducing agent of CO_2 to fuels (CH_4 and CH_3OH) with enhanced photothermal catalytic performance, *J. Mater. Chem. A* 4 (2016) 5314–5322, <https://doi.org/10.1039/c5ta10180h>.
- [204] S. Gao, Z. Sun, W. Liu, X. Jiao, X. Zu, Q. Hu, Y. Sun, T. Yao, W. Zhang, S. Wei, Y. Xie, Atomic layer confined vacancies for atomic-level insights into carbon

- dioxide electroreduction, *Nat. Commun.* 8 (2017) 14503, <https://doi.org/10.1038/ncomms14503>.
- [205] B. Wang, X. Wang, L. Lu, C. Zhou, Z. Xin, J. Wang, G. X.-k. Ke, S. Sheng, Z. Yan, Zou, Oxygen-vacancy-activated CO₂ splitting over amorphous oxide semiconductor photocatalyst, *ACS Catal.* 8 (2017) 516–525, <https://doi.org/10.1021/acscatal.7b02952>.
- [206] L. Liu, H. Zhao, J.M. Andino, Y. Li, Photocatalytic CO₂ reduction with H₂O on TiO₂ nanocrystals: Comparison of anatase, rutile, and brookite polymorphs and exploration of surface chemistry, *ACS Catal.* 2 (2012) 1817–1828, <https://doi.org/10.1021/cs300273q>.
- [207] S. Chen, H. Wang, Z. Kang, S. Jin, X. Zhang, X. Zheng, Z. Qi, J. Zhu, B. Pan, Y. Xie, Oxygen vacancy associated single-electron transfer for photofixation of CO₂ to long-chain chemicals, *Nat. Commun.* 10 (2019) 788, <https://doi.org/10.1038/s41467-019-08697-x>.
- [208] J.-Y. Liu, X.-Q. Gong, A.N. Alexandrova, Mechanism of CO₂ photocatalytic reduction to methane and methanol on defected anatase TiO₂ (101): A density functional theory study, *J. Phys. Chem. C* 123 (2019) 3505–3511, <https://doi.org/10.1021/acs.jpcc.8b09539>.
- [209] Y. Ji, Y. Luo, New mechanism for photocatalytic reduction of CO₂ on the anatase TiO₂(101) surface: The essential role of oxygen vacancy, *J. Am. Chem. Soc.* 138 (2016) 15896–15902, <https://doi.org/10.1021/jacs.6b05695>.
- [210] Y. Ji, Y. Luo, Direct donation of protons from H₂O to CO₂ in artificial photosynthesis on the anatase TiO₂(101) surface, *J. Phys. Chem. C* 123 (2019) 3019–3023, <https://doi.org/10.1021/acs.jpcc.8b11936>.
- [211] Q. Zhang, P. Yang, H. Zhang, J. Zhao, H. Shi, Y. Huang, H. Yang, Oxygen vacancies in Co₃O₄ promote CO₂ photoreduction, *Appl. Catal. B Environ.* 300 (2022), 120729, <https://doi.org/10.1016/j.apcatb.2021.120729>.
- [212] H. Zhao, J. Chen, G. Rao, W. Deng, Y. Li, Enhancing photocatalytic CO₂ reduction by coating an ultrathin Al₂O₃ layer on oxygen deficient TiO₂ nanorods through atomic layer deposition, *Appl. Surf. Sci.* 404 (2017) 49–56, <https://doi.org/10.1016/j.apsusc.2017.01.267>.
- [213] X. Lin, S. Xia, L. Zhang, Y. Zhang, S. Sun, Y. Chen, S. Chen, B. Ding, J. Yu, J. Yan, Fabrication of flexible mesoporous black Nb₂O₅ nanofiber films for visible-light-driven photocatalytic CO₂ reduction into CH₄, *Adv. Mater.* 34 (2022), e2200756, <https://doi.org/10.1002/adma.202200756>.
- [214] S. Gong, Y. Niu, X. Liu, C. Xu, D. Xiong, Z. Tu, M. Xu, Z. Chen, Fabrication of hetero-metal oxide NiCo₂V₂O₈ hollow nanospheres for efficient visible light-driven CO₂ photoreduction, *Appl. Catal. B Environ.* 316 (2022), 121663, <https://doi.org/10.1016/j.apcatb.2022.121663>.
- [215] M. Wang, M. Shen, X. Jin, J. Tian, M. Li, Y. Zhou, L. Zhang, Y. Li, J. Shi, Oxygen vacancy generation and stabilization in CeO_{2-x} by Cu introduction with improved CO₂ photocatalytic reduction activity, *ACS Catal.* 9 (2019) 4573–4581, <https://doi.org/10.1021/acscatal.8b03975>.
- [216] H. Lai, X. Zeng, T. Song, S. Yin, B. Long, A. Ali, G.J. Deng, Fast synthesis of porous iron doped CeO₂ with oxygen vacancy for effective CO₂ photoreduction, *J. Colloid Interface Sci.* 608 (2022) 1792–1801, <https://doi.org/10.1016/j.jcis.2021.10.064>.
- [217] L. Li, P. Li, Y. Wang, L. Lin, A.H. Shah, T. He, Modulation of oxygen vacancy in hydrangea-like ceria via Zr doping for CO₂ photoreduction, *Appl. Surf. Sci.* 452 (2018) 498–506, <https://doi.org/10.1016/j.apsusc.2018.04.256>.
- [218] L. Liu, Z. Liu, H. Sun, X. Zhao, Morphological effects of Au₁₃ clusters on the adsorption of CO₂ over anatase TiO₂ (101), *Appl. Surf. Sci.* 399 (2017) 469–479, <https://doi.org/10.1016/j.apsusc.2016.12.089>.
- [219] T.-D. Pham, B.-K. Lee, Novel photocatalytic activity of Cu@V co-doped TiO₂/PU for CO₂ reduction with H₂O vapor to produce solar fuels under visible light, *J. Catal.* 345 (2017) 87–95, <https://doi.org/10.1016/j.jcat.2016.10.030>.
- [220] L. Pan, H. Mei, G. Zhu, S. Li, X. Xie, S. Gong, H. Liu, Z. Jin, J. Gao, L. Cheng, L. Zhang, Bi selectively doped SrTiO_{3-x} nanosheets enhance photocatalytic CO₂ reduction under visible light, *J. Colloid Interface Sci.* 611 (2022) 137–148, <https://doi.org/10.1016/j.jcis.2021.12.033>.
- [221] K. Chen, T. Jiang, T. Liu, J. Yu, S. Zhou, A. Ali, S. Wang, Y. Liu, L. Zhu, X. Xu, Zn dopants synergistic oxygen vacancy boosts ultrathin CoO layer for CO₂ photoreduction, *Adv. Funct. Mater.* 32 (2021) 2109336, <https://doi.org/10.1002/adfm.202109336>.
- [222] L. Liu, F. Gao, H. Zhao, Y. Li, Tailoring Cu valence and oxygen vacancy in Cu/TiO₂ catalysts for enhanced CO₂ photoreduction efficiency, *Appl. Catal. B Environ.* 134–135 (2013) 349–358, <https://doi.org/10.1016/j.apcatb.2013.01.040>.
- [223] S. Ali, A. Razzaq, H. Kim, S.-I. In, Activity, selectivity, and stability of earth-abundant CuO/Cu₂O/Cu⁰-based photocatalysts toward CO₂ reduction, *Chem. Eng. J.* 429 (2022), 131579, <https://doi.org/10.1016/j.cej.2021.131579>.
- [224] M. Liu, X. Bao, F. Ma, M. Wang, L. Zheng, Z. Wang, P. Wang, Y. Liu, H. Cheng, Y. Dai, Y. Fan, Z. Zheng, B. Huang, Enhanced stability and activity towards photocatalytic CO₂ reduction via supercycle ALD of Cu and TiO₂, *Chem. Eng. J.* 429 (2022), 132022, <https://doi.org/10.1016/j.cej.2021.132022>.
- [225] L. Liu, C. Zhao, Y. Li, Spontaneous dissociation of CO₂ to CO on defective surface of Cu(I)/TiO_{2-x} nanoparticles at room temperature, *J. Phys. Chem. C* 116 (2012) 7904–7912, <https://doi.org/10.1021/jp300932b>.
- [226] S. Zhu, S. Liang, Y. Tong, X. An, J. Long, X. Fu, X. Wang, Photocatalytic reduction of CO₂ with H₂O to CH₄ on Cu(I) supported TiO₂ nanosheets with defective {001} facets, *Phys. Chem. Chem. Phys.* 17 (2015) 9761–9770, <https://doi.org/10.1039/c5cp00647c>.
- [227] K. Wang, J. Lu, Y. Lu, C.H. Lau, Y. Zheng, X. Fan, Unravelling the C-C coupling in CO₂ photocatalytic reduction with H₂O on Au/TiO_{2-x}: Combination of plasmonic excitation and oxygen vacancy, *Appl. Catal. B Environ.* 292 (2021), 120147, <https://doi.org/10.1016/j.apcatb.2021.120147>.
- [228] K.K. Ghuman, T.E. Wood, L.B. Hoch, C.A. Mims, G.A. Ozin, C.V. Singh, Illuminating CO₂ reduction on frustrated Lewis pair surfaces: Investigating the role of surface hydroxides and oxygen vacancies on nanocrystalline In₂O_{3-x}(OH)_y, *Phys. Chem. Chem. Phys.* 17 (2015) 14623–14635, <https://doi.org/10.1039/c5cp02613j>.
- [229] K.K. Ghuman, L.B. Hoch, P. Szymanski, J.Y.Y. Loh, N.P. Kherani, M.A. E-Sayed, G. A. Ozin, C.V. Singh, Photoexcited surface frustrated Lewis pairs for heterogeneous photocatalytic CO₂ reduction, *J. Am. Chem. Soc.* 138 (2016) 1206–1214, <https://doi.org/10.1021/jacs.5b10179>.
- [230] L. Wan, Q. Zhou, X. Wang, T.E. Wood, L. Wang, P.N. Duchesne, J. Guo, X. Yan, M. Xia, Y.F. Lie, A.A. Jelle, U. Ulmer, J. Jia, T. Li, W. Sun, G.A. Ozin, Cu₂O nanocubes with mixed oxidation-state facets for (photo)catalytic hydrogenation of carbon dioxide, *Nat. Catal.* 2 (2019) 889–898, <https://doi.org/10.1038/s41929-019-0338-z>.
- [231] T. Yan, N. Li, L. Wang, W. Ran, P.N. Duchesne, L. Wan, N.T. Nguyen, L. Wang, M. Xia, G.A. Ozin, Bismuth atom tailoring of indium oxide surface frustrated Lewis pairs boosts heterogeneous CO₂ photocatalytic hydrogenation, *Nat. Commun.* 11 (2020) 6095, <https://doi.org/10.1038/s41467-020-19997-y>.
- [232] Y. Liu, C. Miao, P. Yang, Y. He, J. Feng, D. Li, Synergetic promotional effect of oxygen vacancy-rich ultrathin TiO₂ and photochemical induced highly dispersed Pt for photoreduction of CO₂ with H₂O, *Appl. Catal. B Environ.* 244 (2019) 919–930, <https://doi.org/10.1016/j.apcatb.2018.12.028>.
- [233] J. Fan, L. Cheng, Y. Liu, Y. He, Y. Wang, D. Li, J. Feng, Insight into synergetic mechanism of Au@Pd and oxygen vacancy sites for coupling light-driven H₂O oxidation and CO₂ reduction, *J. Catal.* 378 (2019) 164–175, <https://doi.org/10.1016/j.jcat.2019.08.031>.
- [234] L.-Y. Lin, S. Kavadiya, X. He, W.-N. Wang, B.B. Karakocak, Y.-C. Lin, M.Y. Berezin, P. Biswas, Engineering stable Pt nanoparticles and oxygen vacancies on defective TiO₂ via introducing strong electronic metal-support interaction for efficient CO₂ photoreduction, *Chem. Eng. J.* 389 (2020), 123450, <https://doi.org/10.1016/j.cej.2019.123450>.
- [235] Y.-X. Pan, Z.-Q. Sun, H.-P. Cong, Y.-L. Men, S. Xin, J. Song, S.-H. Yu, Photocatalytic CO₂ reduction highly enhanced by oxygen vacancies on Pt-nanoparticle-dispersed gallium oxide, *Nano Res* 9 (2016) 1689–1700, <https://doi.org/10.1007/s12274-016-1063-4>.
- [236] F. Yu, C. Wang, H. Ma, M. Song, D. Li, Y. Li, S. Li, X. Zhang, Y. Liu, Revisiting Pt/TiO₂ photocatalysts for thermally assisted photocatalytic reduction of CO₂, *Nanoscale* 12 (2020) 7000–7010, <https://doi.org/10.1039/c9nr09743k>.
- [237] S. Cai, J. Chen, Q. Li, H. Jia, Enhanced photocatalytic CO₂ reduction with photothermal effect by cooperative effect of oxygen vacancy and Au cocatalyst, *ACS Appl. Mater. Interfaces* 13 (2021) 14221–14229, <https://doi.org/10.1021/acsaami.0c23036>.
- [238] W. Wei, Z. Wei, R. Li, Z. Li, R. Shi, S. Ouyang, Y. Qi, D.L. Philips, H. Yuan, Subsurface oxygen defects electronically interacting with active sites on In₂O₃ for enhanced photothermocatalytic CO₂ reduction, *Nat. Commun.* 13 (2022) 3199, <https://doi.org/10.1038/s41467-022-30958-5>.
- [239] J. Zhu, W. Shao, X. Li, X. Jiao, J. Zhu, Y. Sun, Y. Xie, Asymmetric triple-atom sites confined in ternary oxide enabling selective CO₂ photothermal reduction to acetate, *J. Am. Chem. Soc.* 143 (2021) 18233–18241, <https://doi.org/10.1021/jacs.1c08033>.
- [240] X. Pan, Y.-J. Xu, Efficient thermal- and photocatalyst of Pd nanoparticles on TiO₂ achieved by an oxygen vacancies promoted synthesis strategy, *ACS Appl. Mater. Interfaces* 6 (2014) 1879–1886, <https://doi.org/10.1021/am404877e>.
- [241] S. Chai, Y. Men, J. Wang, S. Liu, Q. Song, W. An, G. Kolb, Boosting CO₂ methanation activity on Ru/TiO₂ catalysts by exposing {001} facets of anatase TiO₂, *J. CO₂ Util.* 33 (2019) 242–252, <https://doi.org/10.1016/j.jcou.2019.05.031>.
- [242] X. Pan, Y.-J. Xu, Defect-mediated growth of noble-metal (Ag, Pt, and Pd) nanoparticles on TiO₂ with oxygen vacancies for photocatalytic redox reactions under visible light, *J. Phys. Chem. C* 117 (2013) 17996–18005, <https://doi.org/10.1021/jp4064802>.
- [243] X. Ye, C. Yang, X. Pan, J. Ma, Y. Zhang, Y. Ren, X. Liu, L. Li, Y. Huang, Highly selective hydrogenation of CO₂ to ethanol via designed bifunctional Ir₁-In₂O₃ single-atom catalyst, *J. Am. Chem. Soc.* 142 (2020) 19001–19005, <https://doi.org/10.1021/jacs.0c08607>.
- [244] S. Cai, L. Wang, S. Heng, H. Li, Y. Bai, D. Dang, Q. Wang, P. Zhang, C. He, Interaction of single-atom platinum–oxygen vacancy defects for the boosted photosplitting water H₂ evolution and CO₂ photoreduction: Experimental and theoretical study, *J. Phys. Chem. C* 124 (2020) 24566–24579, <https://doi.org/10.1021/acs.jpcc.0c04931>.
- [245] L. Li, C. Guo, J. Ning, Y. Zhong, D. Chen, Y. Hu, Oxygen-vacancy-assisted construction of FeOOH/CdS heterostructure as an efficient bifunctional photocatalyst for CO₂ conversion and water oxidation, *Appl. Catal. B Environ.* 293 (2021), 120203, <https://doi.org/10.1016/j.apcatb.2021.120203>.